



universität
wien

DISSERTATION

Titel der Dissertation

Magnetic properties of Gd^{3+} based systems

angestrebter akademischer Grad

Doktor der Naturwissenschaften (Dr. rer.nat.)

Verfasserin / Verfasser: Anton Devishvili
Matrikel-Nummer: 0506420
Dissertationsgebiet (lt. Studienblatt): 411 Physik
Betreuerin / Betreuer: Univ.-Doz. Dr. Rotter

Wien, am 14. Juni 2010

Abstract

Gd^{3+} based rare earth systems are of particular interest due to their large spin ($S = 7/2$). The 4f shell is half filled, implying spherically symmetric charge density and no orbital moment ($L = 0$). There are no first order crystal field effects present in this type of systems, therefore, no magnetocrystalline anisotropy is expected. The standard model of rare earth magnetism suggests a relatively simple mean field model treatment which predicts only spin-spin interaction magnetism with classical dipolar anisotropy. A magnetic structure study of several Gd compounds is presented in this thesis. The structure investigation has been performed with neutron scattering techniques at the ILL accompanied by bulk measurements and numerical analysis. Magnetic properties of GdCu_6 (orthorhombic with space-group $P n m a$) can be described well within this model. Susceptibility and magnetization indicate antiferromagnetic order below the Néel temperature $T_N = 16$ K. Neutron diffraction suggests the presence of a long period possibly incommensurate structure of (h 0 0) type propagation vector ($0.16 < h < 0.25$). The results of the neutron diffraction are in accordance with the expectations from the mean field model. In contrast to GdCu_6 , the tetragonal antiferromagnet $\text{GdRu}_2\text{Si}_2(I_4/m m m)$ is not well explained within the framework of the standard model of rare earth magnetism. Magnetization and susceptibility measured along the different crystallographic axes show an unusually high anisotropy and some additional unexpected features in the magnetic phase diagram. Neutron and magnetic X-ray measurements indicate an antiferromagnetic order below the Néel temperature $T_N = 47$ K with a propagation vector of (0.22 0 0). Some partial correspondence to experimentally observed behavior has been obtained by introducing isotropic biquadratic and anisotropic bilinear interactions. Various other Gd intermetallic compounds have been investigated in less detail but the presence of a long period possibly incommensurate magnetic structure is a common feature observed within all studied compounds.

Zusammenfassung

Aufgrund ihres großen Spinmoments ($S = 7/2$) sind gadoliniumhaltige Verbindungen von großem wissenschaftlichen Interesse. Die halbgefüllte 4f Schale führt zu einer kugelsymmetrischen Ladungsverteilung ohne Orbitalmoment ($L = 0$) und es ist keine magnetokristalline Anisotropie zu erwarten. In einer einfachen Molekularfeldtheorie ist ausschließlich die Spin-Spin-Wechselwirkung anisotrop. In dieser Arbeit wurde die magnetische Strukturen verschiedener gadoliniumhaltiger Verbindungen mit Neutronen gemessen und modelliert. Suszeptibilitäts- und Magnetisierungsmessungen weisen darauf hin, dass die orthorhombische Verbindung GdCu_6 unterhalb $T_N = 16$ K antiferromagnetisch geordnet ist. Eine inkommensurable magnetische Ordnung konnte in der Tat durch Neutronendiffraktion bestimmt und mittels einer einfachen Molekularfeldtheorie beschrieben werden. Demgegenüber scheitert eine solche Beschreibung im Fall der tetragonalen Verbindung GdRu_2Si_2 . Schon in Suszeptibilitäts- und Magnetisierungsmessungen beobachtet man eine ungewöhnlich hohe Anisotropie und mehrere magnetische Phasen. Die magnetische Struktur konnte mit Neutronen- und magnetische Röntgenstreuung im Detail bestimmt und nur unter Einbeziehung einer isotropen biquadratischen und einer anisotropen bilinearen Wechselwirkung zufriedenstellend modelliert werden. Diesen beiden sowie allen weiteren untersuchten Verbindungen ist eine inkommensurable Struktur mit großer Periodenlänge gemeinsam.

Contents

1	Introduction	6
1.1	Rare Earth Magnetism	6
1.2	Gadolinium magnetism	9
2	Experimental Methods	10
2.1	Magnetic structure investigations	10
2.1.1	Neutron scattering	10
2.1.2	Magnetic X-Ray Scattering	18
2.2	Other Magnetic investigation methods	20
2.2.1	Magnetometry	20
2.2.2	Dilatometry	22
2.2.3	Calorimetry	24
3	Data Analysis and Modeling	25
3.1	Nuclear and magnetic scattering	25
3.2	Mean-Field model	26
4	GdRu₂Si₂	29
4.1	Introduction	29
4.2	Sample preparation	30
4.3	Bulk measurements	30
4.4	Neutron diffraction	33
4.5	Magnetic X-Ray Scattering	34
4.6	Model A: Standard model for Gd Magnetism	38
4.6.1	Hamiltonian	38
4.6.2	Numerical simulation	38
4.6.3	Discussion of Model A	43
4.7	Model B: Biquadratic exchange	44
4.7.1	Hamiltonian	44
4.7.2	Numerical simulations	46
4.7.3	Discussion of Model B	46
4.8	Model C: Combined anisotropic bilinear and biquadratic exchange	47
4.8.1	Hamiltonian	47
4.8.2	Numerical simulations	48
4.8.3	Discussion of Model C	51
4.9	Conclusions	55

5	GdCu₆	58
5.1	Introduction	58
5.2	Sample preparation	58
5.3	Neutron diffraction	59
5.4	Numerical simulation	60
5.5	Discussion	64
5.6	Conclusion	68
6	Other Gd compounds	68
6.1	GdRu ₂ Ge ₂	69
6.2	GdPt ₃ Si	71
6.3	Gd ₂ PdSi ₃	77
6.4	GdCuSn	78
6.5	GdSi	80
6.6	Gd ₅ Ge ₃	83
7	Conclusions	86
8	Acknowledgments	88
8.1	Institutions and Organizations	88
8.2	GdRu ₂ Si ₂	88
8.3	GdCu ₆	89
8.4	GdRu ₂ Ge ₂	89
8.5	GdPt ₃ Si	89
8.6	Gd ₂ PdSi ₃	89
8.7	GdCuSn	90
8.8	GdSi	90
8.9	Gd ₅ Ge ₃	90
8.10	General contributions	90
9	Appendixes	91
A	Different Hamiltonian notations.	91
B	Stevens Operators	93

1 Introduction

1.1 Rare Earth Magnetism

The "Rare Earth" elements (also known as lanthanoids) comprise from fifteen elements of the periodic system of elements with the numbers from 57 to 71 (see Table 1).

The term "Rare Earth" originates from the mineral from which they were isolated. These were uncommon oxide-type minerals (earths), initially found in Gadolinite from a mine in the village of Ytterby, Sweden. However, with the exception of the highly-unstable promethium, the rare earth elements are found in relatively high concentrations in the earth's crust. For example cerium is the 25th most abundant element in the earth's crust at 68 parts per million.

The lanthanoids are the f-block elements. They represent the elements with different amount of $4f$ electrons. Lanthanum for example has no $4f$ electrons therefore presenting the non filled $4f$ shell while lutetium has a full $4f$ electron shell (see Table 1 for more details).

In order to understand the magnetism of the rare earths the description of the electronic states, particularly of the $4f$ electrons, in the atoms is crucial. The generalized Hamiltonian for the electrons bound to atomic nuclei is described with the following formula:

$$\mathcal{H} = \mathcal{H}_{kin} + \mathcal{H}_{col}^{ext} + \mathcal{H}_{col}^{int} \quad (1)$$

Here \mathcal{H}_{kin} represents the kinetic energy of an electron, \mathcal{H}_{col}^{ext} is the nuclear Coulomb potential or simply $-Ze^2/r_i$. The difficulties in solving this problem reside in the second term \mathcal{H}_{col}^{int} , the Coulomb interaction between the electrons. In order to solve this equation for the $4f$ electron case the Coulomb interaction is substituted by a self-consistent field (see [1]). The system is considered as a set of non-interacting electrons with density $n(\mathbf{r})$ of the real system, satisfying the single-particle Schrödinger equation:

$$\left(-\frac{\hbar^2}{2m} \nabla^2 + v_{\text{eff}}(\mathbf{r}) \right) \psi_i(\mathbf{r}) = \mathcal{E}_i \psi_i(\mathbf{r}) \quad (2)$$

where the effective potential v_{eff} in the local approximation is described by

$$v_{\text{eff}}(\mathbf{r}) = \int \frac{e^2 n(\mathbf{r}')}{|\mathbf{r} - \mathbf{r}'|} d\mathbf{r}' + v_{\text{ext}}(\mathbf{r}) + v_{\text{xc}}[n(\mathbf{r})] \quad (3)$$

where v_{xc} is the local approximation to the exchange-correlation contribution to the chemical potential of the electron gas, and $n(\mathbf{r})$ is the electron density.

In order to determine the atomic structure, the Schrödinger equation (2) must be solved by the Hartree self-consistent procedure, in which, the potential (3) generates wavefunctions through a process of iteration. Since this potential is spherically symmetric in atoms, the single-particle wavefunctions may be written as the product of a radial function, a spherical harmonic and a spin function.

$$\psi_{nlm_l m_s} = R_{nl}(r)Y_{lm_l}(\hat{\mathbf{r}})\chi_{m_s} \quad (4)$$

where $\hat{\mathbf{r}}$ is a unit vector in the direction of \mathbf{r} , the spin quantum number m_s can take the values $\pm\frac{1}{2}$. The radial component satisfies the equation

$$-\frac{\hbar^2}{2m} \frac{d^2[rR_{nl}(r)]}{dr^2} + \left(v_{\text{eff}}(r) + \frac{l(l+1)\hbar^2}{2mr^2} - \mathcal{E} \right) [rR_{nl}(r)] = 0 \quad (5)$$

Some radial wavefunctions for rare earth atoms are shown in Fig. 1. The $4f$ electrons are well embedded within the atom, and shielded from the surroundings by the $5s$ and $5p$ states. The $5d$ and $6s$ electrons form the conduction bands in metals.

Table 1: Properties of the tripositive rare earth ions. L is the total spin quantum number, S is the total orbital quantum number, J is the total angular momentum quantum number, g is the Landé factor and $(g-1)^2 J(J+1)$ is the De Gennes factor. Values are taken from [1]

$4f^n$	Ion^{+++}	L	S	J	g	$(g-1)^2 J(J+1)$
0	La	0	0	0	—	—
1	Ce	3	$\frac{1}{2}$	$\frac{5}{2}$	$\frac{6}{7}$	0.18
2	Pr	5	1	4	$\frac{4}{3}$	0.80
3	Nd	6	$\frac{3}{2}$	$\frac{9}{2}$	$\frac{8}{11}$	1.84
4	Pm	6	2	4	$\frac{3}{5}$	3.20
5	Sm	5	$\frac{5}{2}$	$\frac{5}{2}$	$\frac{3}{7}$	4.46
6	Eu	3	3	0	—	—
7	Gd	0	$\frac{7}{2}$	$\frac{7}{2}$	2	15.75
8	Tb	3	3	6	$\frac{3}{5}$	10.50
9	Dy	5	$\frac{5}{2}$	$\frac{15}{2}$	$\frac{4}{3}$	7.08
10	Ho	6	2	8	$\frac{3}{5}$	4.50
11	Er	6	$\frac{3}{2}$	$\frac{15}{2}$	$\frac{4}{3}$	2.55
12	Tm	5	1	6	$\frac{5}{7}$	1.17
13	Yb	3	$\frac{1}{2}$	$\frac{7}{2}$	$\frac{6}{7}$	0.32
14	Lu	0	0	0	—	—

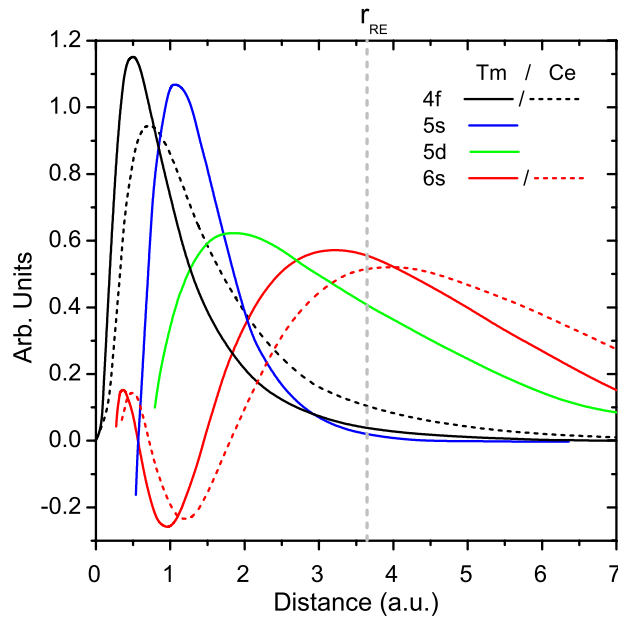


Figure 1: The radial components of atomic wavefunctions for Ce and Tm. The Tm wavefunctions are contracted, relative to those of Ce, due to the incomplete shielding of the greater nuclear charge. The $4f$ shell is localized well within the average rare earth atomic radii r_{RE} . The data was taken from [1].

When a large number of rare earth atoms are assembled to form a solid, the $4f$ electrons generally remain localized, so that their magnetic properties closely resemble those in the free atoms. This is one of the fundamental reasons of particular importance of these systems. The localization of the spin renders many complex magnetic phenomena unnecessary while analyzing the magnetic properties. Most of rare earth systems can be successfully treated within the mean field model.

1.2 Gadolinium magnetism

One of the rare earth elements is of particular interest. Gd^{3+} has the largest spin available in the periodic table ($S = 7/2$) and no orbital moment ($L = 0$) (see Table 1). The fact that there is no orbital moment in Gd^{3+} makes the Gd compounds unique and extremely important for the study of atomic magnetism¹.

According to the Hund's rules the ground state for Gd^{3+} ion is ${}^8S_{7/2}$. Therefore in what follows only the perturbation approach to the ground state multiplet will be considered.

The simplified magnetic only Hamiltonian for a classical Rare Earth system consists of three fundamental contributions: the Zeeman term, Heisenberg exchange and single ion anisotropy (e.g. crystal field effect)

$$\mathcal{H} = \mathcal{H}_{exch} + \mathcal{H}_{cf} + \mathcal{H}_{zeeman} \quad (6)$$

The last term here is the Zeeman splitting which is attributed to the magnetic moment interacting with the external magnetic field. Till late sixties most of the magnetic phenomena were mainly classified by studying the magnetization under applied magnetic field.

The second term \mathcal{H}_{cf} in the Hamiltonian (6) is the Crystal-Field effect. Having an electrostatic origin, this effect is responsible for the splitting of the $4f$ electron ground state due to non homogeneous charge distribution in the crystal matrix. Since the charge distribution is symmetry dependent it is believed to be responsible for magnetic anisotropy and magnetostriction effect in Rare-Earth systems. This well established theory has been practically verified in many rare earth systems [2, 3, 4, 5]. However in the case of Gd^{3+} there is no single ion anisotropy (no crystal field effect). The second term in the Hamiltonian (6) becomes zero. This gives the opportunity to study other (smaller) sources of magnetic anisotropy [6, 7, 8, 9] arising from the first term.

¹ Eu^{2+} is also exhibiting the same properties. However, it was decided to focus this research on Gd compounds since Eu^{2+} sample preparation is in many cases complicated due to the chemical reactivity of Eu and it's affinity to oxygen. Valence instabilities are also common in Eu based compounds.

The first term \mathcal{H}_{exch} in (6) represents the classical spin - spin exchange interaction. This term dictates the Gd^{3+} magnetism since it is the only magnetic interaction believed to be present in Gd systems. \mathcal{H}_{exch} is mostly attributed to the RKKY interaction that exists in the systems with electron conduction band. The complexity of this term will be discussed in detail in this thesis. The evidence of large anisotropy and second order magnetic interactions will be illustrated for several Gd based antiferromagnets. The importance of the classical dipolar interaction [8] will also be mentioned for these systems.

In order to study the spin-spin exchange the research has been narrowed down to metallic Gd - based antiferromagnets. The large spin of Gd^{3+} provides a significant magnetic signal, therefore sophisticated high resolution methods are not necessary for bulk investigations. The rather complicated magnetic interactions in comparison to simple ferromagnets as well as feature rich magnetic phase diagrams are the main reasons for choosing antiferromagnets for this study². As the result of the magnetic interaction the Gd compounds order in various magnetic structures and the key element of this research is the investigation of magnetic structures. The magnetic properties of some Gadolinium antiferromagnets are widely studied mainly due to a presence of significant magnetostriction, magnetocaloric and magnetoresistance effects. However only a limited knowledge of magnetic structure is available at the moment. The results of the research on the magnetic structure of most Gd intermetallic antiferromagnets are presented in Table 2. The compounds reviewed in this thesis are marked in bold³.

2 Experimental Methods

Experiments presented here aim to investigate the magnetic structures of the Gd^{3+} intermetallic compounds. The collected experimental data will be analyzed theoretically by different methods. More details on the experimental methods will be given in the following sections.

2.1 Magnetic structure investigations

2.1.1 Neutron scattering

The neutron is a subatomic particle with no net electric charge and a mass slightly larger than the one of a proton. The nuclei of most atoms consists of protons and

²The more detailed explanation of the advantage of antiferromagnets in studies of spin-spin exchange will be discussed in the following chapters.

³The data in the table was assembled mostly according to the available published results. Only minor private communication results are included from other research groups. Therefore the table might not represent all available knowledge on this subject.

Table 2: Magnetic structures of some Gd compounds. The second column describes the experimental method (n - neutron diffraction, x - magnetic X-ray scattering, m- Moessbauer spectroscopy, μ SR- muon spin relaxation). In the third column the ordering temperatures are given. The fourth and fifth columns contain the propagation vector, and the experimentally derived moment direction at low temperature (moment direction coordinates $[m_x m_y m_z]$ refer to Euclidean coordinate system with $x||a$, $y||b$ and $z||c$). The compound studied within this thesis work are marked in bold.

Compound	Method	Ordering Temperature (K)	Propagation Vector τ	Experimental Moment Direction
cubic				
GdAg (<i>bcc</i>)	n [10]	134	(1/2 1/2 0)	[001]
GdCu (<i>bcc</i>)	n [11]	150	(1/2 1/2 0)	[001]
GdX <i>fcc</i>				
X=S,P,Se	n [12, 13]	50,28,60	(3/2 3/2 3/2)	\perp [111]
X=As,Sb,Bi	n [12, 13]	15.2,32,19	(3/2 3/2 3/2)	\perp [111]
GdCu ₂ In	n [8]	10	(1/3 1 0)	\perp [001]
GdPd ₂ In		10 [14]		
GdIn ₃	x [15]	43 [16]	(1/2 1/2 0)	???
Gd ₂ Ti ₂ O ₇	n [17]	1	(1/2 1/2 1/2)	???
GdB ₆	x [18]	16	(1/4 1/4 1/2)	???
Gd ₂ Sn ₂ O ₇	n [19]	1	(0 0 0)	???
GdCu ₄ In	n[20]	7	(0 1/2 1)	[010]
hexagonal				
Gd ₂ CuGe ₃		12 [21]		
GdGa ₂	m [22]	23.7	(0.39 0.39 0)	
GdCu ₅	m [22]	26	(1/3 1/3 0.22)	
Gd ₅ Ge ₃	n	79 [23]	(0 0 0.34)	\perp [001]
Gd ₇ Rh ₃		140 [24, 25]		
Gd₂PdSi₃	m,n	21 [26]	(0.137 $\overline{0.137}$ 0)	
GdAuSn	m [27]	35 [28]	(0 1/2 0)	
GdAuGe		16.9 [29]		
GdAgGe		14.8 [30]		
GdAuIn		12.2 [30]		
GdAuMg		81 [31]		
GdAuCd	m [32]	66.5 [32]	(1/2 0 1/2)	
Gd ₂ In	n [33] μ SR[34]	100	(0 0 1/6)	
GdNi ₅		32	(0 0 0)	[001]
GdCuSn	m[28],n	24	(0 1/2 0)	[001]

Table 3: Magnetic structures of some Gd compounds. Continuation of table 2. The compound studied within this thesis work are marked in bold.

Compound	Method	Ordering Temperature (K)	Propagation Vector τ	Experimental Moment Direction
tetragonal				
GdAg ₂	n [35]	22.7	(1/4 2/3 0)	[1 1 0]
GdAu ₂	n	50	(5/6 1/2 1/2)	\perp [0 1 1]
GdAu ₂ Si ₂	n [8]	12	(1/2 0 1/2)	[0 1 0]
GdCu ₂ Si ₂	n [36]	12.5	(1/2 0 1/2)	[0 1 0]
GdNi ₂ Si ₂	n [36]	14.5	(0.207 0 0.903)	[0 1 0]
GdNi ₂ B ₂ C	n,x [37]	20	(0.55 0 0)	[0 1 0]
Gd ₂ Ni _{2-x} In		20 [38]		
Gd ₂ Ni ₂ Cd		65 [39]		
Gd ₂ Ni ₂ Mg		49 [40]		
Gd ₂ Pd ₂ In		21 [41]		
GdB ₄		42	(1 0 0) [42]	
GdRu₂Si₂	n,x	47 [43]	(0.22 0 0)	\perp [1 0 0]
GdRu₂Ge₂	n	33 [43]	(2/5 5/6 1/2)	[2/5 5/6 0]
GdNi ₂ Sn ₂		7 [44]		
GdPt ₂ Ge ₂		7 [44]		
GdCo ₂ Si ₂		45 [44]		
GdPd ₂ Ge ₂		18 [44]		
GdPd ₂ Si ₂		16.5 [45]		
GdIr ₂ Si ₂		82.4 [45]		
GdPt ₂ Si ₂	n [35]	9.3 [45]	(1/3 1/3 1/2)	
GdOs ₂ Si ₂		28.5 [45]		
GdAg ₂ Si ₂		10 [44]		
GdFe ₂ Ge ₂		9.3 [46, 47]		
GdCu ₂ Ge ₂		15 [46]		
GdRh ₂ Ge ₂		95.4 [46]		
GdRh ₂ Si ₂		106 [45]		
GdPt₃Si	n	7.5 [48]		
GdNi ₂ Ge ₂		27	(0 0 0.79) [49]	
GdCo ₂ Ge ₂	x [50]	37.5 [46]	(0 0 0.93)	
Gd ₂ CuO ₄	[51]	6.4	(0 0 0)	

Table 4: Magnetic structures of some Gd compounds. Continuation of table 3. The compound studied within this thesis work are marked in bold.

Compound	Method	Ordering Temperature (K)	Propagation Vector τ	Experimental Moment Direction
orthorhombic				
GdCu(FeB)	n [11]	45	(0 1/4 1/4)	\perp [0 1/4 1/4]
Gd ₃ Rh		112 [52]		
Gd ₃ Ni		100 [53]		
Gd ₃ Co		130 [54, 55]		
GdSi	n	55 [56]	(0 0.5 0.093)	
GdCu₆	n	16 [57]	(0.167 0 0)	\perp [1 0 0]
GdAlO ₃		3.9 [58]		
GdBa ₂ Cu ₃ O ₇	n [59]	2.2	(1/2 1/2 1/2)	[60]
GdPd ₂ Si		13 [61]		
GdCu ₂	n,x [62]	42	(1/3 0 0)	[1 0 1]
Gd ₅ Ge ₄	130 [63]	(0 0 0) [64]	[65]	
GdNi _{0.4} Cu _{0.6}	n [66]	63	(0 0 1/4)	
Gd ₂ S ₃		10 [67]	(0 0 0) [68]	
GdNiSn	m [69]	11 [70]	(0 0 0)	
GdBa ₂ Cu ₃ O ₇	n [59]	2.2	(1/2 1/2 1/2)	[001]

neutrons, which are therefore collectively referred to as nucleons. The number of protons in a nucleus is the atomic number and defines the type of element the atom forms. The number of neutrons determines the isotope of an element.

Outside the nucleus, free neutrons are unstable and have a mean lifetime of 885.7 ± 0.8 s (about 15 minutes), decaying by emission of a negative electron and antineutrino to become a proton:



This decay mode, known as beta decay, can also transform the character of neutrons within unstable nuclei.

When bound inside of a nucleus, the instability of a single neutron to beta decay is balanced against the instability that would be acquired by the nucleus as a whole if an additional proton were to participate in repulsive interactions with the other protons that are already present in the nucleus. As such, although free neutrons are unstable, bound neutrons are not necessarily so. The same reasoning explains why protons, which are stable in empty space, may be unstable when bound inside of a nucleus.

Even though the lifetime of a free neutron is small, neutron spectroscopy is a well established technique for probing bulk matter.

The energy E of a neutron can be related to its wave vector \mathbf{k} , the speed of a neutron v , its wavelength λ or temperature T via the relation:

$$E = \frac{\hbar^2 k^2}{2m} = \frac{1}{2}mv^2 = \frac{h^2}{2m\lambda^2} = k_B T \quad (8)$$

The value $v = 2.2$ km/s is conventionally taken as a standard velocity for thermal neutrons. It is clear that the decay processes have to be neglected within the distances provided by conventional neutron scattering setups. More information on correspondence of velocities wavelengths and energies of free neutrons can be observed in Table 5

Table 5: Approximate values for range of energy, temperature and wavelengths for three types of neutron moderators.

Source	Energy (meV)	Temperature (K)	Wavelength (Å)
cold	0.1-10	1-120	30-3
thermal	5-100	60 - 1000	4-1
hot	100-500	1000-6000	1-0.4

The penetration depth of neutrons in matter is extremely long, mainly because they have no charge. Neutron scattering is therefore well suited to the study of

bulk properties. As one can see from the Table 5 the temperature of sub-thermal neutrons for example is that of liquid helium while the wavelength is comparable to the atom distances in solids, giving a relatively high resolution while studying the lattice excitations.

In order to present the mathematical apparatus of the scattering theory it is important to define the scattering length and cross section. In the case of a simple scattering event on a fixed atom (the reference frame) the wavefunction of an incoming particle will be

$$\psi_{inc} = e^{i\mathbf{k}z} \quad (9)$$

The neutron with wavevector \mathbf{k} is parallel to the z axis, since the scattering process in such configuration will be spherically symmetric along z [71]. The wavefunction of the scattered neutrons at the point r would then be written in the form

$$\psi_{sc} = -\frac{b}{r}e^{i\mathbf{k}r} \quad (10)$$

The quantity b in equation (10) is known as the scattering length. The minus sign in the equation (10) is arbitrary and corresponds to a positive value of b for a repulsive potential. Using (9-10) we can thus define the differential scattering cross-section $\frac{d\sigma}{d\Omega}$ for an elastic scattering event (velocity of neutron $v_{inc} = v_{sc}$ on a fixed nucleus)

$$\frac{d\sigma}{d\Omega} = b^2 \quad (11)$$

The $\frac{d\sigma}{d\Omega}$ is called a differential scattering cross section, the physical meaning of this quantity is the number of neutrons scattered per incoming neutron flux into solid angle Ω . The total scattering cross section in that case would simply be

$$\sigma_{tot} = \int_{all \ dir.} \left(\frac{d\sigma}{d\Omega} \right) d\Omega = 4\pi b^2 \quad (12)$$

The scattering length of most elements remains independent of neutron energy just as expressed in equation (10). However, in some cases the scattering length depends on the energy of the neutron. The scattering on the nuclei with energy (original nucleus plus the neutron) close to the excited state is associated with the existence of a non zero imaginary part of b which describes a large absorption of neutrons. The ^{157}Gd is one example of such a nuclei. In case of multiple scattering events on a natural substance consisting of several isotopes the cross section is becoming dependent on the isotope abundance distribution. Instead of preparing the isotopically pure substances for the neutron scattering experiments much simpler mathematical solution is proposed by separating the scattering cross

section contributions from the average scattering length \bar{b} as coherent scattering cross section and incoherent representing the scattering on the standard deviation from average \bar{b} [71].

$$\sigma_{coh} = 4\pi(\bar{b})^2 \quad \text{and} \quad \sigma_{incoh} = 4\pi(\overline{b^2} - (\bar{b})^2) \quad (13)$$

Some values of coherent and incoherent cross sections of natural Gd are shown in Table 6.

Table 6: Thermal neutron scattering lengths and cross sections of Gadolinium. Data taken from [72]

Isotope	Natural abundance (%)	coherent σ_{coh} (barn)	incoherent σ_{incoh} (barn)	total σ_{tot} (barn)	absorption σ_{abs} ⁴ (barn)
Gd		29.3	151.(2.)	180.(2.)	49700.(125.)
¹⁵² Gd	0.2	13.(8.)	0	13.(8.)	735.(20.)
¹⁵⁴ Gd	2.1	13.(8.)	0	13.(8.)	85.(12.)
¹⁵⁵ Gd	14.8	40.8	25.(6.)	66.(6.)	61100.(400.)
¹⁵⁶ Gd	20.6	5	0	5	1.5(1.2)
¹⁵⁷ Gd	15.7	650.(4.)	394.(7.)	1044.(8.)	259000.(700.)
¹⁵⁸ Gd	24.8	10.(5.)	0	10.(5.)	2.2
¹⁶⁰ Gd	21.8	10.52	0	10.52	0.77

The real values that are measured within the neutron scattering experiment are however slightly more complicated than the cross sections of an isolated nucleus.

It is assumed that neutrons interact with matter by means of the Fermi pseudo-potential:

$$V(\mathbf{r}) = \frac{2\pi\hbar^2}{m}b\delta(\mathbf{r} - \mathbf{R}) \quad (14)$$

where m is the neutron mass and b is a scattering length in a sense of an impenetrable sphere of radius b around position \mathbf{R} .⁵ Using this potential the partial differential coherent cross section can be written as [71]

⁴Since absorption is wavelength dependent the values are given for thermal neutrons with speed of $v = 2.2$ km/s.

⁵The Fermi pseudo-potential as given by equation (14) is a formal way of defining a potential which in the Born approximation produces the correct(isotropic) scattering picture. It is not the true potential.

$$\left(\frac{d\sigma}{d\Omega}\right)_{coh.el.}^{nuc} = b^2 \left| \sum_l e^{i\mathbf{Q}\cdot\mathbf{R}_l} \right|^2 \quad (15)$$

where $\mathbf{Q} = \mathbf{k}_{inc} - \mathbf{k}_{sc}$ is the scattering vector, l is the number of nucleus with position \mathbf{R}_l . For a large enough crystal with positions R_l forming a primitive lattice we can show that

$$\left| \sum_l e^{i\mathbf{Q}\cdot\mathbf{R}_l} \right|^2 = N \frac{(2\pi)^3}{\mathcal{V}_0} \sum_{\mathbf{G}} \delta(\mathbf{Q} - \mathbf{G}) \quad (16)$$

where \mathcal{V}_0 is the unit cell volume containing N identical atoms and \mathbf{G} is a reciprocal lattice vector introduced in a way that

$$e^{i\mathbf{G}\cdot\mathbf{R}_l} = 1 \quad \text{for all } l \quad (17)$$

The more generalized form of partial differential cross section for a crystal with more sophisticated symmetry and composition contains the nuclear unit cell structure factor defined as

$$F_N(\mathbf{Q}) = \sum_d e^{i\mathbf{Q}\cdot\mathbf{R}_d} \bar{b}_d \quad (18)$$

where \mathbf{d} denotes each of the atoms in the primitive unit cell so that the partial differential cross section for an elastic scattering event can be written as

$$\left(\frac{d\sigma}{d\Omega}\right)_{coh.el.}^{nuc} = \frac{(2\pi)^3}{\mathcal{V}_0} \sum_{\mathbf{G}} \delta(\mathbf{Q} - \mathbf{G}) |F_N(\mathbf{Q})|^2 \quad (19)$$

From the equation (19) it is clear that the scattering occurs only if $\mathbf{Q} = \mathbf{G}$. This condition is the same as the Bragg's law, which can be expressed (geometrically, using a cosines theorem) in a more familiar way

$$n\lambda = 2d \sin(\theta) \quad (20)$$

where d is the spacing of the scattering planes and n is the order of the diffraction maxima and θ is the scattering angle.

All of the studied compounds are exhibiting antiferromagnetism. Since magnetic structure has a certain periodicity it can be Fourier expanded

$$\mathbf{m}_{ld} = \mathbf{m}_d^\tau e^{i\tau\mathbf{R}_l} \quad (21)$$

here m_{ld} is the moment at the position d of the cell l and τ denotes the propagation vector (or vectors in some cases).

Due to the fact that the neutron has magnetic moment it can probe magnetic structures by interacting with their spins. In the simplest case this interaction is assumed to be dipole only and the partial differential cross section for an elastic magnetic scattering event can be written as

$$\left(\frac{d\sigma}{d\Omega}\right)_{coh.el.}^{mag} = (\gamma r_0)^2 N_m \frac{(2\pi)^3}{V_{0m}} \sum_{\mathbf{G}} \sum_{\mathbf{Q}} |F_{M\perp}(\mathbf{Q})|^2 \delta(\mathbf{Q} - \mathbf{G} \pm n\tau) \quad (22)$$

where $\gamma = 1.913$ is a constant representing the proportionality between neutron dipole magnetic moment and nuclear magneton, $r_0 = 2.818 \cdot 10^{-15}$ m is the classical radius of the electron and the magnetic structure factor is expressed as

$$F_M(\mathbf{Q}) = \sum_d f_d(\mathbf{Q}) m_{ld} e^{i\mathbf{Q}\mathbf{R}_d} \quad (23)$$

here $f_d(\mathbf{Q})$ is the magnetic form factor of an atom d at the position \mathbf{R}_d . Please note that $F_{M\perp} = F_M - \hat{\mathbf{Q}}(F_M \cdot \hat{\mathbf{Q}})$ is used in (22) and $\hat{\mathbf{Q}} = \mathbf{Q}/|\mathbf{Q}|$ is the unit vector. Because of the term $F_{M\perp}$ the magnetic scattering amplitude is highly anisotropic. This anisotropy depends on the respective orientations of the magnetic moment \mathbf{m} and the scattering vector \mathbf{Q} . Therefore the neutron scattering experiments give a direct method for obtaining the Fourier components of the magnetic structure \mathbf{m}_d^r described in (21) [73].

As one can see from the last term of (22) the magnetic scattering also satisfies the Bragg law. Moreover in the antiferromagnetic case the scattering on the magnetic reflections is actually different from the nuclear one and represent satellites of nuclear reflections along the magnetic propagation vector τ . The magnetic form factor (23) is falling rapidly with increasing \mathbf{Q} therefore within the resolution of a typical neutron experiment only the first order satellites are observed. However from (18) and (23) one can notice that when knowing the form factor f_d the estimation of the magnetic moment is possible by comparing the nuclear to the magnetic intensities.⁶

2.1.2 Magnetic X-Ray Scattering

As seen in the previous chapter a big disadvantage of neutron scattering on Gd^{3+} is the resonance processes in ^{157}Gd which lead to a large absorption cross section. However in case of x-rays the other type of resonance processes actually gives a possibility for a much higher resolution scattering on magnetic structures. Since

⁶As will be mentioned later this is a one of the main advantages of neutrons over other magnetic structure investigation methods.

the high energy photons are interacting mainly with the electron charge clouds they have very low penetration depth⁷

The general elastic x-ray scattering cross section is similar to the one of a neutron (15)

$$\left(\frac{d\sigma}{d\Omega}\right)_{coh.el.} = r_0^2 \left| \sum_l e^{i\mathbf{Q}\cdot R_l} f_l(k_{inc}, k_{sc}, \hbar\omega) \right|^2 \quad (24)$$

where f_l represents the scattering amplitude from an l 'th atom and $r_0 = 2.8 \cdot 10^{-15}$ m is the classical electron radius. f_l is commonly known as the scattering factor and consists of several fundamental contributions.

$$f_l(k_{inc}, k_{sc}, \hbar\omega) = f_l^{charge}(\mathbf{Q}) + f_l^{nonres}(\mathbf{Q}, k_{inc}, k_{sc}) + f_l^{res}(k_{inc}, k_{sc}, \hbar\omega) \quad (25)$$

here f_l^{charge} is the Thomson scattering on the charge density of electrons (similar to the nuclear structure factor for neutron scattering), f_l^{nonres} is the non-resonant magnetic scattering amplitude and the f_l^{res} is the resonant magnetic x-ray scattering. The analytical formulation for f_l^{nonres} and f_l^{charge} can be found in [74, 75]. An estimate of the ratio between charge (e.g. nuclear) and non resonant magnetic scattering contribution can be expressed as

$$\left| \frac{f_l^{nonres}}{f_l^{charge}} \right|^2 \sim \left(\frac{\hbar\omega}{mc^2} \right)^2 \left(\frac{F_m}{F_c} \right)^2 | \langle S \rangle | \left(\frac{N_m}{N} \right)^2 \quad (26)$$

where F_m and F_c are the magnetic and charge form factors, $\langle S \rangle$ is the spin of one electron and N_m/N is the ratio of the number of magnetic to total electrons. For typical electron energies of 5 – 10 keV this quantity rarely exceeds 10^{-6} making the nonresonant magnetic x-ray scattering experiment of no preference. The resonant magnetic scattering is a very common tool in magnetic structure determination of Gd compounds (L_{III} resonance) since it gives a considerable scattering intensity and does not suffer from the absorption problem common to neutron experiments.

The partial differential cross section of resonant scattering of linearly polarized ($\sigma \rightarrow \pi$) radiation on the magnetic structure with propagation vector τ can be written in a form

$$\left(\frac{d\sigma}{d\Omega}\right)_{coh.el.}^{res.mag.} = \frac{1}{4} \cos^2\theta |F^{(1)}| \delta(\mathbf{Q} - \mathbf{G} \pm \tau) \quad (27)$$

⁷Absorption limits the 'effective' volume in x-ray scattering in general and especially for resonant x-ray scattering. Nevertheless - contrary to neutron scattering - the brilliance of current x-ray sources make investigations on such a small volume possible.

here $F^{(n)}$ are the resonant matrix elements which are determined by the atomic properties of the resonant scatterer [76]. The resonant matrix elements do not depend on the charge form factor therefore no proper estimation of magnetic moment is possible.

2.2 Other Magnetic investigation methods

The magnetic structure investigations with scattering techniques are the major part of this thesis. Neutron scattering experiments have been performed for every compound studied in this thesis whereas only few magnetic x-ray scattering experiments have been carried out. Due to the rather poor resolution of neutron experiments and the limited amount of single crystals for high resolution experiments other techniques are necessary in order to make a definitive statement on the discovered magnetic structures. Other bulk measurement techniques applied to the same substances are used as a reference to the result of the scattering experiment. In many cases the data has been obtained by other groups and therefore only brief explanations of the bulk experimental techniques used are presented here.

2.2.1 Magnetometry

The magnetization as a quantity of magnetic moment per unit volume is related to an external applied field \mathbf{H} in the following way:

$$\mathbf{M} = \frac{1}{V} \sum_i \mathbf{m}_i \quad (28)$$

where the sum over the atomic moment \mathbf{m}_i is performed over the total volume V . The magnetization changes while external magnetic field is applied which can be quantitatively described by the magnetic susceptibility χ_m :

$$\chi_m = \frac{\partial \mathbf{M}}{\partial \mathbf{H}} \quad (29)$$

The principle aim of magnetometry is to measure those quantities under various conditions (either intrinsic or induced by an applied field). This can be achieved in a number of ways using various magnetic phenomena. The various types of magnetometer fall within two categories: the magnetometers measuring the force acting on a sample in an inhomogeneous magnetic field (magnetic balance or magnetic pendulum) or the ones measuring the magnetic field produced by a sample (Vibrating Sample Magnetometers, Superconducting Quantum Interference Devices)[77].

The magnetometers measuring the force acting on a sample are infrequently used these days due to poor resolution and lack of precise control of the sam-

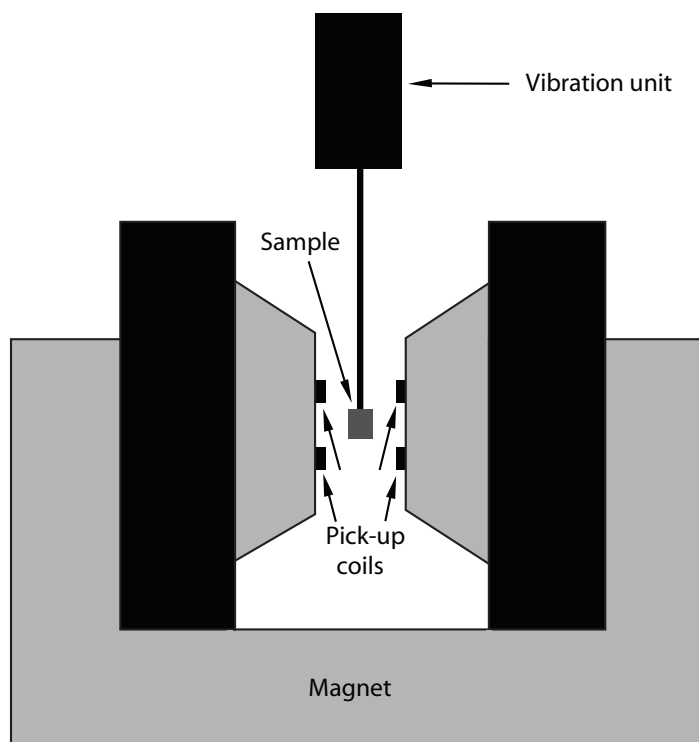


Figure 2: The principal schematic of a vibrating sample magnetometer. The vibration/rotation of the sample depends on the pick up coil position and usually is occurring along the sample holder stick.

ple environment. Superconducting Quantum Interference Device also known as SQUID is one of the most sensitive forms of magnetometry. It uses a combination of superconducting materials and Josephson junctions to measure magnetic fields with resolutions up to $\approx 10^{-14}$ kG [78]. It is designed to be the most precise method for measuring magnetization and it is not used within this thesis due to lack of demand for such a high resolution. Since all the systems investigated are Gd^{3+} antiferromagnets with a considerable magnetic moment and low Néel temperature the magnetization measurements can be performed with a standard Vibrating Sample Magnetometer (VSM) insert in a superconducting cryomagnet.

If the sample vibrates with sinusoidal motion between the poles of an electromagnet, a sinusoidal electrical signal can be induced in suitably placed pick-up coils. The signal has the same frequency of vibration and its amplitude will be proportional to the magnetic moment induced on a sample and its relative position with respect to the pick-up coils system. The schematic representation of a standard VSM setup is shown in Fig. 2.

In this thesis both types of magnetization measurements are in use. The field

dependence of magnetization is measured along different directions of sample orientation. This quantity provides an estimate of the total magnetic moment when the antiferromagnetic order is totally suppressed by an applied field leading to a ferromagnetic structure. Some information about phase transitions and their order can also be obtained. The other widely used quantity is temperature dependence of magnetic susceptibility. It is measured as the temperature dependence of the magnetization of the sample under a small (usually 0.1 – 0.3 T) applied magnetic field. This quantity is crucial for identification of magnetic order and temperature related phase transitions.

2.2.2 Dilatometry

If a magnetic field is applied to a magnetic material the shape of the material changes. This effect is known as magnetostriction and is used in technical applications such as generators of ultrasonic waves or high precision positioning devices [79].

The temperature and magnetic field dependence of the lattice variation of the system is a very important property. Table 7 illustrates different measurement methods, their respective sensitivity as well as the temperature and field ranges.

Table 7: Different methods commonly used to measure thermal expansion and magnetostriction [80].

Method	Sensitivity (dl/l)	External Parameters
Neutron diffraction	10^{-4}	0.01-600 K, 0-15 T
EXAFS at ESRF	10^{-4}	300 K, 0-2 T
X-ray diffraction	10^{-5}	1.5-2000 K, 0-7 T
Strain gauges	10^{-7}	1.5-700 K, 0-30 T
Interferometry	10^{-8}	4-2000 K, 0 T
Capacitive dilatometers	10^{-9}	0.01-1000 K, 0-40 T

The relative lattice thermal variation (dL/L) in the temperature range of 100K is about 10^{-3} , therefore a thermal expansion can be often measured with low resolution methods like x-ray diffraction. However magnetostriction is an effect of considerably lower magnitude and sometimes is less than 10^{-8} relative length change. Therefore for magnetostriction measurements the capacitance dilatometry is the method of choice. Slight changes of sample size causes the capacitance plates to alter their orientation therefore changing the capacitance (see Fig. 3). Modern three-terminal capacitance measurement bridges have high resolution, providing relative length change measurements with precision up to 10^{-9} in static fields up to

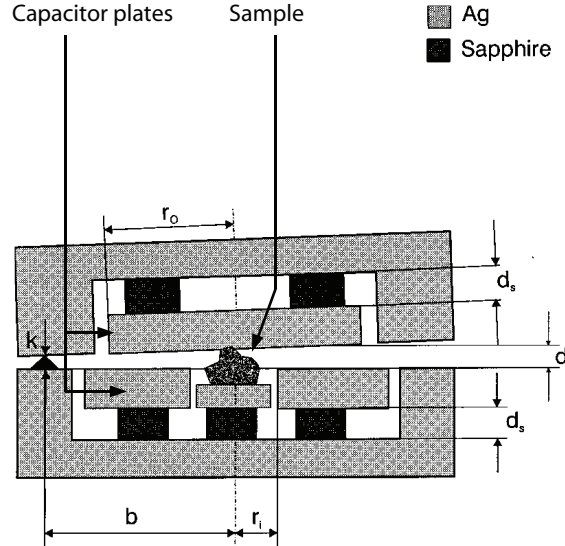


Figure 3: The principal scheme of a capacitance dilatometer. The thermal or magnetic field variation causes the black sample in the center of the dilatometer to change its relative length, thus changing the capacitance of the capacitor fixed around it [82].

45 T and in pulse fields up to 60 T. The modern miniature capacitance dilatometers are very small (sometimes as small as 2 – 3 cm) [81]. This allows magnetostriction experiments to be performed on a small single crystal specimen which are used for neutron and synchrotron scattering experiments.

2.2.3 Calorimetry

Specific heat capacity, also known simply as specific heat, is a measure of the heat energy required to increase the temperature of a unit quantity of a substance by a certain temperature interval. While disordered magnetic moments in the paramagnetic state hardly affect specific heat, within the antiferromagnetic state due to magnetic exchange energy the specific heat shows a significant magnetic contribution which is the thermal derivative of the magnetic exchange energy [83]. This magnetic contribution to the specific heat is very important specifically for magnetic studies of Gd^{3+} systems since some qualitative conclusions about magnetic structure can be made from specific heat measurements [9].

The specific heat is thermodynamically defined as

$$C_x = \lim_{dT \rightarrow 0} \left(\frac{dQ}{dT} \right)_x \quad (30)$$

where dQ is a heat input that causes a subsequent temperature rise dT in the sample. This definition is not very well suited for practical determination of the specific heat. Various approaches are used to determine the specific heat, depending on the sample and its conditions.

Since the studied systems are showing antiferromagnetic order at low temperature the specific heat measurements are limited to the temperature range $T < 300$ K. For measuring the specific heat of a solid bulk sample at low temperature the AC method [84, 85] or the thermal relaxation method [86] is used.

Throughout this thesis the relaxation calorimetry was the most common technique utilized for specific heat measurements. The typical relaxation calorimeter consists of an isolated platform which is attached by a weak thermal link to the heat sink or puck. The thermometer and heater are attached to the platform. During the measurement the puck is placed in an evacuated sample chamber. Prior to the sample measurement the heat capacity of an empty puck has to be measured. During the measurement (with or without sample) the platform is heated to a temperature $T = T_0 + \Delta T$ and then allowed to relax back to T_0 . The decay may be described by one or two exponential components (depending on the thermal link between sample and platform), this decay is recorded and fitted with a curve fitting procedure [87]. Independent studies confirmed that the precision of measurement is up to 1 % for temperatures above 5 K and 5 % for lower temperatures [88], however, there are some difficulties expected with determining absolute values of the specific heat in the vicinity of a first order transition [89].

3 Data Analysis and Modeling

3.1 Nuclear and magnetic scattering

The experiments performed in this thesis are scattering experiments on Gd based intermetallic compounds in a form of single crystal and polycrystalline materials (powders). Since the scattering and absorption cross sections depend on the wavelength of a neutron [90] the hot neutron wavelengths (0.4 - 0.6 Å) are used to reduce the effect of absorption. In order to analyze the measured scattering intensities some complications have to be taken into account.

Single crystal experiments involve independent measurements of each reflection produced by a bulk piece of crystal totally submerged in the neutron beam. This

method is called integrated intensities analysis and is performed as follows[91]. The calculated integrated intensity of a reflection h is

$$I_{int}(h) = SL(h)A(h)P(h)C(h)F^2(h) \quad (31)$$

where vector h labels the Bragg reflection (nuclear or magnetic), $L(h)$ is the Lorentz, polarization and multiplicity factors, S is the so called scale factor, $A(h)$ is the absorption correction, $F(h)$ is the structure factor⁸, $P(h)$ is the preferred orientation factor and $C(h)$ is the special set of corrections: no linearity, efficiencies, specific absorption corrections, extinction⁹. Because of the absorption problem mentioned above the integrated intensities measurement were performed on hot neutron single crystal diffractometers D3 and D9. The principal schematics of such a diffractometer is presented in Fig. 4

In order to refine the measured values with the structural model, for the integrated intensities the following quantity has to be minimized.

$$\chi^2 = \left| \sum_{i=1..n} \frac{1}{\sigma_{I_{mes}(h_i)}} (I_{mes}(h_i) - I_{int}(h_i, \alpha)) \right|^2 \quad (32)$$

here $I_{mes}(h_i)$ is the measured reflection intensity with error $\sigma_{I_{mes}(h_i)}$ at the position h_i and $i = 1..n$ is the number corresponding to the measured reflection. The $\alpha = \{\alpha_1, \alpha_2, ..\alpha_n\}$ is the parameter vector. It includes all the refined parameters which correspond to the nuclear and magnetic structures as well as the instrument specific corrections.

For a neutron scattering experiment on polycrystalline samples the intensities are analyzed as a function of scattering angle θ

$$I_{pow}(\theta) = S \sum_h I_{int}(h)\Lambda(h) + b(\theta) \quad (33)$$

where h labels the Bragg reflection (nuclear or magnetic), S is the scale factor, $b(\theta)$ is the background intensity and $\Lambda(h)$ is the reflection profile function that includes both sample and instrument specific corrections¹⁰ The powder experiments have been performed on a hot neutron diffractometers D4 and 7C2. The principle schematics is presented in Fig. 5.

⁸Debye-Waller factor, also known as temperature factor, is included within the structure factor $F(h)$.

⁹The exact list of the corrections is listed individually for each compound in their respective chapters.

¹⁰Systematic line-shifts like Bragg-Brentano parafocusing arrangement or Debye-Scherrer geometry, peak shape profile and its asymmetry, and specific absorption are the most commonly included factors contributing the reflection profile $\Lambda(h)$.

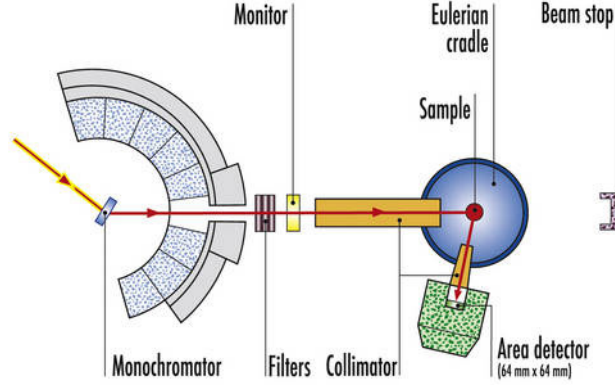


Figure 4: The schematic representation of the hot neutron diffractometer D9. Picture taken from [92]

In the case of powder refinement the equation (32) has a similar form but h is to be substituted with θ

$$\chi^2 = \left| \sum_{i=1..n} \frac{1}{\sigma_{I_{mes}(\theta_i)}} (I_{mes}(\theta_i) - I_{pow}(\theta, \alpha)) \right|^2 \quad (34)$$

here $I_{mes}(\theta_i)$ is the measured scattering intensity with error $\sigma_{I(\theta_i)}$ at the scattering angle θ_i and $i = 1..n$ is the number of the corresponding measurement of the diffraction pattern. The method presented for powder diffraction is named Rietveld refinement after the author of this method which was first described in detail in [93].

3.2 Mean-Field model

The experimental studies on different rare earth based compounds mentioned in section 2 provide experimental data on which theoretical investigations of magnetic properties in general can be based.

As discussed in section 1.1 according to the standard model of rare earth magnetism [1] for a $4f$ Gd^{3+} system there is no single ion anisotropy to the first order in the crystal electric field. The first term in the magnetic Hamiltonian (6) is to be dropped resulting in the Hamiltonian being a sum of isotropic exchange-, the classical dipolar- and the Zeeman interactions [8]:

$$\mathcal{H} = -\frac{1}{2} \sum_{ij} \mathcal{J}(ij) \mathbf{J}_i \mathbf{J}_j - \frac{1}{2} \sum_{ij\alpha\beta} (g_J \mu_B)^2 D_{ij}^{\alpha\beta} J_i^\alpha J_j^\beta -$$

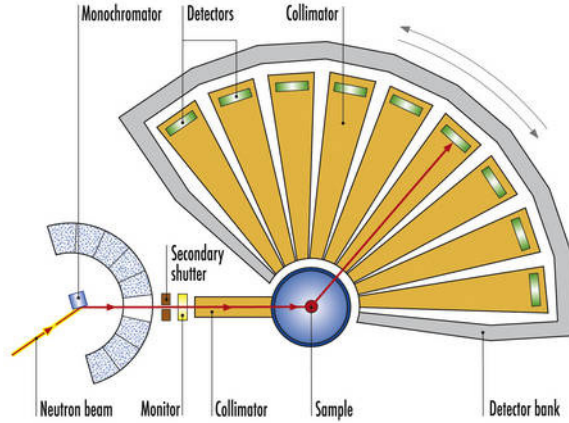


Figure 5: The schematic representation of the hot neutron diffractometer D4. Picture taken from [92]

$$- \sum_i g_J \mu_B \mathbf{J}_i \mathbf{H} \quad (35)$$

Here \mathbf{J}_i denotes the negative of the angular momentum operator of the i^{th} Gd ion, g_J the Landé factor and μ_B the Bohr magneton. Numbers i and j denote all Gd ions while $\alpha, \beta = 1, 2, 3$ for three spatial directions of the crystal.

Provided that the position vectors \mathbf{R}_i of the Gd ions are known from the crystallographic structure, the classical dipolar interaction constants $D_{ij}^{\alpha\beta}$ can be calculated:

$$D_{ij}^{\alpha\beta} = \frac{3(R_i^\alpha - R_j^\alpha)(R_i^\beta - R_j^\beta) - \delta_{\alpha\beta} |\mathbf{R}_i - \mathbf{R}_j|^2}{|\mathbf{R}_i - \mathbf{R}_j|^5} \quad (36)$$

Hamiltonians like (40) may induce complex magnetic properties and numerical simulations are required to make a prediction which can be directly compared to experimental data. In order to do so, the two ion interaction parameters $\mathcal{J}(ij)$ have to be determined. In principle this can be done by measuring the dispersion of magnetic excitations using inelastic neutron scattering on single crystals. However, in the present case the high absorption cross section of Gd does not permit this approach. An alternative way of obtaining the $\mathcal{J}(ij)$ would be an ab initio model or model functions like Bethe-Slater, free electron RKKY (demonstrated for GdCu_6 case) etc. For simple crystallographic structures an indirect approach for an estimation of several $\mathcal{J}(ij)$ parameters (for several pairs of neighbors ij) from experimentally obtained quantities can be implemented.

In order to minimize the free energy of the Hamiltonian (40) the Fourier transform of the spin - spin exchange expressed as:

$$\mathcal{J}_{\alpha\beta}(\mathbf{Q}) = \sum_{ij} \left(\mathcal{J}_{\alpha\beta}(ij)\delta(\alpha\beta) + (g_J\mu_B)^2 D_{ij}^{\alpha\beta} \right) e^{-i\mathbf{Q}(\mathbf{R}_i - \mathbf{R}_j)} \quad (37)$$

will have a maximum of its largest eigenvalue at the propagation vector τ of the antiferromagnetic structure [1]. Since the dipolar term in equation (37) can be directly calculated via (36) and is often negligibly small comparing to the spin-spin exchange the maxima of equation (37) gives an estimate of a value of $\mathcal{J}(Q = \tau)$ at low temperatures via the relation:

$$T_N \cong \frac{\mathcal{J}_{\alpha_{max}}(\mathbf{Q} = \tau)J(J+1)}{3k_B} \quad (38)$$

Here $J = \frac{7}{2}$ is the angular momentum quantum number of the Gd^{3+} ion, $\mathcal{J}_{\alpha_{max}} = \max(\mathcal{J}_{11}, \mathcal{J}_{22}, \mathcal{J}_{33})$, k_B is Boltzmann's constant and T_N is the Néel temperature of antiferromagnet obtained experimentally.

The other characteristic quantity of an antiferromagnet obtained experimentally is the paramagnetic Curie temperature. Within the mean field theory it is related to the magnitude of the Fourier transform of the exchange at $Q = 0$ i.e. $\mathcal{J}_{\alpha\alpha}(Q = 0)$:

$$\theta_\alpha = \frac{\mathcal{J}_{\alpha\alpha}(Q = 0)J(J+1)}{3k_B} \quad (39)$$

Here $\theta_{\alpha=a,b,c}$ denotes the estimated paramagnetic temperature from paramagnetic susceptibility measured along α crystallographic direction.

The relations above directly relate experimental data to sums of exchange constants and thus can be used for the determination of the exchange interaction¹¹. The obtained parameters $\mathcal{J}(ij)$ can be then used to minimize the energy of the Hamiltonian (40) numerically. Throughout this thesis mean field numerical calculations have been performed with the help of McPhase program package [94].

For a given exchange $\mathcal{J}(ij)$ the McPhase program selfconsistently calculates different magnetic moment configurations according to some initial spin configuration and propagation vectors defined by user. The mean field approximation is used in order to minimize the free energy of each of the possible magnetic moment configurations. The magnetic moment configuration with the lowest free energy is used as a resulting structure for the given exchange $\mathcal{J}(ij)$.

Once the structure with the lowest free energy matches the structure predicted by neutron and magnetic x-ray scattering experiments (see section 3.1) the Hamiltonian (40) is recalculated for different sets of temperatures and external fields.

¹¹This exact procedure is strongly dependent on the lattice structure of the studied compound and will be discussed specifically for GdRu_2Si_2 in the following chapter.

In such a way the microscopic magnetic properties can be directly compared with experimentally measured macroscopic bulk properties.

The flexibility of the McPhase¹² program package allows the magnetization, specific heat, magnetic susceptibility and magnetostriction¹³ to be calculated.

After all the experimentally observed magnetic properties reach reasonable agreement with the calculation a parametrized model for a specific compound is assumed to be found, otherwise a new set of exchange parameters $\mathcal{J}(ij)$ is to be tested or a different model Hamiltonian can be used and the described procedures will be repeated accordingly.

In this way complex experimental data can often be estimated by simple Hamiltonians. If this is not possible indications for the nature of more complex magnetic interactions have to be considered.

4 GdRu₂Si₂

4.1 Introduction

GdRu₂Si₂ is a ThCr₂Si₂ - type tetragonal antiferromagnet (space group I4/mmm). Its magnetic properties have been well studied. At high temperatures the thermal variations of the reciprocal paramagnetic susceptibility along the three main crystallographic axes show negligible anisotropy [95]. From equation (39) and available data on magnetic susceptibility it follows that no anisotropic bilinear exchange interaction $\mathcal{J}_{\alpha\beta}(\mathbf{Q})$ is present at $\mathbf{Q} = 0$ in this S-state tetragonal compound [96]. Below $T_N = 47$ K the thermal variation of the susceptibility along the different axes shows a noticeable anisotropy between the c axis and the basal plane. This anisotropy is also observed in the field dependence of magnetization, which also shows an additional unexpected phase transition. Moreover susceptibility data suggests a phase transition at $T_r=40$ K. Summarizing all these facts, GdRu₂Si₂ is a perfect candidate for the study of spin-spin interactions in general and anisotropic exchange in particular.

Therefore, an investigation of the magnetic structure has been performed using scattering techniques and a detailed analysis of magnetic properties with computational methods is presented in this chapter.

¹²For further details please consult the McPhase manual at <http://www.mcphase.de/>

¹³The calculation of magnetostriction involves a priori knowledge of elastic and magnetoelastic constants

4.2 Sample preparation

GdRu₂Si₂ polycrystalline powder was prepared by an arc-melting technique from bulk pieces of high purity components (Gd - 3N, Ru - 4N and Si - 5N). Stoichiometric GdRu₂Si₂ was repeatedly arc-melted on a water cooled copper crucible under Zr gettered Ar atmosphere (IFW, Dresden). To ensure a better homogeneity, the sample was annealed at 900 ° for 48 hours. The purity of the sample has been checked with x-ray diffraction. The single-crystal of GdRu₂Si₂ was grown using the Czochralski technique in a tri-arc furnace (DCMP, Charles University Prague). About 6 g of high-purity constituents (Gd - 3N, Ru - 4N, Si - 6N) were melt in stoichiometric composition directly in the copper crucible in the tri-arc furnace. The resulting mixture was subsequently kept at constant temperature for about 2 hours to ensure complete reaction of the components. The crystal was grown on a sharp tungsten seed at the typical speed of 8 mm per hour with simultaneous rotation of both the seed and the crucible (4 - 6 rotations per minute). The final ingot was 15 mm long, with a maximum diameter of 3mm, and 0.8 mm diameter in the neck part. The rather small size of the resulting crystal was mediated by the high-melting point of the compound, therefore, only 6 g of melt could be used due to the limited maximum power and relevant configuration of the arcs. The phase composition of the grown crystal was verified using X-ray powder diffraction and microprobe analysis (Gd_{0.97}Ru_{2.00}Si_{1.98}). The crystallinity and the crystallographic orientation of the ingot for further experiments was investigated by standard Laue technique.

4.3 Bulk measurements

A characteristic x-ray radiation of wavelength $\lambda = 1.7889 \text{ \AA}$ was used to investigate the crystallographic structure on powder. A secondary monochromator was used between the sample and the detector in order to eliminate the K_{β} lines. The 2Θ position of the reflections was corrected using reflections from Ge powder, which was mixed with the sample. Multiple x-ray diffraction patterns were obtained from 10K up to room temperature with steps of 10 K in order to determine the thermal expansion [97]. The thermal expansion and magnetostriction were measured using a miniature capacitance dilatometer [81], implemented in a commercial PPMS machine (Quantum Design's Physical Property Measurement System), capable of controlling the sample environment conditions in the temperature range 2-350 K and magnetic fields up to 14T. Thermal expansion and magnetostriction were measured for fields applied along the a and c directions, both in longitudinal and transversal geometry. Temperature scans were done at a sweep rate of 0.1-0.2 K/min. For the investigation of magnetostriction the field sweep was interrupted in the vicinity of the field induced transitions, otherwise a field sweep of 40 Oe/s

was used. The same PPMS machine was used for specific heat measurements with the double-relaxation technique. A small flat fragment (8 mg) of single crystal was used for this measurement. The lattice contribution to the specific heat was estimated using the data obtained from the measurement of the non-magnetic LaRu_2Si_2 .

The thermal variation of lattice constants is represented in Fig. 4.5. The x-ray data (taken from [97, 82]) is confronted with the dilatometric measurements and a Debye fit to the high temperature (phonon dominated) thermal expansion data. It is clearly visible, that below the Néel temperature T_N , the cell dimensions are affected by the antiferromagnetic ordering. Longitudinal and transversal magnetostriction measurements in applied magnetic fields along a and c were performed for lattice directions a , b and c below the Néel temperature. The results are presented in Fig. 7 and 8. For the field along the c direction the magnetostriction suggests one field induced transition (possibly spin flip) at $H_f^{[001]} = 2.1 \text{ T}$. On the other hand the change in the lattice constants with magnetic field applied along a shows two magnetic induced transitions (both of spin flop nature) at $H_{f1}^{[100]} = 2.1 \text{ T}$ and $H_{f2}^{[100]} = 4.0 \text{ T}$. The field dependence of the lattice constant in higher fields ($\leq 9 \text{ T}$) suggests the saturation fields $H_s^{[100]} \approx 10.7 \text{ T}$ and at $H_s^{[001]} \approx 9 \text{ T}$, which is in accordance with the values reported in literature [95].

The lattice constants a and b appear to be equal below T_N , thus stating that no orthorhombic distortion is observed in zero field. This particular fact was verified by measuring the peak splitting of certain reflections of the x-ray diffraction pattern. No splitting was observed within the experimental resolution. Note that for a magnetic propagation vector not along c (see below) a peak splitting is expected. This discrepancy is found in several other Gd systems and called magnetoelastic paradox [97, 98]. New high resolution dilatometric measurements (Figs. 7 and 8) show that an orthorhombic distortion is present in non-zero field (e.g. $\Delta a/a$ and $\Delta b/b$ are not equal for $H \parallel [100]$). Moreover, field measurements show that the lattice exhibits a small magnetocrystalline irreversibility. This, however, could be attributed to difficulties experienced with dilatometric measurements under applied fields on anisotropic samples as described in [80]. In magnetostriction signals a repopulation of magnetic domains may be of importance, but the data on magnetic domain population in this compound is not available. Due to the small magnitude of magnetoelastic effect a detailed study of the magnetoelastic Paradox in this system by means of diffraction methods is not possible or extremely difficult.

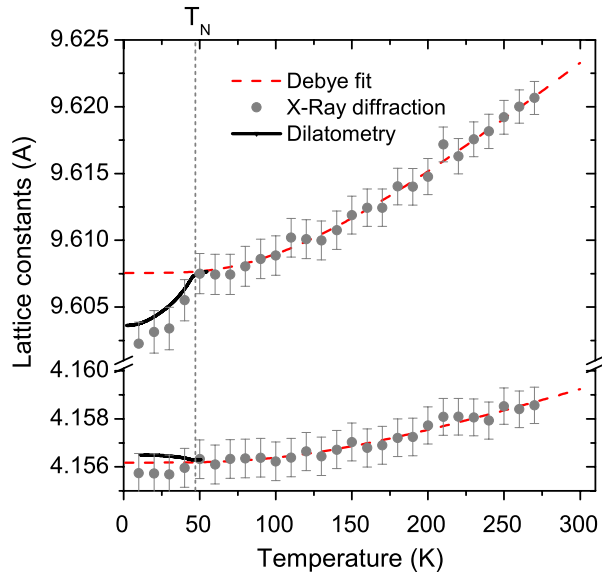


Figure 6: Thermal expansion in zero field measured by dilatometry (solid line) compared to lattice constants measured with x-ray (dots), taken from [97] and calculated Debye approximation (dashed line).

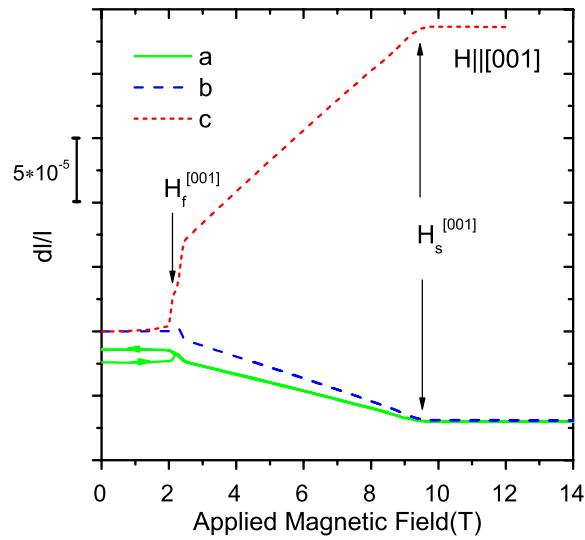


Figure 7: Magnetostriction measured along main crystallographic directions with respect to the magnetic field applied along the (c)-axis. The experimental error is contained within the line width.

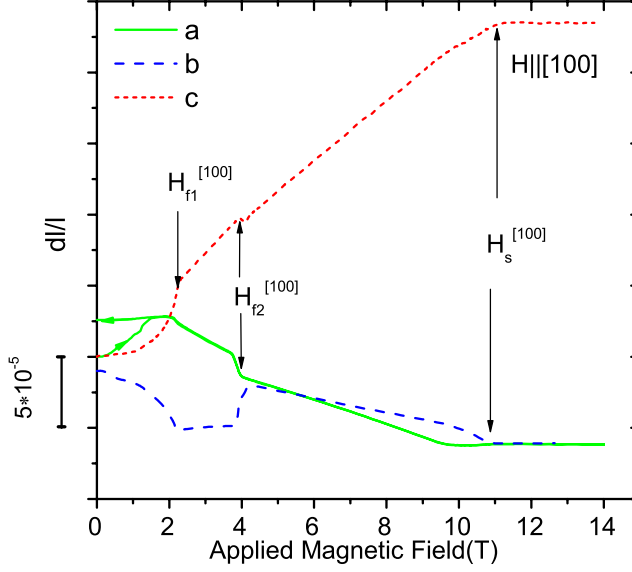


Figure 8: Magnetostriction measured along main crystallographic directions with respect to the magnetic field applied along the (**a**)-axis. The experimental error is contained within the line width.

4.4 Neutron diffraction

Due to the high neutron absorption cross-section of natural Gd for thermal neutrons the magnetic structure was studied using hot neutrons. The powder diffraction patterns were collected at the 7C2 instrument at LLB, Saclay [8, 99]. A neutron wavelength of 0.57 \AA was selected by a Ge (311) monochromator. In order to reduce absorption the powder was placed in a vanadium annular sample holder. Two diffraction patterns were collected at temperatures of 2.3 K and 60 K with a counting time of 9 hours. An empirical background was estimated from the neutron diffraction pattern of a fully absorbing sample (cadmium foil) and an empty sample holder using the following formula: $I_{bkg} = I_{cd} + k(I_{empty} - I_{cd})$ where $k = 0.362$ is an estimated constant. Because of the resonance effects in natural Gd the neutron scattering cross section is wavelength dependent. For neutron energies of about 0.25 eV the effective coherent cross section of 10.2 fm (with real part of 9.99 fm and -0.82 fm as imaginary part) was used [90]. For Ru and Si standard values of 7.03 fm and 4.149 fm were used. The results of the powder refinements show a nuclear structure with a tetragonal lattice with lattice parameters $a = b = 4.168(9) \text{ \AA}$ and $c = 9.626(2) \text{ \AA}$ (See Table 8 for details) Neutron diffraction data at low temperature clearly shows the presence of a long period, possibly incommensurate magnetic structure. A scripting interface was written for

the FullProf package in order to resolve the magnetic structure. Given the experimental resolution different antiferromagnetic configurations within $10 \times 10 \times 10$ crystallographic unit cells were sequentially introduced to the FullProf program to calculate the diffraction pattern. The simulated configurations are all those commonly observed in rare-earth antiferromagnets and include collinear structures, amplitude modulated structures as well as a set of cycloids with moments aligned along different directions. This analysis shows that the most probable magnetic structure is either cycloidal in the (\mathbf{bc}) plane or a collinear structure with moment at 45° from \mathbf{b} and \mathbf{c} axes with $(0.25 \ 0 \ 0)$ propagation vector (see Fig. 9).

The single crystal diffraction experiment was performed on the D9 instrument at ILL, Grenoble. A neutron wavelength of 0.51 \AA was selected by a Cu (220) monochromator. Selected magnetic reflections were measured at temperatures of 2 K and 43 K in order to study the magnetic structure of two different phases observed in this compound. The reflection intensities were integrated from a two dimensional multidetector data. High absorption of natural Gadolinium in combination with inhomogeneity and divergence of the beam does not allow the correct estimation of the absorption for different scattering conditions. The single crystal experiment leads to a more precise determination of the propagation vector of $\tau = (0.22 \ 0 \ 0)$ (see Fig. 10). The wide area q-scans show that within the experimental error no higher order harmonics have been found suggesting a non collinear structure.

Table 8: Results of refinement of atomic positions with Rietveld refinement.

Atom	Wyckoff index	X	Y	Z	Temperature factor (\AA^2)
Gd	2a	0	0	0	0.133(1)
Ru	4d	0	0.5	0.25	0.442(8)
Si	4c	0	0	0.376(8)	0.792(2)

4.5 Magnetic X-Ray Scattering

The x-ray resonant magnetic scattering experiment has been performed on a GdRu_2Si_2 single crystal at the MU-CAT 6-ID-B beamline, APS Argonne, USA. The sample with a polished surface perpendicular to the a -axis and a size of $2 \text{ mm} \times 2 \text{ mm}$ has been mounted on a cold finger of a dispex cryostat. The resonance enhancement at the Gd L_2 absorption edge has been employed at an energy of 7.932 keV. The $\sigma \rightarrow \pi$ polarization geometry has been carried out using a PG

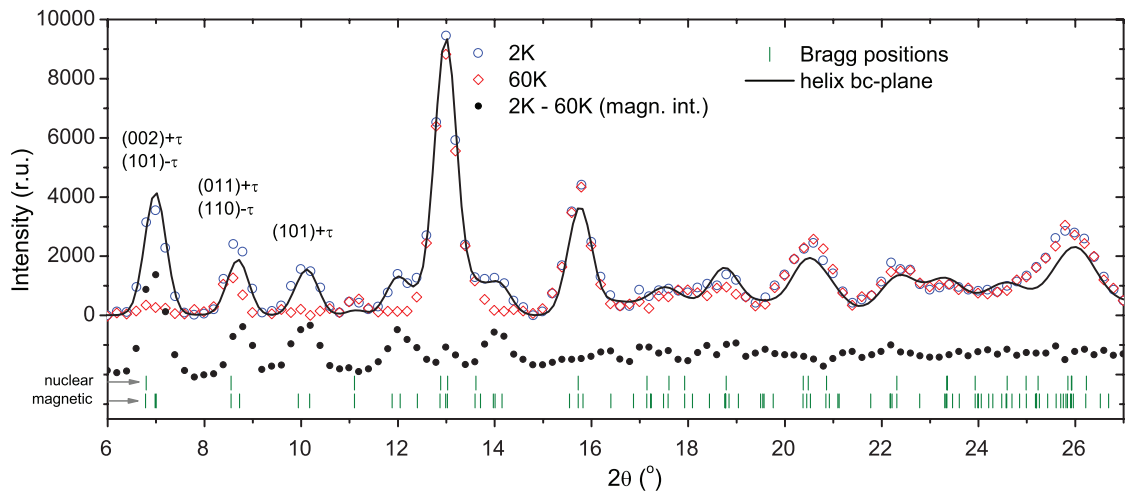


Figure 9: Hot neutron diffraction data obtained at 7C2, Saclay. Red diamonds and blue open circles correspond to experimental data measured above and below the ordering temperature respectively. Black closed circles below represent the difference between high and low temperature spectra. Paramagnetic scattering has been subtracted from the high temperature spectrum. The lines represent calculated intensities for different magnetic configurations.

(006) analyzer. The **(ab)** and the **(ac)** plane have been selected alternatively as scattering planes by azimuth rotation around the a direction.

In Fig.11, the temperature dependence of the intensity of the magnetic $(200)-\tau$ reflection is shown for both scattering planes correlated to the temperature dependence of the incommensurate propagation vector. Below the Néel transition $T_N = 47$ K, the intensity increases strongly in the **(ac)** scattering plane with decreasing temperature in contrast to a very slight increase for the **(ab)** scattering plane. Below $T_r = 40$ K, the situation changes. Now the intensity in the **(ab)** scattering plane increases stronger than in the **(ac)** scattering plane. Both curves converge near 35 K and show a similar temperature dependence below 35 K. This behavior conforms to the results of the azimuth scans. Whereas at $T = 42$ K maxima for the scattering coincident with the **(ac)** plane and minima for the **(ab)** plane, respectively, were observed, there is no significant dependence of the scattering intensity on azimuth rotation at $T = 7$ K. This observation is consistent with a mainly collinear alignment of the Gd moments in the c direction close to the Néel transition. At low temperatures, a similar size of the ordered magnetic Gd moments in the b and c direction can be concluded. The lack of higher order harmonics suggests a helical structure as ground state. The temperature dependence of the propagation vector τ indicates likewise the second phase transition at $T_r = 40$ K. Whereas below T_r the value of ξ in $\tau = (\xi 00)$ decreases continuously with

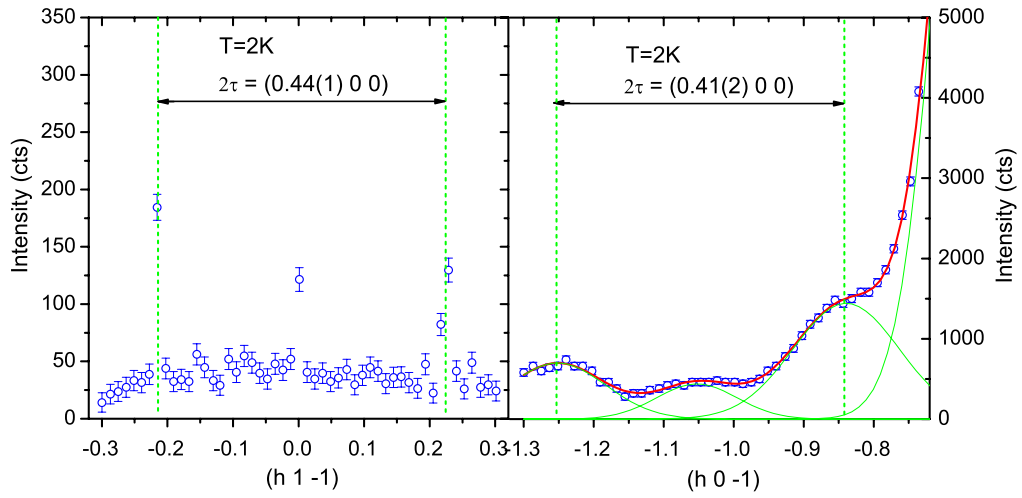


Figure 10: Hot neutron diffraction data obtained at D9, ILL Grenoble. Dots correspond to experimental data measured at 2K. The vertical dashed lines represent the estimated peak position for the $(01\bar{1}) \pm \tau$ reflections on the left and fitted peak positions for the $(\bar{1}0\bar{1}) \pm \tau$ reflections on the right. The peak around the $(0.70\bar{1})$ is background related and is temperature independent. The significant difference of the half width of the peaks is an instrument resolution effect and is attributed to the respective orientation of the scattering vector to the direction of the scan.

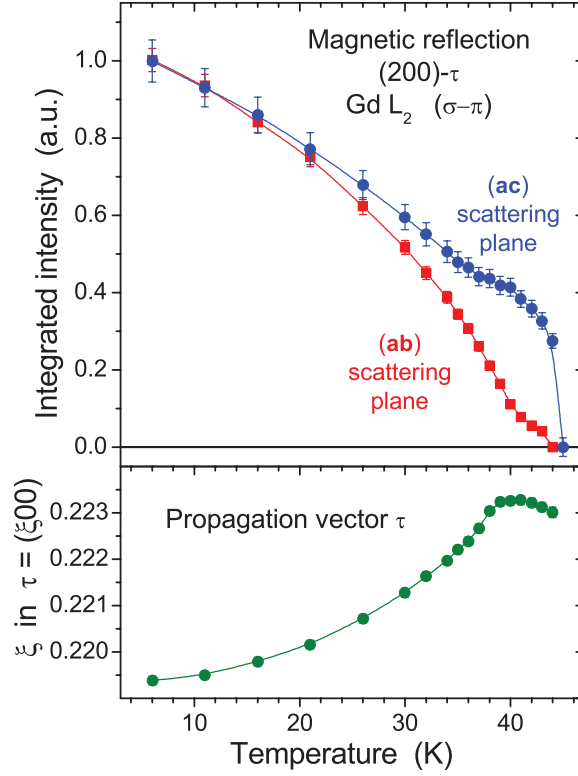


Figure 11: Temperature dependence of the integrated intensity of the $(2\ 0\ 0)\text{-}\tau$ magnetic satellite reflection and of the propagation vector determined by resonant magnetic scattering. The intensity is determined by rocking scans. The propagation vector is based on the positions of the pair of magnetic satellites $(2\ 0\ 0)\pm\tau$ in longitudinal scans.

decreasing temperature, the value ξ is nearly constant above T_r .

The result of the magnetic x-ray experiment shows a clear correspondence to the neutron data, indicating that the most conclusive structure from different neutron and magnetic x-ray observations is a cycloid with moments in the (bc) plane, followed by a collinear amplitude modulated structure above $T_r = 40$ K with moments parallel to c . The most precise determination of propagation vector by magnetic x-ray is shown in Fig. 11.

4.6 Model A: Standard model for Gd Magnetism

4.6.1 Hamiltonian

According to the standard model for a $4f$ Gd^{3+} system there is no single ion anisotropy and the magnetic Hamiltonian ‘is a sum of isotropic exchange-, the

classical dipolar- and the Zeeman interactions [8].

$$\begin{aligned} \mathcal{H} = & -\frac{1}{2} \sum_{ij} \mathcal{J}(ij) \mathbf{J}_i \mathbf{J}_j - \frac{1}{2} \sum_{ij\alpha\beta} (g_J \mu_B)^2 D_{ij}^{\alpha\beta} J_i^\alpha J_j^\beta - \\ & - \sum_i g_{J_i} \mu_B \mathbf{J}_i \mathbf{H} \end{aligned} \quad (40)$$

Here \mathbf{J}_i denotes the angular momentum operator of the i^{th} Gd ion, g_J the Landé factor and μ_B the Bohr magneton.

Provided that the position vectors \mathbf{R}_i of the Gd ions are known from the crystallographic structure, the classical dipolar interaction constants $D_{ij}^{\alpha\beta}$ can be calculated via equation (36)

4.6.2 Numerical simulation

GdRu₂Si₂ is a relatively simple symmetric system with only one atom in the primitive unit cell. This significantly reduces the amount of unknown parameters in $\mathcal{J}(ij)$. An estimate of the interaction constants for several nearest neighbors becomes sufficient to reproduce the experimentally observed magnetic structure. Such an estimation was made by solving a set of equations and inequalities, which can be derived from experimental data such as the Néel temperature, the propagation vector, etc., within the framework of mean field theory. In the following this procedure will be demonstrated neglecting the (small) influence of the dipolar interaction for the moment. In this approach, the Néel temperature T_N and the paramagnetic Curie temperature θ can be expressed via equations (38, 39) while the saturation field H_s for the transition of the antiferromagnetic to the field induced ferromagnetic state can be expressed as follows ($J = S = 7/2$) [1, 100]:

$$H_s = \frac{J(\mathcal{J}(\tau) - \mathcal{J}(0))}{g_J \mu_B} \quad (41)$$

Here $\tau = (0.22 \ 0 \ 0)$ denotes the propagation vector of the magnetic structure and k_B the Boltzmann's constant. $\mathcal{J}(\mathbf{Q})$ is the Fourier transform of the exchange, which is the simplified form of (37):

$$\mathcal{J}(\mathbf{Q}) = \sum_j \mathcal{J}(ij) e^{-i\mathbf{Q}(\mathbf{R}_i - \mathbf{R}_j)} \quad (42)$$

In the case of GdRu₂Si₂ the following values of the Fourier transform of the exchange have been obtained from equations (38) and (39) using $T_N = 47$ K and $\theta = 38.4$ K [95]: $\mathcal{J}(\tau) = 771 \mu eV$ and $\mathcal{J}(0) = 636 \mu eV$. Using these values in equation (41) would give a value of $H_s = 4.25$ T. The experimentally determined

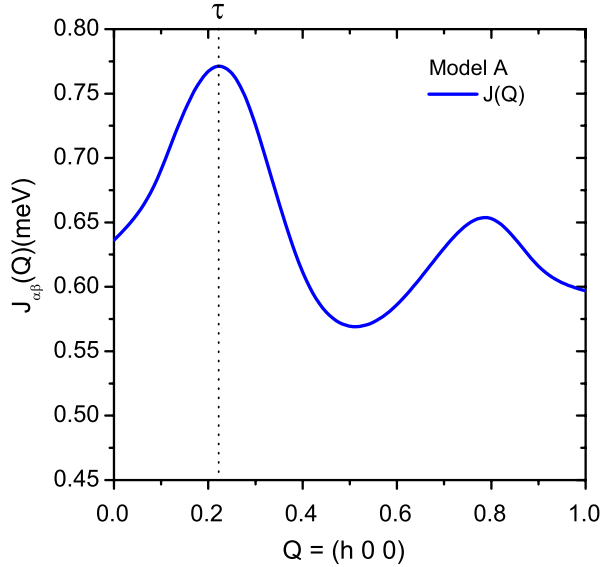


Figure 12: Fourier transformation $\mathcal{J}(\mathbf{Q})$ of the interaction tensor $\mathcal{J}(ij)$ defined in Table 9.

saturation field value is twice bigger than this theoretical value [95]. Within this standard model approach this discrepancy cannot be resolved, whichever set of parametrisation of the Hamiltonian (40) is chosen. Therefore, in the evaluation of this model we did not consider equation (41) and only used equations (38) and (39). In addition, the experimentally determined value of the propagation vector $\tau = (0.223 \ 0 \ 0)$ is taken into account: the Fourier transform of $\mathcal{J}(\mathbf{Q})$ (e.g equation (42)) of the interaction tensor $\mathcal{J}(ij)$ should have a maximum at the propagation vector τ [1]. This condition implies that the derivatives $\frac{d}{dh}\mathcal{J}(\mathbf{Q})$, $\frac{d}{dk}\mathcal{J}(\mathbf{Q})$ and $\frac{d}{dl}\mathcal{J}(\mathbf{Q})$ are zero at $\mathbf{Q} = \tau$. Putting all three derivatives zero and applying equation (37) in general gives three linear equations for the interaction parameters $\mathcal{J}(ij)$. However, if τ is in a symmetry plane or in a symmetry direction some of these equations are automatically fulfilled or linear dependent. In our special case τ is along $(h00)$ and there is only one independent equation, which may be used for the determination of the interaction constants $\mathcal{J}(ij)$:

$$\frac{d}{dh}\mathcal{J}(\mathbf{Q}) = 0 \quad (43)$$

We are therefore left with equations (38), (39) and (43) and some inequalities from the second derivatives. Whilst investigating this system of equations and inequalities it can be shown, that no solution exist unless interaction constants

up to the sixth neighbor or more are taken into account. Several similar sets of parameters have been obtained. In order to ensure that the maximum of the Fourier transform at $\mathbf{Q} = \tau$ is not only a local but a global maximum a numerical calculation of $\mathcal{J}(\mathbf{Q})$ was carried out for the whole Brillouin zone for each set of parameters. In this way we arrived at a some sets of interaction parameters, for which the magnetic properties have been calculated. One of these parameter sets will be discussed in the following and is listed in table 9. Figure 12 shows the corresponding Fourier transform $\mathcal{J}(\mathbf{Q})$ for \mathbf{Q} along (h 0 0). The maximum at $\mathbf{Q} = \tau$ can be clearly seen.

Table 9: Exchange interaction for different neighbors for the case of isotropic exchange. (According to the Standard Model)

Neighbor	Distance (Å)	$\mathcal{J}(ij)(\mu\text{eV})$
100	4.165	218.89
$\frac{1}{2}\frac{1}{2}\frac{1}{2}$	5.654	10.00
110	5.89	-94.45
$\frac{1}{2}\frac{3}{2}\frac{1}{2}$	8.165	-1.88
200	8.33	-45.67
001	9.654	135.6

In order to take into account the effect of the classical dipolar interaction 329 interaction constants $D_{ij}^{\alpha\beta}$ were calculated (all neighbors within 20Å radius were taken into consideration). The long range nature of this interaction has to be taken into account for $q \neq 0$, at finite q this procedure is a good approximation.

Based on this parametrization of the Hamiltonian (40) a numerical calculation of the magnetic properties was performed using the *McPhase* program package [101], [94], ¹⁴. At a given temperature (magnetic field) a magnetic structure was stabilized by a mean field algorithm in combination with a free energy minimization process. Magnetic supercells and initial spin configurations have been generated by a set of q-vectors in combination with a Monte Carlo process.

4.6.3 Discussion of Model A

At low temperatures a single-q helical magnetic structure with propagation vector of $(2/9 \ 0 \ 0) = (0.222 \ 0 \ 0)$ ¹⁵ and moments in the *bc* plane was calculated. The propagation vector is temperature and field independent and in the vicinity of the

¹⁴<http://www.mcphase.de>

¹⁵Due to the specifics of the numerical method the McPhase program can only handle commensurate unit cells. Therefore within the limitation of 20x20x20 nuclear unit cells $(2/9 \ 0 \ 0)$

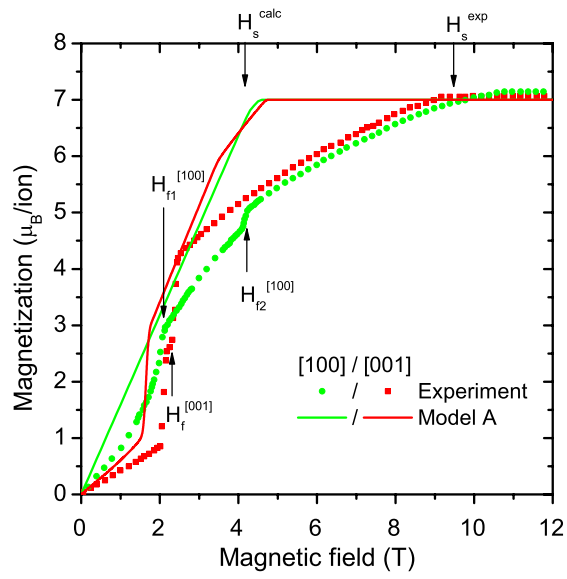


Figure 13: Magnetization along different crystallographic directions. Dots represent measured curves [95]. The dashed line represents the calculated magnetization for the system with Hamiltonian (40) and exchange interaction tensor $\mathcal{J}(ij)$ taken from Table 9.

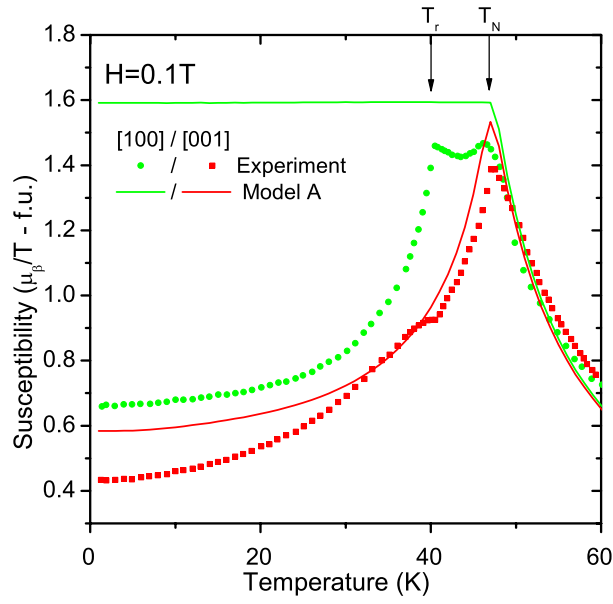


Figure 14: Magnetic susceptibility along main crystallographic directions. Dots represent measured curves [95]. Solid lines represent calculated susceptibility along different crystallographic directions for the system with Hamiltonian (40) and exchange interaction tensor $\mathcal{J}_{\alpha\beta}(ij)$ taken from Table 9.

ordering temperature a change into a collinear amplitude modulated structure with moments along [010] is predicted. The temperature region of this phase is very small in temperature (0.5 K) due to the small magnitude of the dipolar anisotropy (about $7\mu\text{eV}$), which tends to align the moments along [010] [8]. The temperature and field dependence of the magnetic structure was calculated allowing a prediction of the magnetization and susceptibility. The results of this calculation are compared to experimental data in figures 13 and 14. The mean field Monte-Carlo calculations are in total agreement with the estimation of the critical field (equation (41)), which does not agree with the experiment in this model. As can be seen from the susceptibility the antiferromagnetic ordering occurs below $T_N = 47$ K. As stated in [8] the anisotropic classical dipolar interaction suggests a collinear amplitude modulated structure just below the ordering temperature. For the dipolar interaction described by equation (36) the preferred direction is calculated to be along [010]. This is in contrast to the results of the magnetic x-ray experiment which states the moments to be along [001] near the ordering temperature. This experimentally observed anisotropy excludes the possibility of multiple-q order (as postulated for $\text{GdNi}_2\text{B}_2\text{C}$ in [100]). For this reason in further simulations only single-q magnetic structures were considered. By the order of magnitude for the closest neighbor the exchange interaction appears to be about 100 times stronger than the classical dipolar interaction for this compound. This is the reason why the transition temperature T_r between collinear and cycloid structure is predicted to be only about 0.5 K below the Néel temperature. This is in contrast to the experimental value of $T_r = 40$ K. Thus we conclude that a more significant source of anisotropy than the classical dipolar interaction needs to be considered in the Hamiltonian.

4.7 Model B: Biquadratic exchange

4.7.1 Hamiltonian

In order to resolve the discrepancy between the observed and calculated critical field values it was attempted to introduce isotropic biquadratic exchange. The biquadratic exchange has been postulated in the Gd^{3+} systems before [102]. It was however not to be expected to be confirmed by neutron scattering without polarization analysis due to the low experimental resolution [103].

The generalized form of Hamiltonian that was used to calculate the magnetic properties with a biquadratic term is:

is the closest commensurate magnetic configuration to (0.22 0 0) determined by the Magnetic X-Ray experiment)

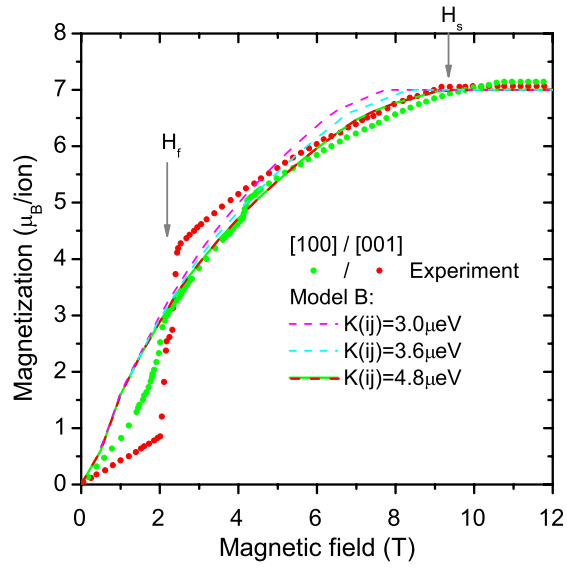


Figure 15: Magnetization along different crystallographic directions. Dots represent measured curves [95]. The lines represent the calculated magnetization for the system with Hamiltonian (44) and exchange interaction $\mathcal{J}(ij)$ taken from Table 10 and biquadratic exchange $K(ij)$ for the nearest neighbor 100 is being varied (see legend).

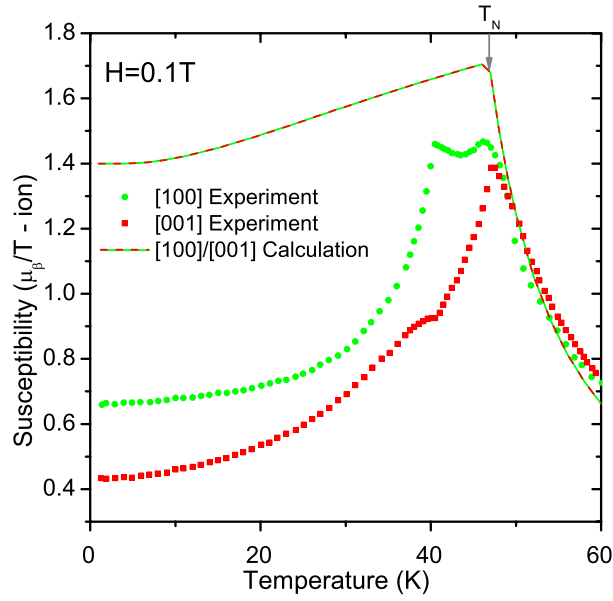


Figure 16: Magnetic susceptibility along main crystallographic directions. Dots represent the measured curves [95]. Solid lines represent the calculated susceptibility along different crystallographic directions for the system with Hamiltonian (40), where exchange interaction tensor $\mathcal{J}_{\alpha\beta}(ij)$ and biquadratic exchange $K(ij)$ are taken from Table 10.

$$\mathcal{H} = -\frac{1}{2} \sum_{ij} \mathcal{J}(ij) \mathbf{J}_i \mathbf{J}_j - \sum_i g_J \mu_B \mathbf{J}_i \mathbf{H} - \frac{1}{2} \sum_{ij} K(ij) (\mathbf{J}_i \mathbf{J}_j)^2 \quad (44)$$

where in addition to model A (section 4.6) the last term $K(ij)$ describes the biquadratic interaction.

4.7.2 Numerical simulations

The effective bilinear interaction has been kept the same and a nearest neighbor biquadratic interaction has been introduced. The corresponding numerical values of $\mathcal{J}(ij)$ and $K(ij)$ are shown in Table 10. The numerical calculations were performed in the same way as described in section 4.6. The only difference is that in the meanfield approach in addition to the angular momentum components $\langle J_i \rangle$ the expectation values of $\langle O_2^m \rangle$ have been also considered. Values of $K(ij)$ for the nearest neighbor have been varied from 3 to 5 μeV in order to obtain a reasonable value of the saturation field H_s .

Some of the results of magnetization calculations are presented in Figure 15 along the experimental data. Values of $\mathcal{J}(ij)$ and $K(ij)$ obtained for the best model are listed in Table 10 and were used to calculate the magnetic susceptibility which is presented alongside experimental data on Fig. 16.

Table 10: Isotropic linear and biquadratic exchange.

Neighbor	Distance (\AA)	$\mathcal{J}(ij)$	$K(ij)(\mu\text{eV})$
100	4.165	218.89	-4.8
$\frac{1}{2}\frac{1}{2}\frac{1}{2}$	5.654	10.00	0
110	5.89	-94.45	0
$\frac{1}{2}\frac{3}{2}\frac{1}{2}$	8.165	-1.88	0
200	8.33	-45.67	0
001	9.654	135.6	0

4.7.3 Discussion of Model B

At low temperature the calculation stabilizes a single-q helical magnetic structure with a propagation vector of $(0.222 \ 0 \ 0)$ with moments in the (\mathbf{bc}) plane.

The temperature dependence of the calculated magnetic susceptibility along different directions is in better agreement with the experiment than for the model in section 4.6 (see Fig. 16). There is a peak at T_N for all crystallographic directions, however no second transition at $T_r = 40$ K is reproduced by the calculation.

There is no anisotropy in the Hamiltonian (44) and therefore the calculated magnetization along different directions remains exactly the same (see Fig. 15). Calculations show that application of a *small* field in any direction changes the moment orientation of the helix so that the moments always remain perpendicular to the field, increasing the applied field always results in the same magnetization process by a smooth turning of the magnetic moments from a perpendicular plane towards the applied field direction. Several curves with different magnitude of biquadratic exchange $K(ij)$ are plotted on Figure 15 in order to show that the short range biquadratic exchange strongly affects the saturation field. This deviation from the standard antiferromagnetic behavior (model A, [1]) can be explained: equations (38) and (39) are derived from a small moment expansion of the free energy. Therefore in equation (38) and (39) the higher order biquadratic terms of the interaction have no effect, whereas equation (41) does not hold anymore. The saturation field H_s is very sensitive to small contributions of biquadratic interactions $K(ij)$. Introducing biquadratic interactions removes the main failure of model A, namely the failure to describe consistently the experimental values of the Néel temperature T_N and the saturation H_s .

From several simulations the value of $K(100)$ corresponding to the experimentally measured saturation field $H_s = 9$ T was deduced to be $K(100) = -4.8\mu\text{eV}$. The experiment shows that the critical fields along $[100]$ and $[001]$ are different by a value of approximately 1.5 T. The behavior of the experimentally measured magnetization shows anisotropy which is not reflected in the model.

As seen from Table 9 and 10 the values of exchange tensor $\mathcal{J}_{aa,bb,cc}$ for the nearest neighbor is different from the value used in the previous simulation. Such a change in exchange in $\mathcal{J}_{aa,bb,cc}$ is necessary to keep the value of the Fourier transform $\mathcal{J}(\tau)$ and $\mathcal{J}(0)$ unchanged by the biquadratic term (see Appendix A for details).

4.8 Model C: Combined anisotropic bilinear and biquadratic exchange

4.8.1 Hamiltonian

In order to reproduce the large experimentally observed anisotropy in the system we introduce anisotropic (diagonal) bilinear interactions. Our Hamiltonian (44) should be rewritten in the following form:

$$\mathcal{H} = -\frac{1}{2} \sum_{\alpha} \sum_{i,j}^{i,j} J_i^{\alpha} \mathcal{J}_{\alpha\alpha}(ij) J_j^{\alpha} - \sum_i g_J \mu_B \mathbf{J}_i \mathbf{H} - \frac{1}{2} \sum_{ij} K(ij) (\mathbf{J}_i \mathbf{J}_j)^2 \quad (45)$$

This gives us the opportunity to define each of the diagonal components \mathcal{J}_{aa} , \mathcal{J}_{bb} and \mathcal{J}_{cc} separately. We did not take into account the classical dipolar interaction in this model, because it generates an anisotropy which is in contradiction with the experimental moment direction near T_N^{calc} (compare Model A).

4.8.2 Numerical simulations

In the anisotropic case the Fourier transform of the interaction tensor $\mathcal{J}_{\alpha\beta}$ is given by equation (37).

In such an approach the equations (38), (39) and (41) do not hold anymore and become direction dependent. In order to clarify the situation several simulations with different diagonal anisotropic interaction tensors $\mathcal{J}_{\alpha\beta}$ have been performed. Exchange \mathcal{J}_{aa} and \mathcal{J}_{bb} have been artificially reduced or increased by scaling values with respect to $\mathcal{J}_{cc}(ij)$ by a common factor k (e.g. $\mathcal{J}_{cc} = k\mathcal{J}_{aa,bb}$). For diagonal interaction tensor $\mathcal{J}_{\alpha\beta}(ij)$ equation (38) can be rewritten in the form:

$$T_N = \frac{\mathcal{J}_{\alpha\alpha}(\tau)J(J+1)}{3k_B} \quad (46)$$

where $\mathcal{J}_{\alpha\alpha}(\tau)$ is the highest value of diagonal components of the Fourier transform of anisotropic exchange interaction tensor $\mathcal{J}_{\alpha\beta}(ij)$. Note that in the case of GdRu₂Si₂, $\mathcal{J}_{cc}(\tau)$ should have the highest value, since in the experiment just below the $T_N = 47$ K the moments point in c - direction.

The experimentally determined isotropic nature of the susceptibility above the Néel temperature T_N suggests isotropy of $\mathcal{J}_{\alpha\beta}(Q=0)$. Therefore the equation (39) should still hold.

Some empirical proportionality has been established for the components of the critical field by numerical analysis (see Figures 17, 18):

$$H_{sa} \propto \frac{\mathcal{J}_{aa}(\tau) + \mathcal{J}_{cc}(\tau)}{2} - \mathcal{J}_{aa}(0) \quad (47)$$

$$H_{sc} \propto \frac{\mathcal{J}_{aa}(\tau) + \mathcal{J}_{cc}(\tau)}{2} - \mathcal{J}_{cc}(0) \quad (48)$$

Introduction of greater anisotropies than the classical dipolar interaction makes the phase transition at T_r discussed in section 4.6 more pronounced. The difference

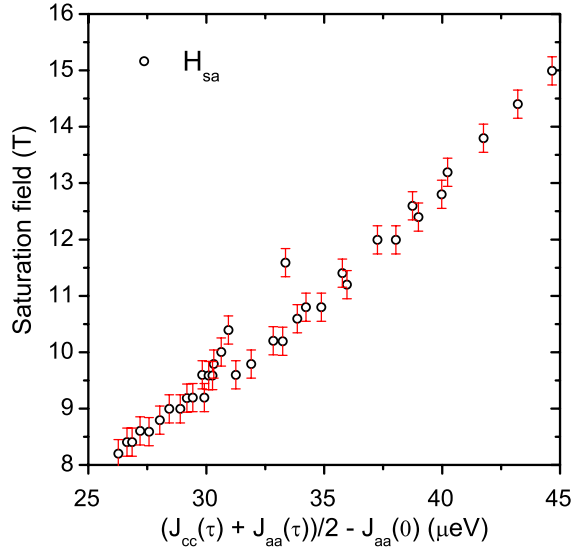


Figure 17: Expression (47) versus calculated saturation field along [100] direction obtained by several different numerical simulation runs. The error bars represent limited accuracy of the numerical simulation.

between Néel temperature T_N and transition temperature T_r is estimated to be (for $K(ij) \approx 0$) see Figure 19):

$$T_N - T_r \propto \mathcal{J}_{aa}(\tau) - \mathcal{J}_{cc}(\tau) \quad (49)$$

Several simulations with different diagonal anisotropic interaction tensors $\mathcal{J}_{\alpha\beta}$ have been performed in order to verify relation (49). Exchange \mathcal{J}_{aa} and \mathcal{J}_{bb} have been artificially reduced or increased by scaling values with respect to $\mathcal{J}_{cc}(ij)$ by a common factor k (e.g. $\mathcal{J}_{cc} = k\mathcal{J}_{aa,bb}$) while $K(ij) \approx 0$. It was found that for $T_N - T_r \approx 7$ K the corresponding value of $\mathcal{J}_{aa}(\tau) - \mathcal{J}_{cc}(\tau) \approx 80\mu eV$.

Further fine tuning of anisotropic exchange involved fulfilling the condition of $\mathcal{J}_{aa,bb}(Q=0) = \mathcal{J}_{cc}(Q=0)$. This was accomplished by changing values of the $\mathcal{J}_{aa,bb}(001)$ so that the $\mathcal{J}_{aa,bb,cc}(0) = 636\mu eV$ as required by equation (39). Doing so and introducing biquadratic exchange obtained in section 4.7 the spin flop transition observed in magnetization data with the field applied along c direction at $H_f^{[001]} = 2.1$ T was also reproduced. For the calculated field induced transition of $H_f^{[001]} = 2.1$ T the correspondent difference in $\mathcal{J}_{aa}(\tau) - \mathcal{J}_{cc}(\tau) \approx 86\mu eV$. A similar value has been obtained above on the basis of the magnitude of the transition temperature $T_r = 40$ K. Therefore it can be concluded, that the metamagnetic transition at T_r and spin flop transition $H_f^{[001]}$ under applied field have the same

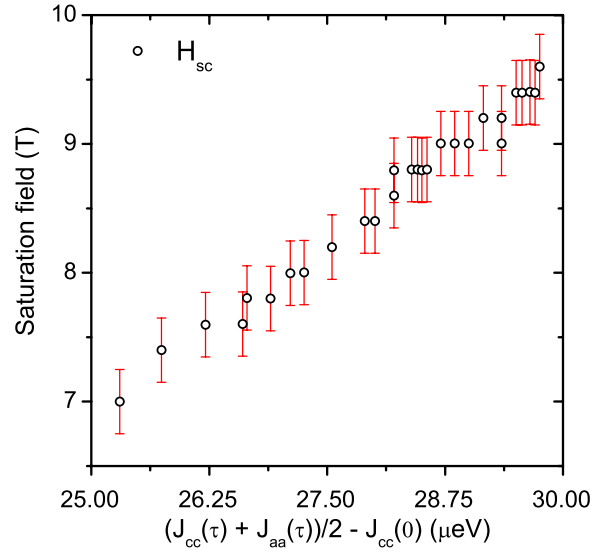


Figure 18: Expression (48) versus calculated saturation field along [001] direction obtained by several different numerical simulation runs. The error bars represent limited accuracy of the numerical simulation.

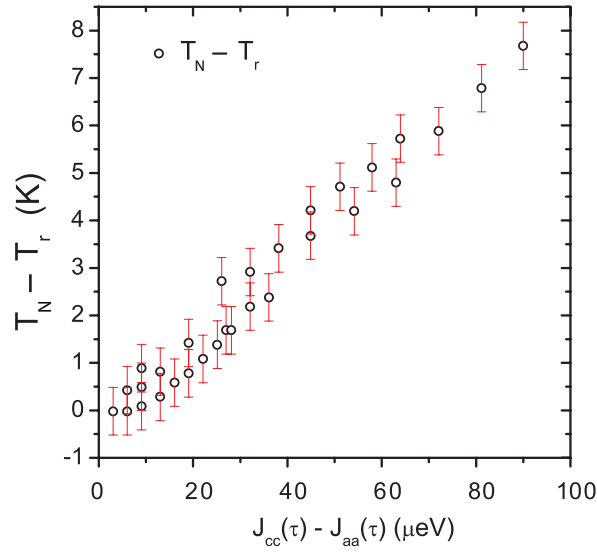


Figure 19: Expression (49) versus calculated transition temperature obtained by several different numerical simulation runs. The error bars represent limited accuracy of the numerical simulation.

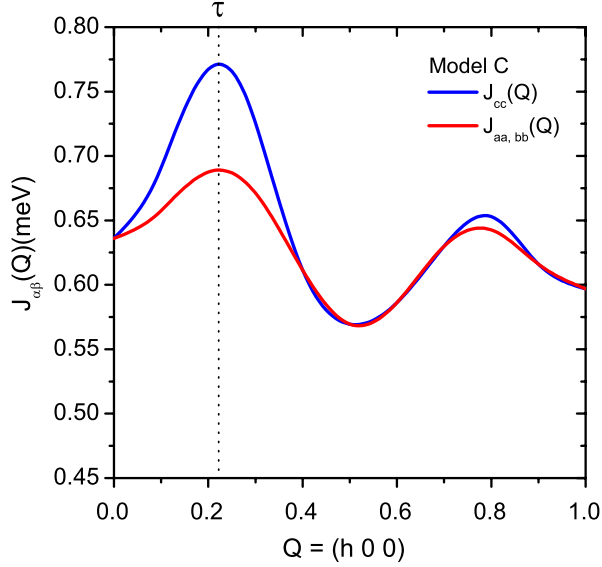


Figure 20: The components of the Fourier transform of the interaction tensor $\mathcal{J}_{\alpha\beta}(ij)$ defined in equation (37). Red line represents $\mathcal{J}_{aa}(Q)$ and $\mathcal{J}_{bb}(Q)$ diagonal components. The blue line represents $\mathcal{J}_{cc}(Q)$ diagonal component.

origin and may be caused by a bilinear anisotropy in the two ion interaction.

A similar value of $J_{aa}(\tau) - \mathcal{J}_{cc}(\tau) \approx 86\mu\text{eV}$ has been obtained during the fine tuning of the difference $J_{aa}(\tau) - \mathcal{J}_{cc}(\tau)$ while calculating the anisotropic magnetization for different sets of $\mathcal{J}_{\alpha\beta}(ij)$.

Further fine-tuning of the difference between $\mathcal{J}_{aa,bb}(\tau)$ and $\mathcal{J}_{cc}(\tau)$ was performed in order to match the exact magnetic field which accompanies the transition (see Fig. 22). The resulting parameters that are shown in Table 11 were used to calculate magnetic properties.

In order to present the resulting model the fine-tuned anisotropy in interaction tensors $\mathcal{J}_{\alpha\beta}(ij)$ and tuned biquadratic exchange parameters $K(ij)$ from model B were used in Hamiltonian (45) (see Table 11).

The Fourier transform of the exchange interaction tensor $\mathcal{J}_{\alpha\beta}(ij)$ is presented in Fig. 20. Fig. 22 shows the calculated magnetization for different magnitudes of the anisotropy plotted versus experimental data. Fig. 23 shows the calculated susceptibility versus the experimentally measured one.

4.8.3 Discussion of Model C

In order to estimate the magnitude of the anisotropy several different simulation runs have been performed without the biquadratic term in the Hamiltonian (45) (e.g. $K(ij) = 0$). It was found that in the anisotropic case the critical fields along different directions are estimated to be proportional to expressions (47) and (48) (see Figures 17, 18).

Subtracting equation (48) from (47) one can express the difference of the saturation fields

$$H_{sa} - H_{sc} \propto \mathcal{J}_{cc}(0) - \mathcal{J}_{aa}(0) \quad (50)$$

Thus giving another discrepancy in the interpretation of the experimental data that needs clarification: the experimentally measured difference $H_{sa} - H_{sc} \approx 1.5$ T. From the proportionality (50) it follows that the difference $\mathcal{J}_{cc}(0) - \mathcal{J}_{aa}(0) \approx 40\mu eV$ ¹⁶. Such a big difference in $\mathcal{J}_{\alpha\alpha}(Q = 0)$ would result in an observable difference in the paramagnetic susceptibilities along a and c (for $T > T_N$). This can be interpreted as following: the susceptibility measured with a magnetic field of 0.1 T will be less affected by a demagnetization factor effect than the magnetization measured for fields up to 10 T. Therefore this inconsistency in the interpretation of the experimental data can be attributed to sample shape specific differences in demagnetization factors along different directions. According to [95] no correction for such a difference had been performed for magnetization data. Therefore it does not make sense to take the experimental values of H_{sa} and H_{sc} to estimate $\mathcal{J}_{cc}(0) - \mathcal{J}_{aa}(0)$ and in this parameterization the relation (50) is ignored.

Another important issue in this system is the existence of a second phase above $T_r^{exp} = 40$ K. Such a phase is predicted to exist just below the ordering temperature when an anisotropy is present in the system.

Using equation (49) and figure 19 one can make a rough estimation of $J_{aa}(\tau) - \mathcal{J}_{cc}(\tau) \approx 80\mu eV$. A similar value has been obtained in the fine tuning of the difference $J_{aa}(\tau) - \mathcal{J}_{cc}(\tau)$ by calculating the anisotropic magnetization for different sets of $\mathcal{J}_{\alpha\beta}(ij)$ (see section 4.8.2 for discussion).

At low temperatures the resulting calculation stabilizes a single q helical magnetic structure with propagation vector of $(2/9 \ 0 \ 0)$. The propagation vector is temperature independent. The calculated magnetic structure is temperature dependent and undergoes a transition at $T_r = 40$ K. The magnetic structure at low temperature is helical with moments in the **(bc)** plane. The transition at $T_r = 40$ K is attributed to the suppression of the *b* component in the helix leading to a collinear amplitude modulated structure with moments in *c* direction for

¹⁶Please note, that even though the equation (50) has been extensively validated for the systems with different anisotropy and no biquadratic exchange present, calculations with $K(ij) \neq 0$ also shows that the equation (50) still holds.

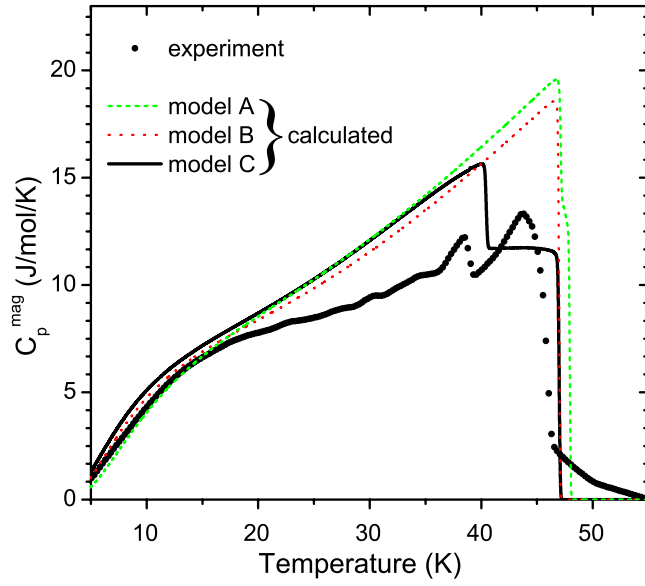


Figure 21: Temperature dependence of magnetic contribution to the specific heat. The data (black circles) was obtained by subtracting the specific heat of LaRu_2Si_2 (non magnetic analog) from the one of GdRu_2Si_2 (e. g. $C_m = C_{\text{GdRu}_2\text{Si}_2} - C_{\text{LaRu}_2\text{Si}_2}$). Dashed green, red short dashed and solid black lines represent the calculated magnetic contribution to the specific heat for the models A, B and C respectively.

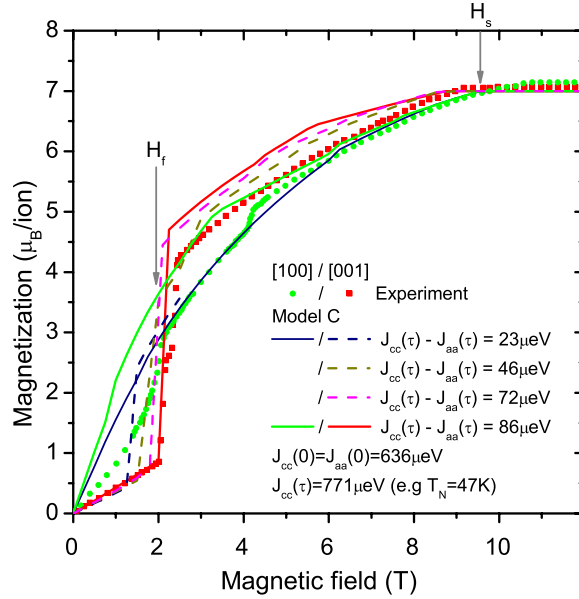


Figure 22: Magnetization along different crystallographic directions. The dots represent measured curves [95] while the lines represent calculated magnetization for the system with Hamiltonian (45). Exchange interaction tensor $\mathcal{J}_{\alpha\beta}(ij)$ has been varied so that the difference $J(\tau)_{aa,bb} - J(\tau)_{cc}$ takes different values (see legend) and $J(0)_{aa,bb} - J(0)_{cc} = 0$. Isotropic short range biquadratic exchange for nearest neighbor 100 has been taken from Table 11.

$T_r < T < T_N$. Such an amplitude modulated structure is indicated by a jump of $\Delta C_P = 13.43$ J/K mol in the magnetic contribution to the specific heat at the Néel temperature [9, 7] (See Fig. 21). In contrast to models A and B the model C reproduces these features of the experimental specific heat. Moreover, in model C at all temperatures below the Néel temperature $T_N = 47$ K the calculated magnetic structure corresponds to the experimental result.

The calculated magnetization along [001] reproduces the first order transition at $H_f^{[001]} \approx 2.1$ T very well. However, the calculated magnetization along [100] does not correspond to the experimentally measured one. The slope of magnetization near the zero field is abnormally high in comparison to the experiment. This result can also be observed in the calculation of magnetic susceptibility presented in Figure 23. The anomalous anisotropy in the system is reflected in a difference for susceptibilities along different directions. The direction [001] moderately corresponds to the experiment while [100] is considerably larger than the experimental data. The susceptibility along a and b as expected from the model is identical and

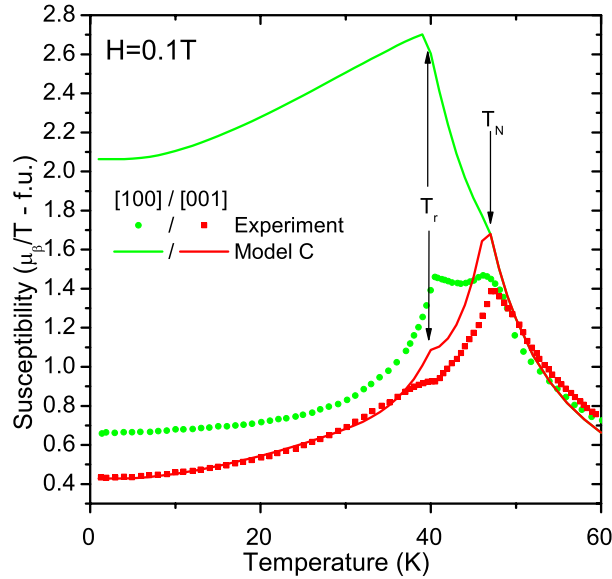


Figure 23: Magnetic susceptibility along main crystallographic directions. The dots represent measured curves [95]. The solid lines represent the calculated susceptibility along different crystallographic directions for the system with Hamiltonian (45) where the exchange interaction tensors $\mathcal{J}_{\alpha\beta}(ij)$ and $K(ij)$ were taken from Table 11.

therefore the domain effect can not be considered as a potential explanation for such a behavior. In order to remove the discrepancies in the magnetization and susceptibility it will probably be necessary to introduce an in-plane anisotropy.

4.9 Conclusions

The lack of crystal field effects in Gd^{3+} compounds reveals the complexity of magnetic interactions. GdRu_2Si_2 shows unique magnetic properties such as anisotropy and unusual susceptibility behavior.

The magnetic structure is very well supported by different experiments and numerical simulations confirm a helical structure of propagation vector $(0.222\ 0\ 0)$ with moments perpendicular to it. Three major numerical simulation attempts have been carried out in order to interpret the magnetic properties (see Fig. 24).

Model A is a standard model for Gd^{3+} [1] systems and includes the classical dipolar interactions and isotropic spin-spin exchange.

- The temperature dependent calculation from 0 up to 40K predicts the correct magnetic structure.

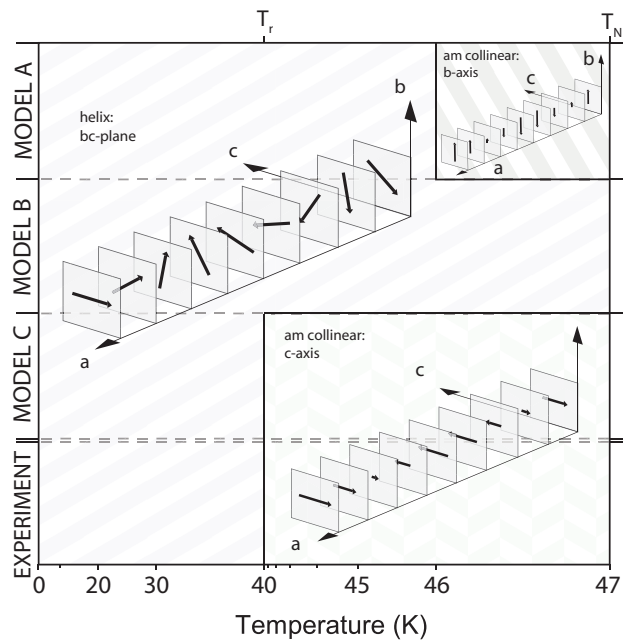


Figure 24: The following sketch represents the temperature dependence of calculated magnetic structures of GdRu_2Si_2 for different models in zero field. Note that a non-linear temperature scale is used for illustration of various magnetic structures near T_N .

Table 11: Anisotropic linear and isotropic biquadratic exchange.

Neighbor	Distance (Å)	$\mathcal{J}_{aa,bb}(ij)$	$\mathcal{J}_{cc}(ij)$	$K(ij)(\mu\text{eV})$
100	4.165	83.9	218.89	-4.8
$\frac{1}{2}\frac{1}{2}\frac{1}{2}$	5.654	3.8	10.00	0
110	5.89	-36.3	-94.45	0
$\frac{1}{2}\frac{3}{2}\frac{1}{2}$	8.165	-0.72	-1.88	0
200	8.33	-17.54	-45.67	0
001	9.654	248.5	135.6	0

- The magnetic phase observed just below the ordering temperature (46 - 47 K), suggest an amplitude modulated structure with moment parallel to b in contrast to the experiment, which suggests a collinear amplitude modulated structure with moments parallel to c direction in the temperature range 40 - 47 K.
- The temperature dependence of the magnetic susceptibility of the system is different from the experimentally observed one.
- The calculations with applied magnetic field show significant disagreement with the experimental data (wrong saturation field value, no transitions).

Model B is an isotropic model with biquadratic interaction:

- The temperature dependent calculation from 0 up to 40K predicts the correct magnetic structure.
- No temperature induced transition at T_r is produced by the calculation.
- Biquadratic exchange clearly improves the description of the magnetization (correct saturation fields, but no transitions).
- The susceptibility behavior shows a pronounced decrease with temperature which is also observed experimentally.

Model C combines biquadratic interaction from the model B and two ion anisotropy.

- The temperature dependent calculations from 0 up to 47 K predict the correct magnetic structure.
- The temperature induced transition at T_r is reproduced by the calculation.

- The calculated susceptibility along the c direction agrees with the experiment, whereas along a the calculation significantly exceeds the experiment.
- The calculated magnetization successfully reproduces the first order transition along the c direction at $H_f^{[001]} = 2.1$ T. However, the calculated magnetization along a direction does not reproduce two transitions $H_{f1}^{[100]}$ and $H_{f2}^{[100]}$ observed in experiment.

The unusual magnetic properties exhibited by this system cannot be explained within the framework of the standard model [8]. The classical dipolar interaction can not be the reason of anisotropic behavior. Some selective correspondence to experimentally observed behavior have been obtained by introducing isotropic biquadratic and anisotropic bilinear interactions. Further modeling of the biquadratic interactions and bilinear anisotropy is needed to improve the description of the experimental data.

5 GdCu₆

5.1 Introduction

GdCu₆ is an orthorhombic system with spacegroup $Pnma$. Thermal variations of susceptibility along different directions in the paramagnetic state show small anisotropy. Paramagnetic Curie temperatures have been determined to be -32.1 K, -30 K and -2.61 K along the a -, b - and c -axes, respectively. The susceptibility and magnetization at low temperature indicate an antiferromagnetic order below the Néel temperature $T_N = 16$ K [104]. The temperature dependence of the specific heat shows an additional transition at $T_r = 15.8$ K. The estimated effective magnetic moment per Gd³⁺ ion is $\approx 7.8\mu_B$ [105]. The saturation field $H_s \approx 24$ T was deduced from magnetization in pulsed high magnetic field [105].

5.2 Sample preparation

The polycrystalline GdCu₆ sample was prepared at IFW, Dresden by levitation melting technique from pure Gadolinium with a purity of 99.9% and copper with a purity of 99.999%. A Hukin type cold crucible with argon atmosphere was used for this alloying. To ensure homogeneity of the reacted components the resulting droplets were annealed at $T = 800^\circ\text{C}$ for 72 hours. The crystallinity of the resulting sample has been verified by x-ray powder diffraction.

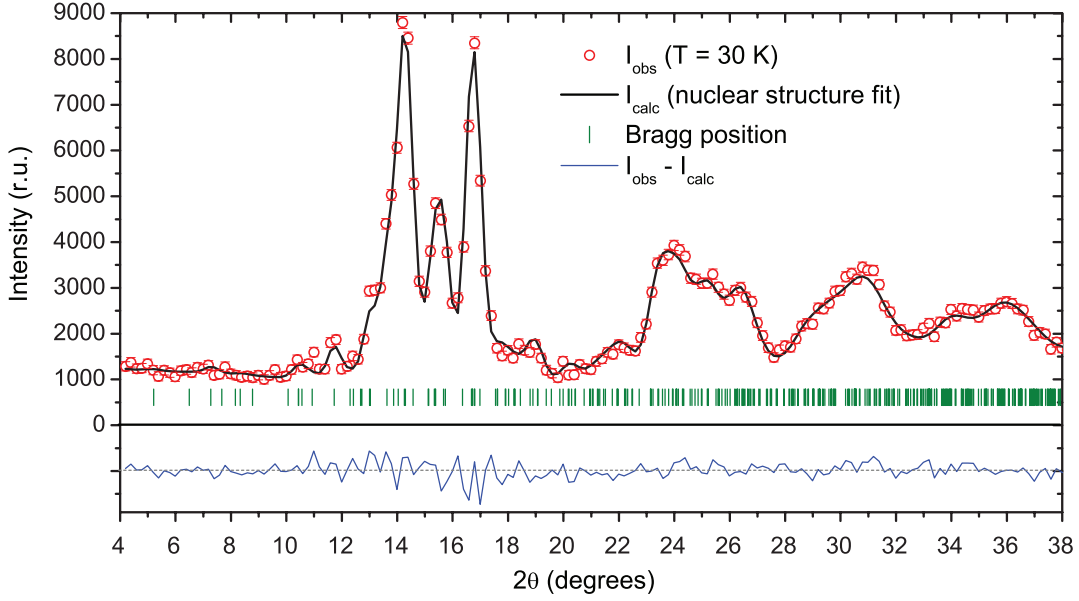


Figure 25: GdCu_6 hot neutron diffraction pattern measured at 7C2, Saclay. The red open circles represent the experimental data measured above the ordering temperature. The line represents the Rietveld refinement of the nuclear structure.

5.3 Neutron diffraction

Due to the high neutron absorption cross section of natural Gd for thermal neutrons the magnetic structure was studied using hot neutrons. The powder diffraction patterns were collected at the 7C2 instrument at LLB, Saclay. A neutron wavelength of 0.57 \AA was selected by a Ge (311) monochromator.

The resulting amount of powder measured was about 8 g. In order to reduce absorption the powder was placed in a vanadium annular sample holder. Two diffraction patterns were collected at temperatures of 2 K and 30 K with a counting time of 9 hours. An empirical background I_{bkg} was estimated from the neutron diffraction pattern of a fully absorbing (cadmium foil) sample I_{cd} and an empty sample holder I_{empty} using the following formula: $I_{bkg} = I_{cd} + k(I_{empty} - I_{cd})$ where $k = 0.3807$.

Because of the resonance effects in natural Gd the neutron scattering cross section is wavelength dependent. For the neutron energies of about 0.25 eV the effective coherent cross section of 10.2 fm (with real part of 9.99 fm and -0.82 fm as imaginary part) was used [90]. The FullProf package was used to analyze the diffraction pattern.

The nuclear structure was fitted to the 30 K powder pattern. Results of the Rietveld refinement are summarized in Table 12 and presented in Figure 25. The

unit cell dimensions were determined to be $a=8.023 \text{ \AA}$, $b=5.027 \text{ \AA}$, $c=10.075 \text{ \AA}$.

Table 12: Results of refinement of atomic positions with Rietveld refinement.

Atom	Wyckoff index	x	y	z	Temperature factor (\AA^2)
Gd	4c	0.257(8)	0.25	0.566(5)	0.1(1)
Cu1	8d	0.05(1)	0.477(8)	0.313(4)	0.2(2)
Cu2	4c	0.06(1)	0.25	0.077(7)	0.3(2)
Cu3	4c	0.142(8)	0.25	0.853(9)	0.3(2)
Cu4	4c	0.292(9)	0.25	0.272(8)	0.3(2)
Cu5	4c	0.375(9)	0.25	0.005(9)	0.3(2)

Neutron diffraction data at low temperature clearly indicates the presence of a long period possibly incommensurate structure. A scripting interface was written for the FullProf package in order to resolve the magnetic structure. Different antiferromagnetic configurations were sequentially introduced to the FullProf program to calculate the diffraction pattern. The simulated configurations are all of those commonly observed in rare-earth antiferromagnets and include collinear structures, amplitude modulated structures as well as a set of cycloids with moments aligned along different directions. Given the experimental resolution different antiferromagnetic configurations within $10 \times 10 \times 10$ crystallographic unit cells were sequentially introduced to the FullProf program to calculate the diffraction pattern. The results of the low temperature neutron powder diffraction fit are presented in Figure 26.

The magnetic propagation vector $\tau = (2/9 \ 0 \ 0) \approx (0.22 \ 0 \ 0)$ has been determined from the diffraction pattern (Figure 26). Several different antiferromagnetic configurations with this propagation vector have been calculated in order to match the magnetic intensity. The magnetic moments restricted to the bc - plane reproduce the measured scattering intensity. Within the experimental resolution assuming an equal moment collinear structure in the bc - plane the moment direction along the $[021]$ direction e. g. $\approx 45^\circ$ between b and c was refined. Such a magnetic configuration gives the same scattering intensities as a helical structure with equal moments.

5.4 Numerical simulation

As explained in the introductory chapter the classical Gd^{3+} system can be treated with Hamiltonian (40).

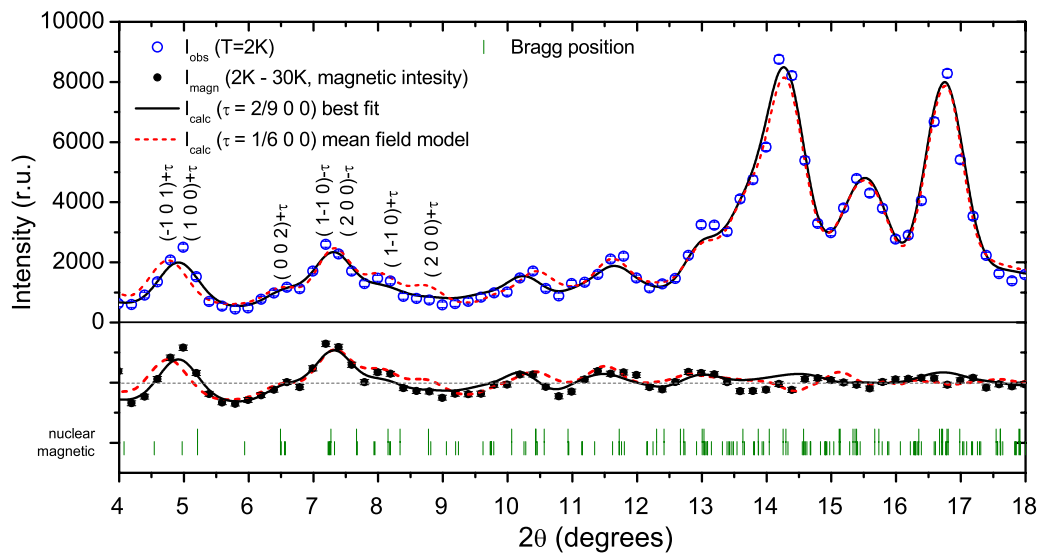


Figure 26: GdCu_6 hot neutron diffraction data obtained at 7C2, Saclay. Blue open circles represent experimental data measured below the ordering temperature. The line represents the fit of magnetic and nuclear structures. Black dots below represent the difference between the high and low temperature diffraction pattern.

Due to the small magnitude of the classical dipolar interaction $D_{ij}^{\alpha\beta} J_i^\alpha J_j^\beta$ the antiferromagnetic propagation vector is dominated by the spin - spin exchange $\mathcal{J}_{\alpha\beta}(ij) = \mathcal{J}(ij)\delta_{\alpha\beta}$, where $\delta_{\alpha\beta}$ denotes the Kronecker symbol.

In order to minimize the free energy the Fourier transform (37) will have a maximum at the propagation vector of the antiferromagnetic structure [1]. The magnitude of this maximum can be related to the Néel temperature $T_N = 16$ K (assuming isotropic exchange) using equation (38)

According to [105] GdCu₆ shows the Curie-Weiss behavior in paramagnetic state. The inverse susceptibility can be fitted yielding the paramagnetic Curie temperatures $\theta_{\alpha=a,b,c}$ (in this case $\theta_a = -32.1$ K, $\theta_b = -30$ K and $\theta_c = -2.61$ K) along different crystallographic directions. The fact that $\theta_a \approx \theta_b \neq \theta_c$ indicates some significant anisotropy in the two ion interaction $\mathcal{J}_{\alpha\alpha}(ij)$. The Curie temperatures are related by the mean field theory to the magnitude of the Fourier transformation of the exchange at $Q = 0$ i.e. $\mathcal{J}_{\alpha\alpha}(Q = 0)$ via (39)

Using equations (38) and (39) one can estimate the magnitude of $\mathcal{J}(Q = \tau) \approx 262\mu\text{eV}$, $\mathcal{J}_{aa}(Q = 0) \approx -527\mu\text{eV}$, $\mathcal{J}_{bb}(Q = 0) \approx -509\mu\text{eV}$ and $\mathcal{J}_{cc}(Q = 0) \approx -48\mu\text{eV}$. For a periodic antiferromagnetic structure the critical (saturation) field along different directions is estimated by (41) [1].s

Using equations (39) and (38) in (41) the expression for the critical field value can be obtained

$$H_s^\alpha = \frac{3k_B(T_N - \theta_\alpha)}{gJ\mu_B} \quad (51)$$

Using the experimentally obtained values of T_N and θ_α in (51) the saturation field along the c direction $H_{sc}^{calc} \approx 9.2$ T is calculated. As seen from the experiment this value does not correspond to the experimentally measured saturation field $H_{sc}^{exp} \approx 24$ T. However the calculated saturation fields along a and b show more reasonable values $H_{sa}^{calc} \approx 23.82$ T and $H_{sb}^{calc} \approx 23.28$ T.

Since the primitive crystallographic cell of GdCu₆ contains more than one Gd atom the above evaluation is not straight forward. The method described in [106, 9] can not be applied directly since expression (37) is valid strictly for single atom basis. In the case of multiple atoms (n_b) in the primitive unit cell $\mathcal{J}_{\alpha\beta}^{r,r'}(Q)$ in expression (37) has to be expressed as a tensor, the indices $r, r' = (1..n_b)$ are necessary to express the exchange between different atoms r and r' in the primitive unit cell. The diagonalization of this tensor will be required to obtain the Néel temperature for such a system. Although equations (37), (39), (38), (41) have to be modified accordingly, the resulting expression (51) will remain valid.

In order to simulate the magnetic properties of GdCu₆, in a first step the anisotropy seen in the paramagnetic Curie temperature was neglected. Direct exchange effects can probably be neglected in comparison to the RKKY interaction due to the metallic character of this system and the large Gd-Gd distances -

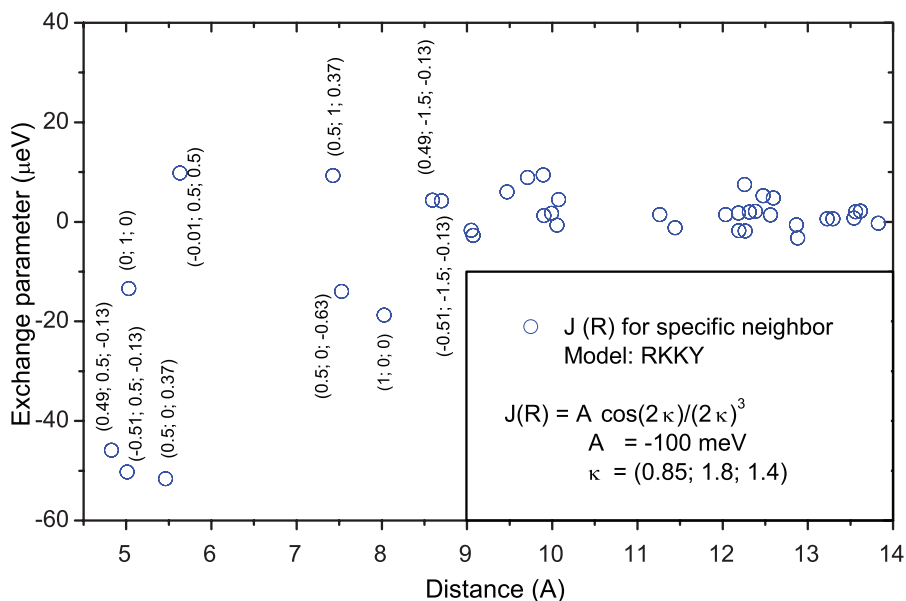


Figure 27: Exchange parameters calculated by equation (52) for GdCu₆. Dots represent the exchange constants $\mathcal{J}(R)$ where R is the distance to equivalent neighbors.

the nearest neighbor distance 0.48 nm is large compared to the atomic radius of Gd (0.18 nm). Therefore the spin-spin exchange was chosen to be isotropic and assumed to be oscillating according to the RKKY model [1], generalized to an anisotropic Fermi-surface:

$$\mathcal{J}(r) = A \cos(2\kappa) / (2\kappa)^3 \quad (52)$$

with

$$\kappa^2 = k_a^2 r_a^2 + k_b^2 r_b^2 + k_c^2 r_c^2 \quad (53)$$

The calculation which is in detail described in section 3.2 was performed for different values of the Fermi surface tensor $k_F = (k_a, k_b, k_c)$ and best correspondence to the experimental propagation vector and other magnetic properties was found for $k_F = (0.85, 1.8125, 1.4) \text{ \AA}^{-1}$. In order to get the correct magnitude of the Néel temperature the scaling factor A was set to $A = -100 \text{ meV}$. The parameters are shown in fig 27. In this parameter set the $T_N^{\text{calc}} = 17,4 \text{ K}$. The isotropic paramagnetic Curie temperature $\theta_\alpha = -9 \text{ K}$ is in between the experimental values $\theta_a = -32.1 \text{ K}$ and $\theta_c = -2.61 \text{ K}$. Applying equation (41) the calculated saturation field $H_S^{\text{calc}} \approx 14 \text{ T}$.

In addition to the RKKY interaction $\mathcal{J}(R)$ as parametrized by equation (52) the dipolar interaction (36) was used.

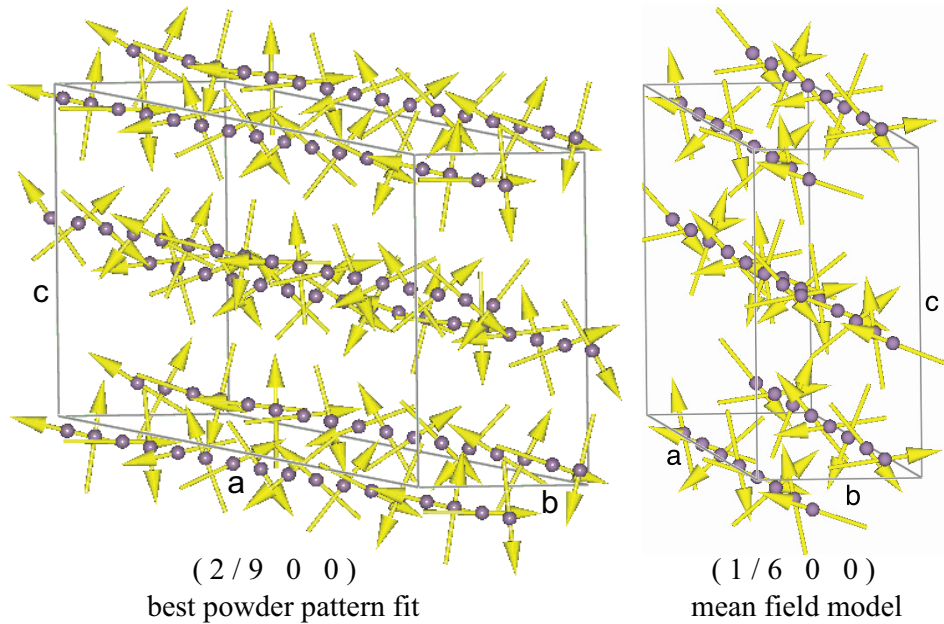


Figure 28: a) (left) Magnetic structure of GdCu_6 at $T = 2$ K, fit from neutron powder diffraction. b) (right) Calculated magnetic structure of GdCu_6 at $T = 2$ K using the mean field model discussed in the text. Only Gadolinium atoms are shown.

5.5 Discussion

Treating these interactions in the form of the Hamiltonian (40) a helical magnetic structure was obtained at 2 K with propagation vector $\tau = (0.167\ 0\ 0)$ and moments in the (bc) plane. Note that the structure is a helix with a turning angle of 60 degrees. Taking into account the considerable experimental error involved in a short wavelength experiment this is in good accordance with the experimental data. The calculated magnetic structure is shown in Figure 28b.

The diffraction pattern was calculated for this helix and is compared to the experimentally observed pattern in Figure 26. Within the experimental resolution the overall agreement is reasonable.

In addition to the magnetic structure at 2 K the temperature dependence of the magnetic susceptibility was calculated and is shown in comparison to experimental data in Figure 29. As reported by low temperature susceptibility measurements the antiferromagnetic hard axis is parallel to the $[100]$ direction, suggesting that the bc - is the easy plane. As suggested by the neutron diffraction experiment and numerical simulations, the magnetic moments are situated in the (bc) plane, thus fully corresponding to an expectation from bulk measurements.

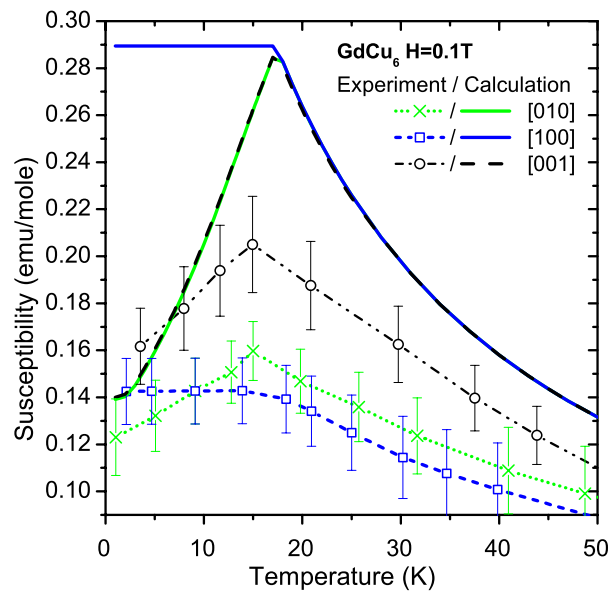


Figure 29: Temperature dependence of magnetic susceptibility along three main crystallographic directions in the low temperature region. Data (dashed lines) was taken from [105]. Calculated magnetic susceptibility is represented by solid lines.

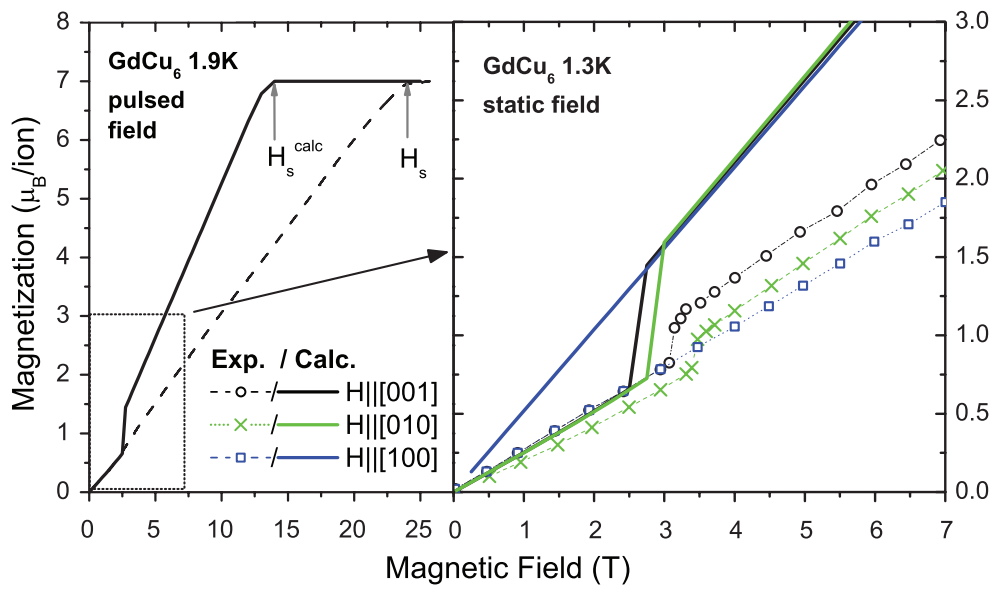


Figure 30: Experimentally measured magnetization of GdCu_6 in static and pulsed magnetic field. The magnetic field pulse was applied along the $[001]$ direction. A static magnetic field up to 14 T was used to obtain magnetization for main crystallographic directions. Data taken from $[105]$ (dashed lines) is confronted with results of a numerical simulation (bold lines) described in section 5.

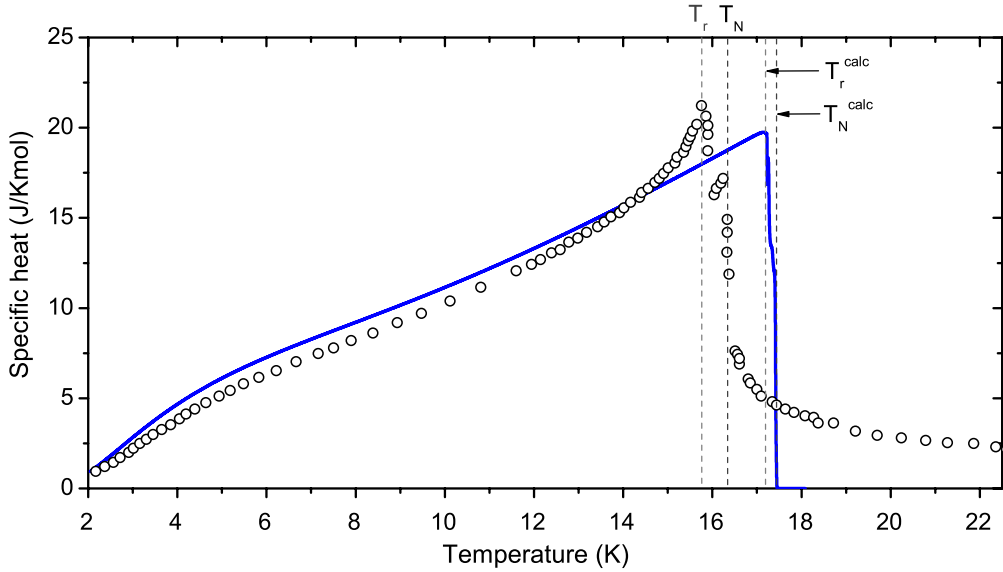


Figure 31: Temperature dependence of magnetic contribution to the specific heat. The data (black open circles) was obtained by subtracting the specific heat of LaCu_6 (non magnetic analog) from the one of GdCu_6 (e. g. $C_m = C_{\text{GdCu}_6} - C_{\text{LaCu}_6}$). Data taken from [105]. The solid blue line represents the calculated magnetic contribution to the specific heat by mean field approximation described in section 3.2.

The magnetic contribution to the specific heat can be compared to experimental data in Figure 31. From the experimental data and the simulation it can be seen that another antiferromagnetic phase is stabilized in the vicinity of the Néel temperature. According to the calculation in this phase the propagation vector stays the same like at lower temperatures $(0.167 \ 0 \ 0)$. However, the moments are aligned in an amplitude modulated collinear structure parallel to the b -direction. Like in many other Gd compounds such a collinear phase in a narrow temperature range below the Néel temperature may be stabilized by the dipolar anisotropy [8].

The magnetization for the magnetic field along the main crystallographic directions has been calculated and is confronted to experimental data in Figure (30). All main features of magnetization are reproduced but the calculated saturation field $H_s^{\text{calc}} \approx 14$ T while the experiment suggests $H_s^{\text{exp}} \approx 24$ T. Such a difference however is attributed to the particular values of $\mathcal{J}(r)$ which were fitted to obey $\theta = -9$ K leading to a too small value of $H_{s\alpha}^c$ via relation (41).

5.6 Conclusion

Since GdCu_6 has more than one Gd^{3+} ion in the unit cell, the procedure of obtaining the values of $\mathcal{J}(r)$ involves fine tuning a large number of exchange parameters for different symmetrically equivalent neighbors in order to match the maximum condition of equation (37) (generalized to more atoms per unit cell) at $Q = \tau$ where τ is the experimentally determined propagation vector. To express an exchange within four Gd^{3+} ions in the primitive unit cell twelve independent exchange constants are required. To obtain a long range antiferromagnetic order even more parameters have to be considered. In order to reduce the number of fit parameters a more general formalism of an RKKY exchange (52) is used. Within the particular choice of four parameters in equation (52) the exchange between any neighboring atoms can be analytically expressed. To obtain a stable antiferromagnetic configuration the energy of the Hamiltonian (40) has been iteratively minimized. Such formulation of exchange interaction does not allow introduction of anisotropy in the paramagnetic region, which is observed in the experimental susceptibility above the Néel temperature. Such anisotropy is expected to lead to a larger difference between T_N and T_r . It can also affect the slope of the magnetization curves along different directions but no other features are expected.

Most of the experimentally observed magnetic features have been reproduced by calculations. The susceptibility is constant for the hard axis direction below T_N . The magnetization is almost linear up to the saturation. Such a behavior is expected from the standard model described in section 4.6. Thus GdCu_6 can be considered as well described by the standard model of rare earth magnetism. The magnetic structure observed using neutron scattering is in agreement with expectations from the dipolar model [8]. No direct evidence for biquadratic interactions described in the previous chapter have been observed for GdCu_6 . However, by comparing the results of this model analysis with the published single crystal bulk magnetisation and susceptibility data it can be stated that some source of anisotropy other than the dipolar interaction must be present in GdCu_6 . Additional studies should involve a high resolution magnetic x-ray or neutron diffraction experiment on single crystals.

6 Other Gd compounds

The GdRu_2Si_2 and GdCu_6 were presented in details above as a good examples of different theoretical approaches being applied in order to interpret the magnetic phenomena in Gd^{3+} systems. The relatively simple crystallographically GdRu_2Si_2 exhibits magnetic properties which are very unusual for this class of compounds whereas GdCu_6 - rather complicated crystallographic system shows

very predictable magnetic properties according to the theory. In addition to these two widely presented cases other Gd compounds studied in this thesis work will be shortly reviewed.

6.1 GdRu₂Ge₂

GdRu₂Ge₂ crystallizes in ThCr₂Si₂ - type tetragonal structure (space group I4/mmm). It orders antiferromagnetically below the ordering temperature $T_N = 33$ K. The specific heat step like behavior indicates a rather long-period amplitude modulated incommensurate magnetic structure [95].

The polycrystalline GdRu₂Ge₂ sample was prepared by an arc-melting technique from natural Gadolinium with 4N purity. Stoichiometric GdRu₂Ge₂ was repeatedly arc-melted on water cooled copper cubicle under Zr gettered Ar atmosphere (IFW, Dresden). To ensure a better homogeneity the sample was annealed at 900 ° for 48 hours. The resulting crystallinity of the sample has been verified using x-ray diffraction.

Due to the high neutron absorption cross-section of natural Gd for thermal neutrons the magnetic structure was studied using hot neutrons. The powder diffraction patterns were collected at the 7C2 instrument in LLB, Saclay. A neutron wavelength of 0.57 Å was selected by a Ge (311) monochromator. In order to reduce absorption the powder was placed in a vanadium annular sample holder. Two diffraction patterns were collected at temperatures of 2.3 K and 45 K with a counting time of 9 hours. An empirical background was estimated from the neutron diffraction pattern of a fully absorbing (cadmium foil) sample and an empty sample holder using the following formula: $I_{bkg} = I_{cd} + k(I_{empty} - I_{cd})$ where $k = 0.1936$.

Because of the resonance effects in natural Gd the neutron scattering effective coherent cross section of 10.2 fm (with real part of 9.99 fm and -0.82 fm as imaginary part) was used [90]. The analysis of the diffraction pattern was carried out with the FullProf package.

The nuclear structure was fitted to the 45 K powder pattern. Results of the Rietveld refinement are summarized in Table 12 and presented in Figure 32. Unit cell dimensions were determined to be $a = c = 4.06(4)$ Å, $c = 9.65(3)$ Å.

Neutron diffraction data at low temperature clearly indicates the presence of a long period possibly incommensurate structure (see Figure 33). Different antiferromagnetic configurations were subsequently introduced to the FullProf program to calculate the diffraction pattern. Given the experimental resolution different antiferromagnetic configurations within 10 x 10 x 10 crystallographic unit cells were sequentially introduced to the FullProf program to calculate the diffraction pattern.

The best fit within this limited search of magnetic structures has the propagation vector $\tau = (2/5 \ 5/6 \ 1/2) \approx (0.4 \ 0.833 \ 0.5)$. The magnetic structure appears

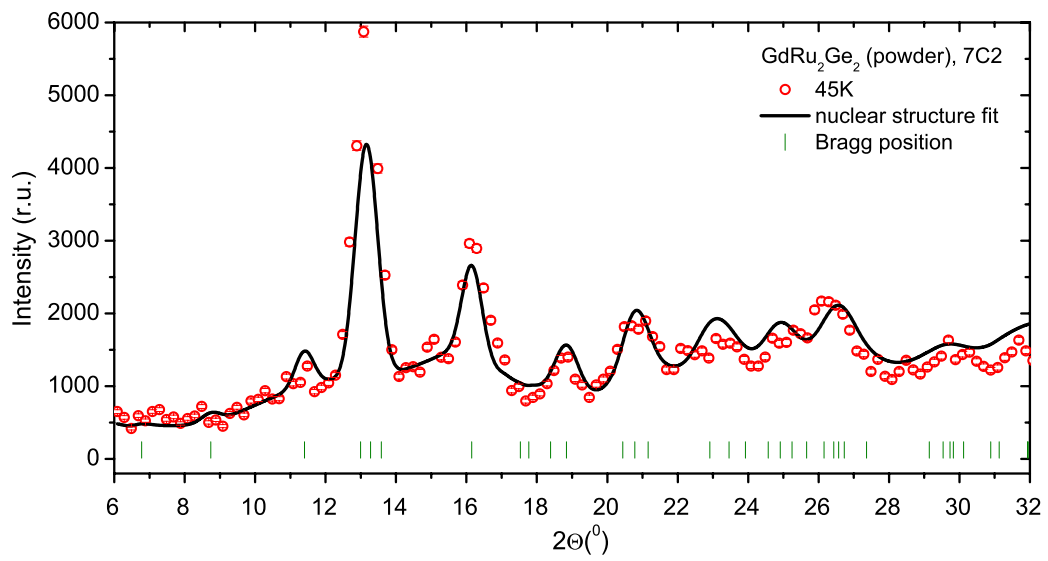


Figure 32: GdRu_2Ge_2 hot neutron diffraction data obtained at 7C2, Saclay. The red open circles correspond to the experimental data measured above the ordering temperature. The solid line represents the calculated intensity for the nuclear structure summarized in Table 13.

Table 13: Results of refinement of atomic positions of GdRu₂Ge₂ with Rietveld refinement.

Atom	Wyckoff index	x	y	z	Temperature factor (Å ²)
Gd	2a	0.0	0.0	0.0	0.2(4)
Ru	4d	0.0	0.5	0.25	0.4(2)
Ge	4e	0.0	0.0	0.370(9)	0.1(5)

to be a spin density wave with moments parallel to the projection of propagation vector τ on (**ab**) - plane.

The results of the low temperature neutron powder diffraction fit are presented in Figure 33. The proposed structure is in agreement with the structure indicated by bulk measurements in [95]. However due to the low resolution of a hot neutron powder experiment further investigation of this propagation vector would require a single crystal experiment.

6.2 GdPt₃Si

GdPt₃Si is a non-centrosymmetric CePt₃B type tetragonal system [107]. Specific heat measurements indicate that it is an amplitude modulated antiferromagnet below $T_N = 15.1$ K. This is the first non centrosymmetric tetragonal Gd compound which has been studied.

The polycrystalline GdPt₃Si sample was prepared by an arc melting technique on a water cooled copper hearth in argon atmosphere. The high purity starting materials used were Gd and Pt ingots - 4N and Si pieces - 6N. The arc melted buttons were vacuum sealed within thick walled quartz tubes, heat treated at 800°C for 10 days and then quenched in water.

The powder diffraction patterns were collected at the D4 instrument in ILL, Grenoble. A neutron wavelength of 0.49 Å was selected by a Cu(220) monochromator. In order to reduce absorption the powder was placed in a vanadium annular sample holder. Multiple diffraction pattern were collected in the temperature range of 4K and 30K with a counting time of 30 minutes. An empirical background (I_{bkg}) was estimated from the neutron diffraction pattern of a fully absorbing (isotopic Boron - I_B) sample and an empty sample holder (I_{empty}) using the following formula:

$$I_{bkg} = I_B + k(I_{empty} - I_B) \quad (54)$$

where $k = 0.126$ is an empirically estimated constant.

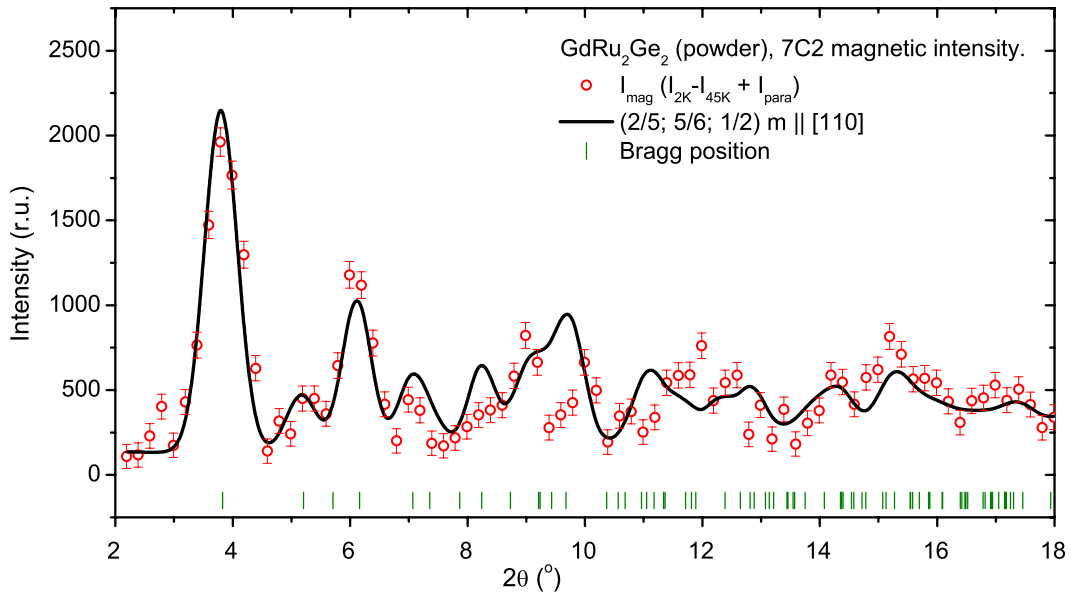


Figure 33: GdRu₂Ge₂ hot neutron magnetic only scattering profile. Red open circles represent the magnetic only scattering intensity. Paramagnetic scattering has been accounted for by subtracting the high and low temperature spectra. The solid black line represents the calculated intensities for a magnetic configuration with propagation vector $\tau = (2/5 \ 5/6 \ 1/2)$.

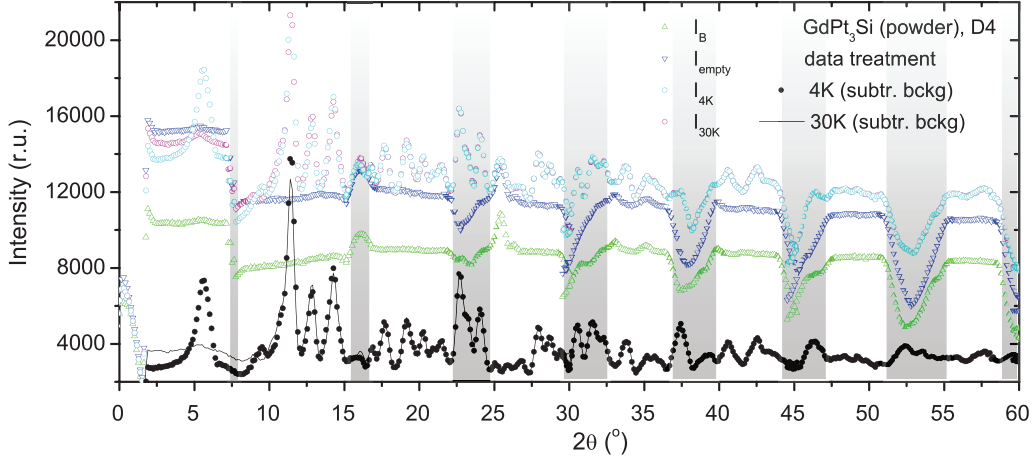


Figure 34: Hot neutron diffraction data obtained at D4, ILL. Pink and blue open circles represent raw neutron diffraction data measured on GdPt_3Si above and below the ordering temperature respectively. The hollow triangles pointing downwards and upwards are representing the diffraction pattern of empty and fully absorbing samples respectively. The black line and black filled circles represent the diffraction pattern above and below the ordering temperature respectively with subtracted background according to the procedure described in the text. Gray areas mark the certain sectors where due to the specific experimental conditions the intensities can not be reliably extracted.

As seen from the Figure 34 the background subtraction for such highly absorbing sample is not a trivial procedure. Since D4 is equipped with a wide angle multidetector the resulting raw pattern is a combination of contributions of multiple detector reading normalized by a certain detector efficiency profile. The linear part of the detector efficiency can be observed in the Figure 34 as a plateau like feature in the diffraction patterns (especially visible in fully absorbing and empty sample patterns). The gray areas mark out the regions where the difference between the I_{empty} and I_B is changing, therefore making the evaluated background dependent on the particular choice of the k coefficient in equation 54. Such a difference in I_{empty} and I_B makes the subtraction difficult and the nuclear and magnetic scattering intensities in these regions can not be trusted as they may be altered by the non-linearity in the I_{bkg} .

Because of the resonance effects in natural Gd the neutron scattering cross section is wavelength dependent. For the neutron energies of about 0.25 eV the effective coherent cross section of 10.2 fm (with real part of 9.99 fm and -0.82 fm as imaginary part) was used [90].

The resulting pattern with subtracted background (black circles in Fig. 34)

Table 14: Results of refinement of atomic positions of GdPt₃Si with Rietveld refinement.

Atom	Wyckoff index	X	Y (cell units)	Z	Temperature factor (Å ²)
Gd	1a	0.0	0.0	0.0	0.56(4)
Pt1	2c	0.5	0.0	0.454(6)	0.46(2)
Pt2	1b	0.5	0.5	0.241(9)	0.46(2)
Si	1b	0.5	0.5	0.835(8)	0.25(6)

was analyzed with the FullProf package.

Nuclear structure was fitted at 30 K temperature diffraction pattern (See Figure 35). No asymmetry in the peak shape have been considered. For corresponding instrument, wavelength and sample size 9.3805, 1.9033 and 0.2029 were used as U, V and W parameters in the refinement. Results of the Rietveld refinement are summarized in the Table 14. Unit cell dimensions were determined to be $a = b = 4.027(9)$ Å, $c=5.363(7)$ Å.

As seen from the Figure 35 the calculated intensities around 22° – 24° are not consistent with the observed values. This discrepancy is attributed to the artifacts of the estimated background. Such discrepancy is affordable while fitting the nuclear structure, since the nuclear structure is known a priori. However this prevents an accurate fitting of the magnetic structures. In order to bypass such problems the magnetic contribution to the scattering can be in principle deduced while subtracting the diffraction patterns measured in the magnetic and paramagnetic states. Since

$$I_{afm} = I_{nuc} + I_{mag} + I_{bkg} \quad \text{and} \quad I_{pm} = I_{nuc} + I_{para} + I_{bkg} \quad (55)$$

where I_{afm} , I_{nuc} and I_{para} are the scattering contributions arising from magnetic, nuclear and paramagnetic structures (random magnetic moment) respectively. Subtracting one equation from another leads us to:

$$I_{afm} - I_{pm} + I_{para} = I_{mag} \quad (56)$$

Thus it can be seen that the rather complicated background subtraction is not required while analyzing the magnetic only intensity. Such a magnetic only scattering and the background subtraction is presented in detail in Figure 36. The magnetic only neutron scattering indicates a rather complicated long period antiferromagnetic structure with a non trivial propagation vector. However within the 10x10x10 times supercell no magnetic structure fitted the magnetic diffraction pattern.

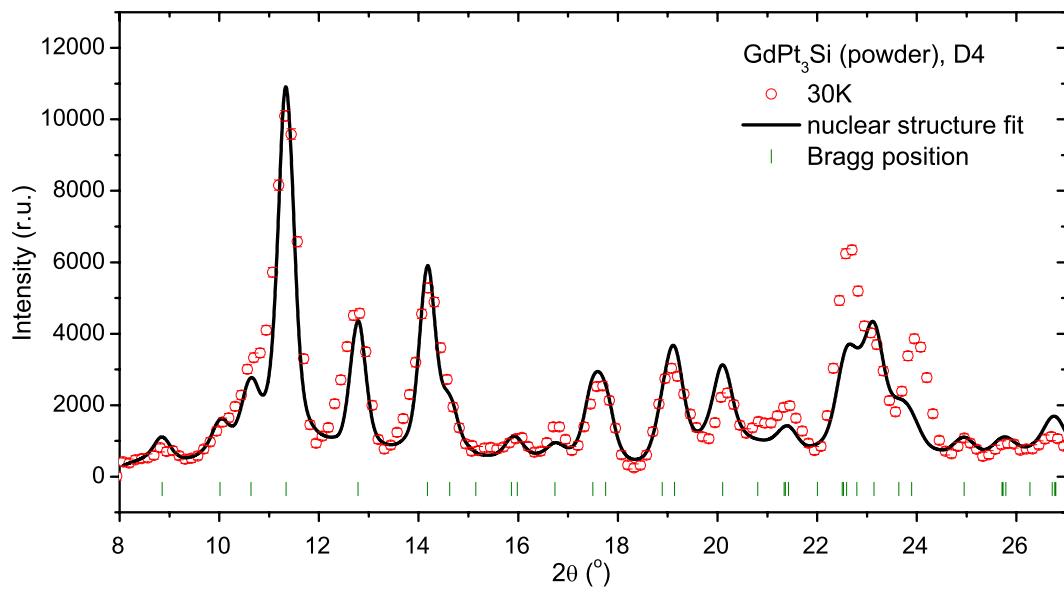


Figure 35: GdPt₃Si hot neutron diffraction pattern obtained at D4, ILL. Red open circles represent experimental data measured above the ordering temperature. The line represents the Rietveld refinement of the nuclear structure described in Table 14.

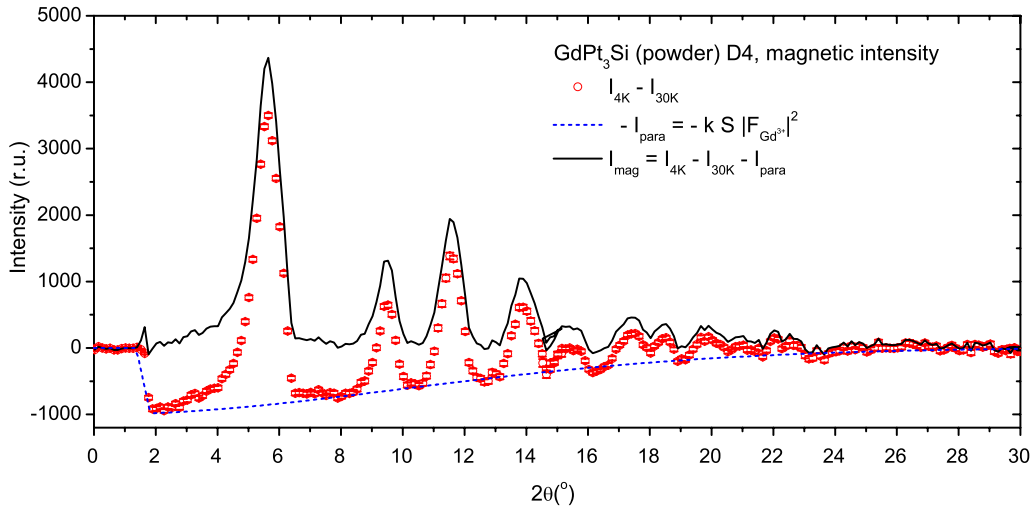


Figure 36: GdPt_3Si hot neutron magnetic only diffraction profile. Red open circles represent the difference between experimental data measured above and below the ordering temperature. The dashed blue line represents the calculated paramagnetic scattering contribution where $k \approx 10^3$ is the scale factor, S is the step function (for $2\theta > 1.967^\circ$ $S=0$ otherwise $S = 1$) and $|F_{\text{Gd}^{3+}}|$ is Gd^{3+} form factor. The line represents the magnetic only scattering intensity deduced using the equation (56).

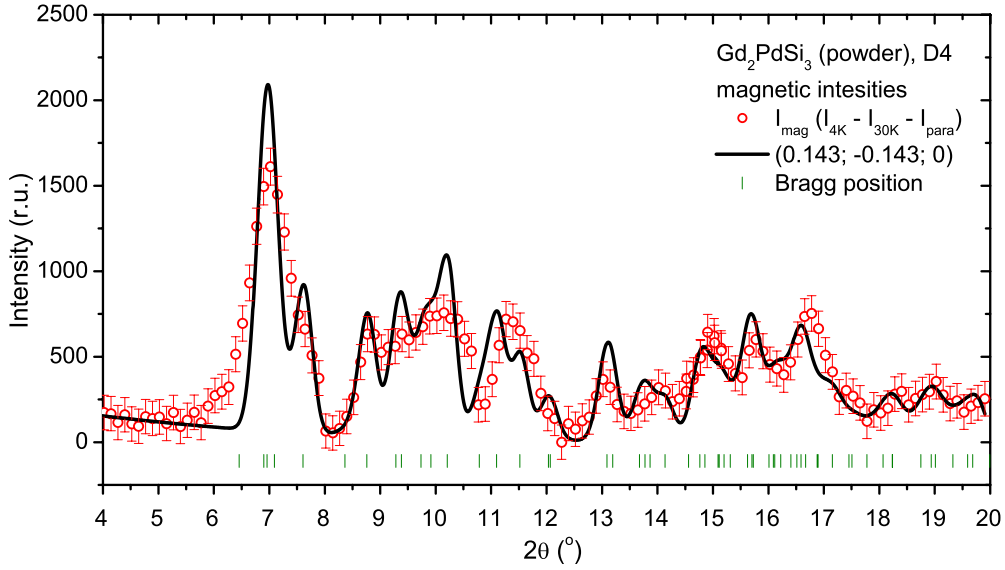


Figure 37: Gd_2PdSi_3 hot neutron magnetic only diffraction profile. Red open circles represent the magnetic only scattering contribution. Paramagnetic scattering has been taken into account while subtracting the high temperature pattern from the low temperature one. The solid black line represents calculated intensities for magnetic configuration with propagation vector $\tau = (0.143 \overline{0.143} 0)$.

6.3 Gd_2PdSi_3

Gd_2PdSi_3 crystallizes in an AlB_2 derived hexagonal centrosymmetric structure. This compound exhibits unusually large anisotropy, large negative magnetoresistance as well as a significant magnetocaloric effect [108, 26]. Preliminary results on single crystals using magnetic x-ray scattering indicated a propagation vector of $(0.143 \overline{0.143} 0)$ below $T_N = 22$ K.

The polycrystalline Gd_2PdSi_3 sample was prepared by an arc melting technique from natural Gadolinium with a purity of 99.99%. A tri arc furnace was used with argon atmosphere in temperatures of about 900° followed by homogenization at 750° in an evacuated quartz tube. The resulting crystallinity of the sample has been verified using x-ray diffraction.

The powder diffraction patterns were collected at the D4 instrument in ILL, Grenoble. A neutron wavelength of 0.49\AA was selected by a Cu (220) monochromator. In order to reduce absorption the powder was placed in a vanadium annular sample holder. Multiple diffraction patterns were collected in the temperature

range from 4 to 30 K with a counting time of one hour. An empirical background was estimated from the neutron diffraction pattern of a fully absorbing (cadmium foil) sample and an empty sample holder using the following formula: $I_{bkg} = I_{cd} + k(I_{empty} - I_{cd})$ where $k = 0.896$.

The neutron diffraction shows a comparatively weak signal. As explained in the previous section, the subtraction of background does not give a clear pattern that can be fitted with the nuclear structure from the previous x-ray investigation. However an analysis of pure magnetic intensities has been performed. The result of the fit is presented in Figure 37. The propagation vector indicated in previous magnetic x-ray experiments appears to index the magnetic intensities fairly well. The magnetic moments appear to be oriented in the plane perpendicular to the propagation vector and form a helical structure. However due to low experimental resolution and poor quality of the fit additional experiments on single crystal are necessary in order to clarify the magnetic structure.

6.4 GdCuSn

GdCuSn crystallizes in a CaIn_2 type centrosymmetric hexagonal structure. It develops an antiferromagnetism below $T_N = 24$ K. From Mössbauer spectroscopy several conclusions about magnetic structure have been drawn [28].

The polycrystalline GdCuSn sample was prepared by a levitation melting technique from natural Gadolinium with a purity of 99.99%. A tri arc furnace was used with argon atmosphere in temperatures of about 900°C followed by homogenization for 4 days at 800°C in an evacuated quartz tube. The resulting crystallinity of the sample has been verified using x-ray diffraction.

The powder diffraction patterns were collected at the D4 instrument in ILL, Grenoble. A neutron wavelength of 0.49 Å was selected by a Cu (220) monochromator. In order to reduce absorption the powder was placed in a vanadium annular sample holder. Multiple diffraction pattern were collected in the temperature range between 4 and 30 K with a counting time of one hour. An empirical background was estimated from the neutron diffraction pattern of a fully absorbing (cadmium foil) sample and an empty sample holder using the following formula: $I_{bkg} = I_{cd} + k(I_{empty} - I_{cd})$ where $k = 0.73$.

Due to the relatively large background the nuclear structure analysis has not been performed. The analysis of pure magnetic intensities is presented in Figure 38. Since the previous investigation with Mössbauer spectroscopy suggested the propagation vector $\tau = (0 \ 1/2 \ 0)$ with magnetic moments parallel to the c direction the resulting calculated neutron intensity is based on collinear structure parallel to the c and b directions. It is observed from the figure that the propagation vector is sufficient to index the pattern, however the structure seems to be more complicated. As seen from the reflection indices there is no possibility to arrange

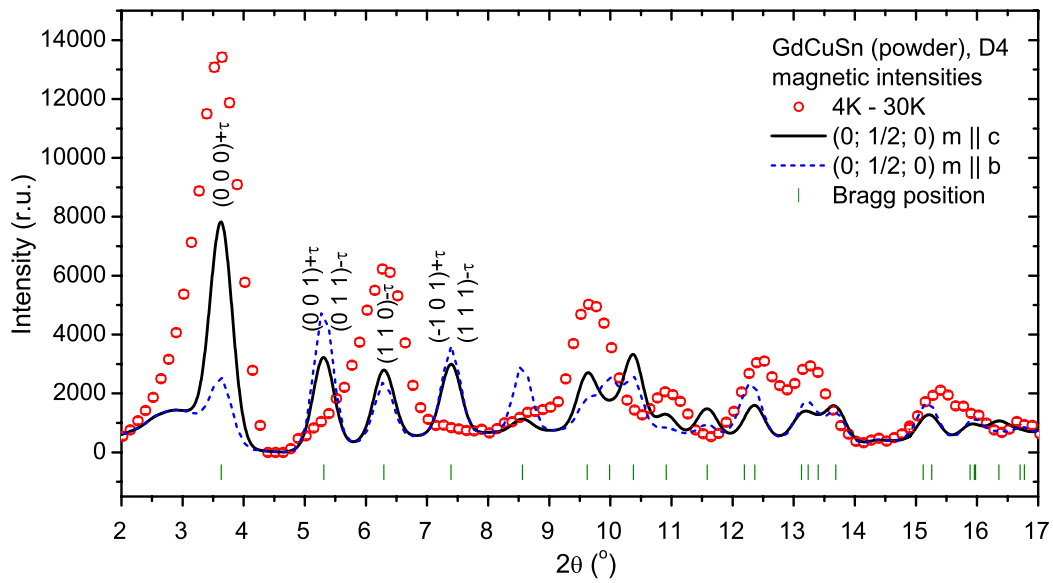


Figure 38: Hot neutron diffraction data obtained at D4, ILL, Grenoble. The red open circles represent the difference between high and low temperature spectra. Paramagnetic scattering has been subtracted from the high temperature spectra. The solid black and dashed blue lines represent the calculated intensities for the magnetic configuration with propagation vector $\tau = (0 \ 1/2 \ 0)$ and moments along c and b respectively.

moments so that the peaks arising from $(001) + \tau$, $(011) - \tau$ and $(\bar{1}01) + \tau$, $(111) - \tau$ will result in no intensity while keeping the significant scattering of the $(110) - \tau$ peak. Therefore the propagation vector must have a more complicated form than the one suggested by Mössbauer spectroscopy experiment in [28].

6.5 GdSi

GdSi crystalizes in the FeB type orthorhombic structure with spacegroup $Pnma$. In this structure, the orthorhombic unit cell contains 4 formula units with all the atoms occupying the Wyckoff position 4c. It develops weak ferromagnetism below temperature $T_C = 78$ K followed by a long period incommensurate antiferromagnetism below the Néel temperature $T_N = 54$ K. The thermal variation of the paramagnetic susceptibility along different directions shows significant anisotropy. Below the ordering temperature the antiferromagnetic order is being observed by magnetization and susceptibility measurements [109].

Paramagnetic Curie temperatures have been determined to be 20 K according to [109] or -8 K according to [110]. The estimated effective magnetic moment per Gd^{3+} is (in Bohr magnetons) $\approx 8.41\mu_B$ [109]. The saturation field $H_s \approx 20$ T was deduced from the magnetization in static high magnetic fields [56].

A GdSi single crystal was grown in a mirror furnace using the floating zone technique. The seed and feed for crystal growth were prepared by arc melting Gd and Si with a purity of at least 3N to obtain an alloy button of the nominal composition GdSi. In the most stable growth, a growth rate of 6 mm/h, and a rotation of the seed and feed of 30 rpm in opposite directions were used.

The monocrystalline GdSi sample was prepared by an arc melting technique from natural Gadolinium with a purity of 99.99%. A tri arc furnace was used with argon atmosphere in temperatures of about 900°. The resulting purity of the sample has been verified using x-ray diffraction.

The single crystal hot neutron diffraction was performed at the D9 instrument at ILL, Grenoble. A neutron wavelength of 0.51 Å was selected by a Cu (220) monochromator. Selected magnetic reflections were measured at temperatures of 2, 50 and 290 K in order to study the magnetic structure of the two different phases observed in this compound. The reflection intensities were integrated from a two dimensional multi-detector data and fitted with the FullProf package (see Figure 39). Numerous q-scans along different directions have been measured under various temperature conditions.

The nuclear structure was fitted at room temperature using integrated intensities data. The results of the nuclear structure refinement are summarized in Figure 15. Unit cell dimensions were determined to be $a = 7.99(9)$, $b = 3.86(9)$, $c = 5.75(9)$ Å. The full list of fitted intensities is presented in Tables 18 - 21.

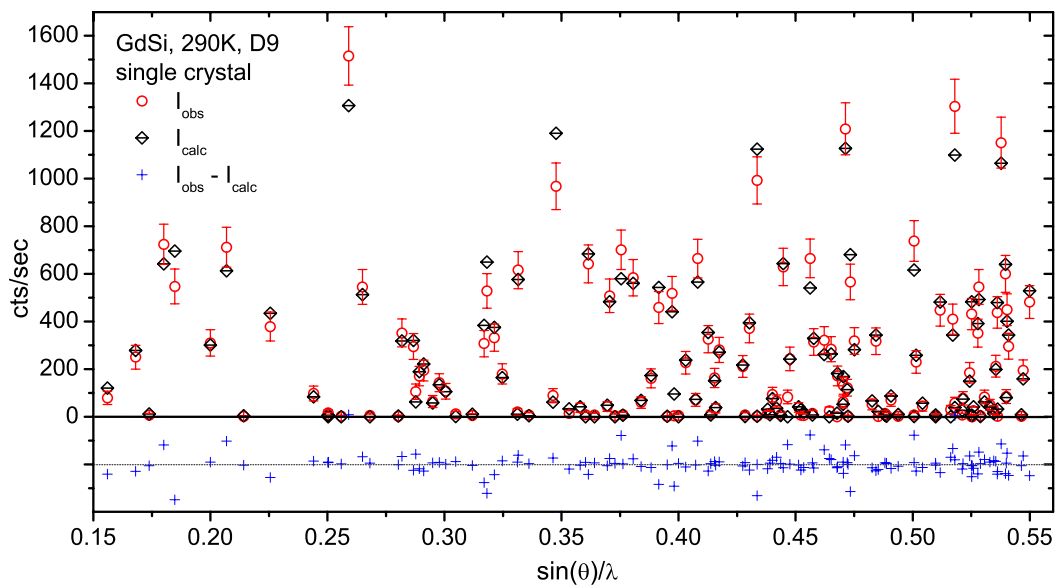


Figure 39: GdSi single crystal integrated intensities measured on D9, ILL, Grenoble. The red open circles correspond to experimental data measured above the ordering temperature. The black crossed diamonds represent the nuclear structure fit summarized in Table 15. The blue crosses represent the difference between calculated and observed intensities.

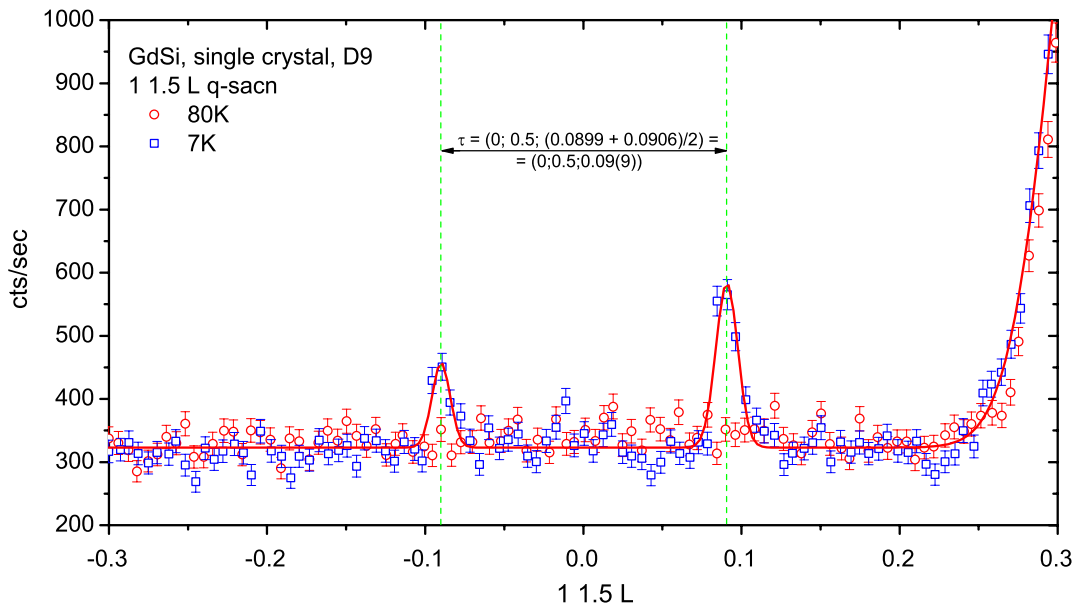


Figure 40: GdSi single crystal q-scan around (1 1.5 0) along L measured at D9, ILL Grenoble. Red open circles and blue open squares correspond to experimental data measured above and below the ordering temperature respectively. Red solid line represents the fitted intensity. The vertical dashed line represents the fitted peak positions for the $(1\ 1\ 0) \pm \tau$ reflections.

Table 15: Results of refinement of atomic positions with Rietveld refinement.

Atom	Wyckoff index	X	Y (cell units)	Z	Temperature factor (\AA^2)
Gd	4c	0.32080	0.25000	0.38560	0.13288
Si	4c	0.46280	0.25000	0.87340	0.12304

The results of the neutron single crystal diffraction indicate the magnetic propagation vector $\tau \approx (0 \ 0.5 \ 0.09)$ (see Figure 40). Due to insufficient amount of magnetic reflections found the orientation of magnetic moments has not been discovered.

6.6 Gd₅Ge₃

The Gd₅Ge₃ crystallizes in the hexagonal Mn₅Si₃ crystallographic structure (space group $P6_3/mcm$) where the Gd³⁺ ions occupy two different crystallographic sites ($4d$ and $6g$, see Table 16) [23]. The layers formed by the rare-earth ions are stacked along the hexagonal c axis. Magnetic ordering temperature of 76 K (with a further reorientation at 52 K) were obtained by susceptibility measurements [23]. The magnetic structure is still an open question. A first phenomenological model of the spin arrangement of Gd₅Ge₃ proposes a simple antiferromagnetism on the $4d$ sites and a 120° structure on the $6g$ sites is given in [111].

The polycrystalline Gd₅Ge₃ sample was prepared by an arc melting technique from natural Gadolinium with a purity of 99.99%. A tri arc furnace was used with argon atmosphere in temperatures of about 800°C. The resulting crystallinity of the sample has been verified using x-ray diffraction. The single crystals of Gd₅Ge₃ were prepared by a Czochralski crystal growing procedure in a tri arc furnace using single-phase polycrystalline samples as starting substance. The crystals were cut into rectangular pieces with a characteristic length of 2 mm, approximately. All of the pieces were annealed at 300°C for 24 hours in an evacuated quartz tube.

The single crystal diffraction was performed at the D9 and D3 instrument at the ILL, Grenoble. A neutron wavelength of 0.51 Å was selected by a Cu (220) monochromator. Nuclear reflections were measured at temperatures of 4, 60 and 100 K on the D9 instrument. The reflection intensities were integrated from a two dimensional multi-detector data and fitted with the FullProf package. Basic nuclear reflection set and numerous q -scans along different directions have been measured under various temperature and magnetic field conditions on D3.

In order to verify the nuclear structure, integrated intensities were fitted at 100 K. Results of the nuclear structure refinement are summarized in Figure 41.

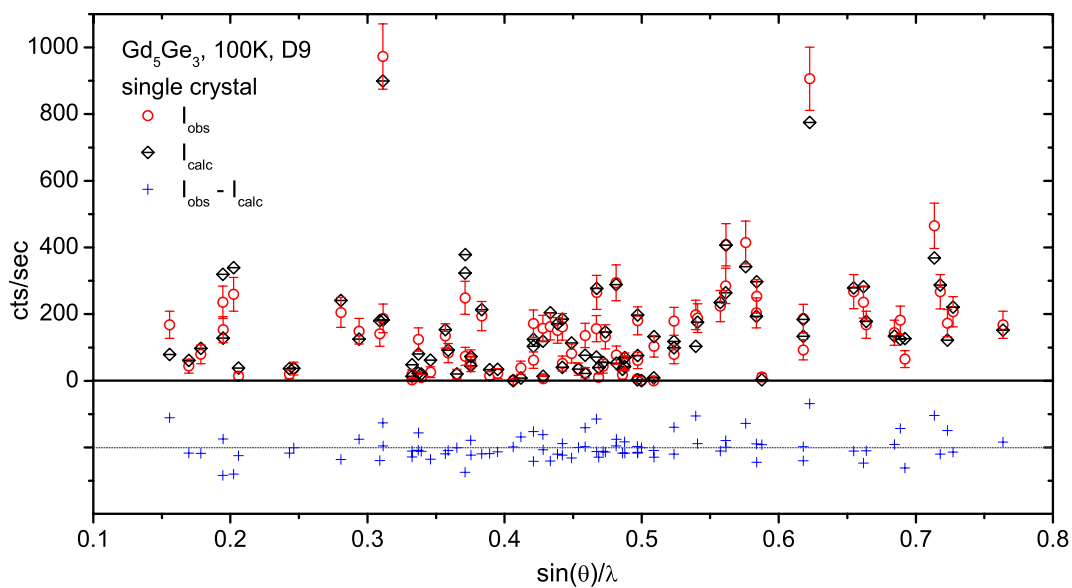


Figure 41: Gd_5Ge_3 single crystal integrated intensities data obtained on D9, ILL, Grenoble. The red open circles correspond to experimental data measured above the ordering temperature. The black crossed diamonds represent the nuclear structure fit summarized in Table 16. The blue crosses represent the difference between calculated and observed intensities.

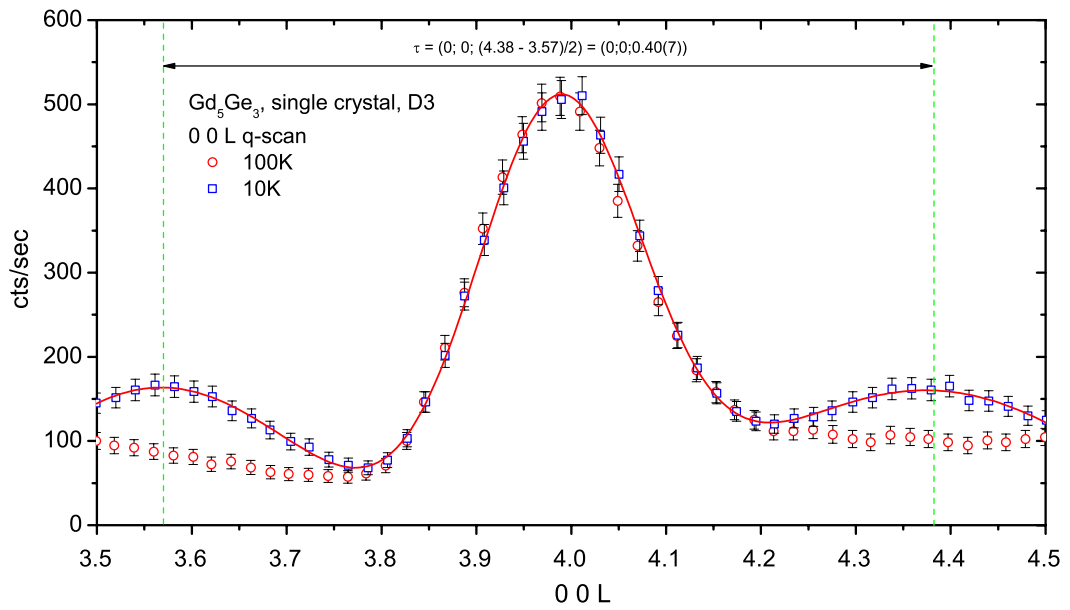


Figure 42: Gd₅Ge₃ q-scan around $(0\ 0\ 4 \pm L)$ reflection performed on D3, ILL, Grenoble. The red open circles and blue open squares correspond to experimental data measured above and below the ordering temperature, respectively. The red solid line represents the fitted intensity. The vertical dashed lines represent the fitted peak positions for the $(004) \pm \tau$ reflections.

Table 16: Results of refinement of atomic positions with Rietveld refinement.

Atom	Wyckoff index	X	Y (cell units)	Z	Temperature factor (\AA^2)
Gd	4d	0.333	0.666	0.0	0.25(6)
Gd	6g	0.24(9)	0.0	0.25	0.25(6)
Ge	6g	0.60(6)	0.0	0.25	0.25(6)

The unit cell dimensions were determined to be $a = b = 8.56(2) \text{ \AA}$, $c = 6.425(9) \text{ \AA}$. The full list of fitted intensities can be observed in Tables 22 - 24.

The single crystal diffraction experiment on D3 lead to determination of a propagation vector of $\tau = (0 \ 0 \ 0.40(7))$ (see Figure 42). The wide area q-scans show that within the error of the experiment no higher order harmonics have been found suggesting a non collinear structure. Recent resonant magnetic X-Ray scattering experiments confirmed this propagation vector [112].

7 Conclusions

The Gd^{3+} systems are very attractive candidates to study mainly due to their very large spin resulting in large signals in the bulk and scattering experiments. The standard model for Gadolinium magnetism (localized half filled $4f$ shell, dipolar anisotropy) in most cases is confirmed by various experiments.

The detailed study of spin-spin interactions in Gd based intermetallic compounds has been illustrated with several Gadolinium systems. Two particular compounds have been discussed in detail. GdCu_6 is the supporter of the Standard Model of rare-earth magnetism. Numerical simulations have been used to establish a link between the results of scattering experiments and its interpretation with respect to the observed bulk magnetic properties. The simulated behavior of the proposed magnetic structure reproduces the features in magnetization, susceptibility and specific heat. In contrast to GdCu_6 , the GdRu_2Si_2 tetragonal antiferromagnet is not well explained by the standard model for Gadolinium magnetism. Magnetization and susceptibility measured along the different crystallographic axes show an unusually high anisotropy and additional unexpected features in the magnetic phase diagram. The application of the mean field model calculation had a limited success in interpreting the experiment.

- The classical dipolar interaction is an important source of anisotropy in Gadolinium compounds [8]. The importance of this interaction has been illustrated in this thesis for GdCu_6 .

- However the case of GdSi and the more widely investigated GdRu₂Si₂ suggest stronger sources of anisotropy not related to classical dipolar interaction. Some of the results of numerical simulations for GdRu₂Si₂ suggest the presence of anisotropic bilinear exchange.
- In addition to anisotropic exchange the importance of non standard spin - spin interactions such as isotropic biquadratic exchange is suggested for GdRu₂Si₂.

Magnetic structures have been determined using the neutron scattering techniques at the ILL and LLB. Since gadolinium is the best neutron absorber found in nature the neutron experiments are non trivial and require specific techniques to be implemented:

- The most reliable neutron diffraction data on natural Gadolinium specimen has been obtained by investigations on preferably thin (or even better thin layer) shape single crystals with hot - thermal neutron wavelengths (0.5 - 0.8 Å). The higher the wavelength the better the resolution of the scattering experiment is to be expected. However, with the increase of the wavelength the absorption is increased demanding less amount of sample to be exposed (due to absorption) and require more time to acquire reasonable statistics.
- The inelastic neutron scattering is a desired technique for in-depth magnetic investigation. However only isotopically pure Gadolinium specimen are eligible for such a study. Making the applicability of neutron scattering methods limited in this particular case.
- Along the main alternatives to neutron scattering the magnetic resonant x-ray scattering is suggested. The field dependent magnetic x-ray scattering along with the numerical simulations can give an insight on very tricky antiferromagnetic structures. However, the process of making Gd based single crystal specimen is often very complicated and this clearly limits the application of the magnetic x-ray technique.

The relatively low resolution of neutron scattering techniques in the case of Gadolinium suggest a more systematic approach to available bulk experimental data. A detailed study of the experimental results, involving the mean field model numerical simulations is necessary to make definitive conclusions about the studied magnetic structures. Only limited experimental data is available on Gadolinium compounds. Therefore a generalized model of Gadolinium magnetism would require more systematic research in this area in order to explain the high anisotropy, magnetoelastic paradox, magnetocrystalline irreversibility and other exotic effects which have been recently discovered in Gadolinium magnetism.

8 Acknowledgments

8.1 Institutions and Organizations

The author wishes to acknowledge the support of Austrian Science Foundation (FWF) project P16778-N02 and the French-Austrian Bilateral Scientific Technical Exchange Program "Amadee" project 17/2003. This work is a part of the research plan MSM 0021620834 that is financed by the Ministry of Education of the Czech Republic. Part of this work was performed within the DFG-funded program of the Sonderforschungsbereich 463. Most of the work performed in this thesis has been carried out in the following institutions:

Institut Laue - Langevin, Grenoble, France (ILL).

Institut für Physikalische Chemie, Universität Wien, Austria (IPC UW).

Institut für Festkörperphysik, TU Dresden, Germany (IFP TUD).

Ames Laboratory USDOE, Iowa State University, Ames, USA (APS).

Labaratoire Leon Brillouin, CEA-CNRS, Saclay, France (LLB).

Institut für Festkörperphysik, TU Wien, Austria (IFP TUW).

Charles University, DCMP, Praha, Czech Republic.

Institut für Festkörper und Werkstofforschung, Dresden, Germany (IFW).

Centre National de la Recherche Scientifique, Grenoble, France (CNRS).

The list of contributed work together with contributors will be sorted by the chemical substance.

8.2 GdRu_2Si_2

The polycrystalline sample have been obtained by G. Behr at IFW. This sample has been studied later by soft X-Ray scattering at IFP TUW by A. Lindbaum and by neutron scattering at 7C2 instrument in LLB by M. Rotter with B. Beuneau being the local contact. J. Prokleska and J. Vejpravova from Charles University in Prague have obtained a significant amount of single crystal specimen of GdRu_2Si_2 .

Under the supervision of P. Svoboda those crystals have been characterized by specific heat, heat capacity and magnetostriction measurements.

The key discovery of magnetism of GdRu_2Si_2 was made at the 6-ID-B beamline in Argonne facility in USA by A. Kreyssig and A. Barcza. This discovery was later validated by myself on the hot neutron diffractometer D9 at ILL under the supervision of A. Stunault. The single crystal have been oriented with Laue X-Ray diffraction at the CNRS with the help of J. Debray.

Special thanks goes to M. Rotter, J. Jensen, A. Hiess and M. Johnson for providing a significant input in the development of a mean field model of this system.

8.3 GdCu_6

The polycrystalline sample has been obtained in IFW by G. Behr. This sample has been measured using hot neutron diffraction on 7C2 in LLB by M. Rotter and B. Beuneau. The numerical simulation were performed under the supervision of M. Rotter.

8.4 GdRu_2Ge_2

The polycrystalline sample has been obtained by G. Behr at IFW. Hot neutron scattering have been performed at 7C2 instrument in LLB by M. Rotter with B. Beuneau being the local contact. Additional help has been provided by P. Ambroise.

8.5 GdPt_3Si

The polycrystalline sample has been produced and characterized by E. Royanian at IFP TUW. The hot neutron diffraction have been performed at D4 in ILL. The experiments have been local contacted by B. Ouladiaf and A. Stunault. Additional input from instrument team of H. Fischer G. Cuellio and A. Ivanov was greatly appreciated.

8.6 Gd_2PdSi_3

The polycrystalline sample has been obtained in IFW by G. Behr. The hot neutron diffraction have been performed at D4 in ILL with B. Ouladiaf and A. Stunault as local contacts. Additional input from instrument responsible H. Fischer was greatly appreciated.

8.7 GdCuSn

The polycrystalline sample has been produced and characterized by E. Royanian at IFP TUW. The hot neutron diffraction have been performed at D4 in ILL. The experiment have been supervised by B. Ouladiaf and A. Stunault. Additional input from instrument team of H. Fischer G. Cuellio and A. Ivanov is greatly appreciated.

8.8 GdSi

The monocrystalline sample has been produced by T. Lee at the University of Warwick, Coventry, UK. He also had assisted to a series of hot neutron diffraction experiment on D9 supervised by A. Stunault and G. McIntyre. The single crystal has been oriented with Laue X-Ray diffraction at the CNRS with the help of J. Debray.

8.9 Gd₅Ge₃

The mono- and polycrystalline substances have been prepared by Y. Narumi and T. Tsutaoka at the institute of Solid State Physics, University of Tokyo. They have also characterized the substances with soft and hard X-Rays. The hot neutron diffraction have been performed at D4 and D9 diffractometers in ILL. A. Stunault and B. Ouladiaf have been local contacts for those experiments. Additional support from the instrument responsible G. Cuellio was greatly appreciated. The single crystal has been oriented with Laue X-Ray diffraction at the CNRS with the help of J. Debray.

8.10 General contributions

A special acknowledgement is directed to local contacts C. Ritter, W.Schmidt and M. Koza for assisting in numerous experiments performed during my stay at ILL although not presented in the framework of this thesis work [80, 113]. The Tree Axis Spectrometer group headed by J. Kulda has provided me with significant support during the work at ILL. The diffraction group at the ILL headed by the author of the FullProf software package J. Rodrigez-Carvahal provided the necessary support with various experiments and significant help in data analysis. Special thanks goes to Prof. P. Rogl and Dr. A. Grytsiv for providing the necessary infrastructure and assistance at IPC UW. H. Muller, E. Royanian, E. Bauer and A. Lindbaum have been very helpful at IFP TUW.

This work would not have been possible without the input of my supervisor M. Rotter and local ILL supervisor A. Hiess. I also wanted to acknowledge additional

help of G. Krexner and R. Golser at Physical Faculty of University of Vienna.

9 Appendixes

A Different Hamiltonian notations.

This is a technical note showing how biquadratic interactions can be dealt using the McPhase package. A typical magnetic Hamiltonian \mathcal{H} , which may be treated with the McPhase program package is:

$$\mathcal{H} = \sum_s B_l^m O_l^m(\mathbf{J}_i) - \frac{1}{2} \sum_{ij} \mathcal{J}(ij) \mathbf{J}_i \mathbf{J}_j - \sum_i g_J \mu_B \mathbf{J}_i \mathbf{H} \quad (57)$$

The first term describes the crystal field (Stevens Operators O_l^m , see table in appendix B), the second the magnetic exchange interaction, the third the Zeeman energy if an external magnetic field is applied. Instead (or rather in addition) to this it is also possible to treat the more general two ion exchange coupling

$$\mathcal{H}_{JJ} = -\frac{1}{2} \sum_{ij} \sum_{l'} \sum_{mm'} \mathcal{K}_{ll'}^{mm'}(ij) O_l^m(\mathbf{J}_i) O_{l'}^{m'}(\mathbf{J}_j) \quad (58)$$

This general notation allows the McPhase program to calculate not only classical ferromagnetic and antiferromagnetic systems but also systems with multipolar order.

In order to establish a correspondence between the two different notations the second order term in Hamiltonian (58) and (44) (e.g. $l = 2$, written down for isotropic interaction)

$$\begin{aligned} H_q = & -\frac{1}{2} \sum_{ij} K(ij) \left(\frac{1}{6} O_2^0(J_i) O_2^0(J_j) \right. \\ & + \frac{1}{2} (O_2^{-2}(J_i) O_2^{-2}(J_j) + O_2^2(J_i) O_2^2(J_j)) + \\ & \left. + 2(O_2^{-1}(J_i) O_2^{-1}(J_j) + O_2^1(J_i) O_2^1(J_j)) \right) \end{aligned} \quad (59)$$

has to be expressed in terms of the negative of the angular momentum operator. The Stevens Operators in equation (59) have to be substituted with their respective expressions in angular momentum operators presented in appendix B. In order not to get confused with the indices the following substitution $J_i \rightarrow M$ and $J_j \rightarrow N$ is adopted. Equation (59) can be rewritten:

$$\begin{aligned}
H_q = & -\frac{1}{2} \sum_{ij} K(ij) \left(\frac{1}{6} (3M_z^2 - J(J+1))(3N_z^2 - J(J+1)) + \right. \\
& + \frac{1}{2} (M_x^2 - M_y^2)(N_x^2 - N_y^2) + \frac{1}{2} (M_x M_y + M_y M_x)(N_x N_y + N_y N_x) + \\
& \left. + \frac{1}{2} (M_x M_z + M_z M_x)(N_x N_z + N_z N_x) + \frac{1}{2} (M_y M_z + M_z M_y)(N_y N_z + N_z N_y) \right) \quad (60)
\end{aligned}$$

The commutation rules of the negative of the angular momentum operator has to be considered:

$$[J_\alpha, J_\beta] = -i\mathcal{E}_{\alpha\beta\gamma} J_\gamma \quad (61)$$

so that

$$J_\alpha J_\beta + J_\beta J_\alpha = \begin{cases} 2J_\alpha J_\beta + J_\beta J_\alpha - J_\alpha J_\beta = 2J_\alpha J_\beta + i\mathcal{E}_{\alpha\beta\gamma} J_\gamma \\ 2J_\beta J_\alpha + J_\alpha J_\beta - J_\beta J_\alpha = 2J_\beta J_\alpha - i\mathcal{E}_{\alpha\beta\gamma} J_\gamma \end{cases} \quad (62)$$

taking (62) into account and since $J(J+1) = M_x^2 + M_y^2 + M_z^2 = N_x^2 + N_y^2 + N_z^2$ equation (60) can be transformed into

$$\begin{aligned}
H_q = & -\frac{1}{2} \sum_{ij} K(ij) \left(\frac{1}{2} (\vec{M} \cdot \vec{N}) + (M_x M_y N_x N_y + M_y M_x N_y N_x + \right. \\
& + M_x M_z N_x N_z + M_z M_x N_z N_x + M_y M_z N_y N_z + M_z M_y N_z N_y) + \frac{1}{6} J^2 (J+1)^2 + \\
& + \frac{1}{2} (M_z^2 N_z^2 + M_x^2 N_x^2 + M_y^2 N_y^2) - \frac{1}{2} (M_x^2 N_y^2 + M_y^2 N_x^2 + M_z^2 N_x^2 + \\
& + M_x^2 N_z^2 + M_z^2 N_y^2 + M_y^2 N_z^2) - \frac{1}{2} J^2 (J+1)^2 + \\
& \left. + \frac{1}{2} (M_x^2 + M_y^2 + M_z^2)(N_x^2 + N_y^2 + N_z^2) \right) \quad (63)
\end{aligned}$$

Note that the sum of last the two items in (63) is zero and these terms have been added to derive (63) to give the following result:

$$H_q = -\frac{1}{2} \sum_{ij} K(ij) \left(\frac{1}{2} (\vec{M} \cdot \vec{N}) - \frac{1}{3} J^2 (J+1)^2 + (\vec{M} \cdot \vec{N})^2 \right) \quad (64)$$

Thus the resulting equation which relates the biquadratic exchange written in terms of Hamiltonian (57) with the one written in terms of (58) will look like

$$H_q = -\frac{1}{2} \sum_{ij} K(ij) \left(\frac{1}{6} O_2^0(J_i) O_2^0(J_j) + \frac{1}{2} (O_2^{-2}(J_i) O_2^{-2}(J_j) + O_2^2(J_i) O_2^2(J_j)) + \right.$$

$$\begin{aligned}
& +2(O_2^{-1}(J_i)O_2^{-1}(J_j) + O_2^1(J_i)O_2^1(J_j)) = \\
= & -\frac{1}{2} \sum_{ij} K(ij) \left(\frac{1}{2}(J_i \cdot J_j) - \frac{1}{3}J^2(J+1)^2 + (J_i \cdot J_j)^2 \right) \quad (65)
\end{aligned}$$

Taking into account the higher term (non dipolar) of magnetic moment in the formalism of Stevens Operators (Hamiltonian (58)), the tensor $\mathcal{K}_l^{mm'}(ij) \neq 0$ for $l = 2$. Since McPhase uses the general form of Hamiltonian (58), the introduction of biquadratic exchange in Hamiltonian (44) will end up in

$$\begin{aligned}
H_{biquad} &= -\frac{1}{2} \sum_{ij} K(ij)(J_i \cdot J_j)^2 = \\
= & -\frac{1}{2} \sum_{ij} K(ij) \left(\frac{1}{6}O_2^0(J_i)O_2^0(J_j) + \frac{1}{2}(O_2^{-2}(J_i)O_2^{-2}(J_j) + O_2^2(J_i)O_2^2(J_j)) + \right. \\
& \left. +2(O_2^{-1}(J_i)O_2^{-1}(J_j) + O_2^1(J_i)O_2^1(J_j)) - \frac{1}{2}(J_i \cdot J_j) + \frac{J^2(J+1)^2}{3} \right) \quad (66)
\end{aligned}$$

The linear term of the exchange which comes out here has to be compensated in the linear part of the exchange in Hamiltonian (44) and (45), when scaling up the input files for McPhase program.

B Stevens Operators

Hereby Stevens Operators are presented up to the second order ($l = 2$) and their respective formulations in terms of angular momentum operators used in this thesis. For the full list of operators please refer to [114].

$$\begin{array}{l}
X = J(J+1) \\
O_{00} = 1 \\
\hline
O_1^{-1} = \frac{-i}{2}[J_+ - J_-] = J_y \\
O_1^0 = J_z \\
O_1^1 = \frac{1}{2}[J_+ + J_-] = J_x \\
\hline
O_2^{-2} = \frac{-i}{2}[J_+^2 - J_-^2] = J_x J_y + J_y J_x = 2P_{xy} \\
O_2^{-1} = \frac{-i}{4}[J_z(J_+ - J_-) + (J_+ - J_-)J_z] = \frac{1}{2}[J_y J_z + J_z J_y] = P_{yz} \\
O_2^0 = [3J_z^2 - X] \\
O_2^1 = \frac{1}{4}[J_z(J_+ + J_-) + (J_+ + J_-)J_z] = \frac{1}{2}[J_x J_z + J_z J_x] = P_{xz}
\end{array}$$

$$O_2^2 = \frac{1}{2}[J_+^2 + J_-^2] = J_x^2 - J_y^2$$

References

- [1] J. Jensen and A. R. Mackintosh, *Rare Earth Magnetism*, Clarendon Press Oxford (1991)
- [2] M. Loewenhaupt, “Crystal Fields In Low Symmetry Systems“, *Physica B* **163** (1990) 479
- [3] P. Fulde and M. Loewenhaupt, “Magnetic Excitations in Crystal Field split 4f Systems“, *Adv. Physics* **34** (1985) 589
- [4] V. Sima, V. Sima, M. Divis, P. Svoboda, Z. Smetana, S. Zajac and J. Bischof, “On Crystal-field spectroscopy based on specific heat and thermal expansion measurements: application to the TmCu₂ intermetallic compound“, *J. Phys. Cond. Mat.* **1** (1989) 10153
- [5] O. Moze, “Crystal Field Effects in Intermetallic Compounds studied by Inelastic Neutron Scattering“, in: *Handbook of Magnetic Materials* Vol. 11, ed. K. H. J. Buschow, Elsevier Science B. V. (1998) 494
- [6] M. Rotter, M. Doerr, A. Lindbaum, M. Loewenhaupt and B. Beuneu, “Using Hot Neutrons to Spot Small Sources of Magnetic Anisotropy“, in: *Annual Report*, Laboratoire Leon Brillouin, Saclay, France (2003) 48
- [7] M. Rotter, M. Loewenhaupt, M. Doerr, A. Lindbaum and H. Michor, “Non-collinear Amplitude Modulated Magnetic Order in Gd Compounds“, *Phys Rev.* **B 64** (2001) 014402
- [8] M. Rotter, M. Loewenhaupt, M. Doerr, A. Lindbaum, H. Sassik, K. Ziebeck and B. Beuneu, “Dipole Interaction and Magnetic Anisotropy in Gadolinium Compounds“, *Phys. Rev.* **B 68** (2003) 144418
- [9] J. A. Blanco, D. Gignoux and D. Schmitt, “Specific Heat in Gd compounds II. Theoretical model“, *Phys. Rev.* **B 43** (1991) 13145
- [10] T. Chattopadhyay, G. J. McIntyre and U. Köbler, “Antiferromagnetic Phase Transition in GdAg“, *Sol. Stat. Com.* **100** (1996) 117

- [11] J. A. Blanco, J. I. Espeso, J. I. GarcíaSoldevilla, J. C. GómezSal, M. R. Ibarra, C. Marquina and H. E. Fischer, “Magnetic structure of GdCu through the martensitic structural transformation: A neutron -diffraction study“, *Phys. Rev.* **B 59** (1999) 512
- [12] T. R. McGuire, R. J. Gambino, S. J. Pickart and H. A. Alperin, “Magnetic Structure and Exchange Interactions in Cubic Gadolinium Compounds“, *J. of Appl. Phys.* **40** (1969) 1009
- [13] F. Hulliger, “Magnetic Properties of the Rare Earth Pnictides“, *J. Magn. Magn. Mat.* **8** (1978) 183
- [14] M. J. Parsons, J. Crangle, K. U. Neumann and K. R. A. Ziebeck, “Unusual low temperature specific heat in ternary Gd intermetallic compounds“, *J. Magn. Magn. Mat.* **184** (1998) 184
- [15] E. Granado, B. Uchoa, A. Malachias, R. Lora-Serrano, P. G. Pagliuso and H. Westfahl, “Magnetic Structure and Critical Behavior of GdRhIn₅: resonant x-ray diffraction and renormalization group analysis“, *Phys. Rev. B* **74** (2006)
- [16] B. Stalinski, A. Czopnik, N. Iliew and T. Mydlarz, *J. de Physique* **C5** (1979) 149
- [17] Y. Narumi, A. Kikkawa, K. Katsumata, Z. Honda, M. Hagiwara and K. Kindo, “High field Magnetization of the Pyrochlore Compound Gd₂Ti₂O₇“, *Low Temp. Phys.* **850** (2006) 1113
- [18] M. Amara, S. E. Luca, R. M. Galera nad F. Givord, C. Detlefs and S. Kunii, “Exchange displacement waves in GdB₆“, *Phys. Rev.* **B 72** (2005) 64447
- [19] A. S. Wills, M. E. Zhitomirsky, B. Canals, J. P. Sanchez, P. Bonville, P. Dalmás de Reotier and A Yaouanc, “Magnetic ordering in Gd₂Sn₂O₇: the archetypal Heisenberg pyrochlore antiferromagnet“, *J. Phys. Cond. Mat.* **18** (2006) L37
- [20] H. Nakamura, N. Kim, M. Shiga, R. Kmieć, K. Tomala, E. Ressouche, J. P. Sanchez and B. Malaman, “The partially disordered state of the frustrated face-centred cubic antiferromagnet GdInCu₄“, *J. Phys.: Cond. Mat.* **11** (1999) 1095
- [21] S. Majumdar and E. V. Sampathkumaran, “Magnetic behavior of Gd₂CuGe₃: Electrical resistance minimum above the Néel temperature“, *Phys. Rev.* **B 61** (2000) 61

- [22] M. Barandiaran, D. Gignoux, J. Rodriguez Fernandez and D. Schmitt, *Physica B+C* **154B** (1989) 289
- [23] T. Tsutaoka, Y. Nishiume and T. Tokunaga, “Magnetic and Transport Properties of R_5Ge_3 ($R=Gd, Tb$) single crystals“, *J. Magn. Magn. Mat.* **272-276** (2004) e421
- [24] K. Sengupta, K. K. Iyer and E. V. Sampathkumaran, “Large magnetoresistance and magnetocaloric effect above 70 K in Gd_2Co_2Al , Gd_2Co_2Ga and Gd_7Rh_3 “, *Phys. Rev. B* **72** (2005) 54422
- [25] T. Tsutaoka, Y. Nakamori, T. Tokunaga and Y. Itoh, “Magnetic and Electrical Properties of R_7Rh_3 ($R=Gd, Tb, Dy, Ho, Er$ and Y)“, *J. Phys. Soc. Jap.* **70** (2001) 199
- [26] R. Mallik, E. V. Sampathkumaran, M. Strecker and G. Wortmann, “Observation of a minimum in the temperature-dependent electrical resistance above the magnetic-ordering temperature in Gd_2PdSi_3 “, *Europhys. Lett.* **41** (1998) 315
- [27] F. Casper, V. Ksenofontov, H. C. Kandpal, S. Reiman, T. Shishido, M. Takahashi, M. Takeda and C. Felser, “Structure and Properties of $GdAuSn$ and the $GdAuSn/MnAuSn$ System“, *Zeitschr. f. anorg. allg. Chemie* **632** (2005) 1273
- [28] D Bialic, R Kruk, R Kmiec and K Tomala, “ ^{155}Gd and ^{119}Sn Mössbauer effect investigations of $GdCuSn$ and $GdAuSn$ “, *Journal of Alloys and Compounds* **257** (1997) 49
- [29] B. J. Gibson, W. Schnelle, R. Pöttgen, K. Bartkowski and R. K. Kremer, “Susceptibility, specific heat and transport properties of $CeAuGe$ and $GdAuGe$ “, *Czechoslovak J. Phys.* **46** (1996) 2573
- [30] R. Pöttgen, G. Kotzyba, E. A. Görlich, K. Latka and R. Dronskowski, “Structure, Chemical Bonding, Magnetic Susceptibility and ^{155}Gd Moessbauer Sepctroscopy of the Antiferromagnets $GdAgGe$, $GdAuGe$, $GdAu_{0.44}In_{1.56}$, and $GdAuIn$ “, *J. Sol. Stat. Chem.* **141** (1998) 352
- [31] K. Latka, R. Kmiec, A. W. Pacyna, T. Fickenscher, R. D. Hoffman and R. Pöttgen, “Magnetism and ^{155}Gd Mössbauer spectroscopy of $GdAuMg$ “, *Sol. Stat. Sci.* **6** (2004) 301
- [32] K. Latka, R. Mkie, A. W. Pacyna, T. Fickenscher, R. D. Hoffmann and R. Pöttgen, “Magnetic Ordering in $GdAuCd$ “, *J. Magn. Magn. Mat.* **280** (2004) 90

- [33] D. Ravot, O. Gorochov, T. Roisnel, G. Andre, F. Bourre-Vigneron and J. A. Hodges, *Int. J. Mod. Phys. B* **7** (1993) 818
- [34] A Yaouanc, P DalmasdeR  otier, P C M Gubbens, A M Mulders, F E Kayzel and J J M Franse, “Muon-Spin-Relaxation study of the critical longitudinal spin dynamics in a dipolar Heisenberg ferromagnet“, *Phys. Rev.* **B 53** (1996) 350
- [35] D. Gignoux, P. Morin and D. Schmitt, “Multiple magnetic phase transitions in the tetragonal GdPt₂Si₂ and GdAg₂ compounds“, *Journal of Magnetism and Magnetic Materials* **102** (1991) 33
- [36] J. M. Barandiaran, D. Gignoux, D. Schmitt, J. C. Gomez-Sal, J. Rodriguez Fernandez, P. Chieux and J. Schweizer, “Magnetic Properties and Magnetic structure of GdNi₂Si₂ and GdCu₂Si₂ Compounds“, *J. Mag. Magn. Mat.* **73** (1988) 233
- [37] C. Detlefs, A. I. Goldman, C. Stassis, P. C. Canfield, B. K. Cho, J. P. Hill and D. Gibbs, “Magnetic Structure of GdNi₂B₂C by Resonant and Nonresonant X-ray Scattering“, *Phys. Rev.* **B 53** (1996) 6355
- [38] A. Lindbaum and M. Rotter, “Spontaneous Magnetoelastic Effects in Gadolinium Compounds“, in: *Handbook of Magnetic Materials* Vol. 14, ed. K. H. J. Buschow, Elsevier Sci. Pub. Amsterdam, The Netherlands (2002) 307
- [39] F. Canepa, S. Cirafici, F. Merlo, M. Pani and C. Ferdeghini, “Antiferromagnetism in Gd₂Ni₂Cd“, *J. Magn. Magn. Mat.* **195** (1999) 646
- [40] K. Latka, R. Kmiec, A. W. Pacyna, R. Mishra and R. P  ttgen, “Magnetism and hyperfine interactions in G₂Ni₂Mg“, *Sol. Stat. Sci.* **3** (2001) 545
- [41] M. Giovannini, H. Michor, E. Bauer, G. Hilscher, P. Rogl and R. Ferro, *J. Alloys Compd.* **280** (1998) 26
- [42] S. Ji, C. Song, J. Koo, K. B. Lee, Y. J. Park, J. Y. Kim, J. H. Park, H. J. Shin, J. S. Rhyee, B. H. O and B. K. Cho, “Interference of Magnetic and Anisotropic Tensor Susceptibility Reflections in Resonant X-ray Scattering of GdB₄“, *Phys. Rev. Lett.* **91** 257205
- [43] A. Garnier, D. Gignoux, D. Schmitt and T. Shigeoka, “Giant magnetic anisotropy in tetragonal GdRu₂Ge₂ and GdRu₂Si₂“, *Physica* **B 222** (1996) 80

- [44] R. Mallik and E. V. Sampathkumaran, “Magnetic precursor effects, electrical and magnetoresistance anomalies and heat capacity behavior of Gd alloys“, *Phys. Rev.* **B 58** (1998) 9178
- [45] L. D. Tung, J. J. M. Franse, K. H. J. Buschow, P. E. Brommer and N. P. Thuy, “A study of magnetic coupling in GdT_2Si_2 compounds (T=transition metal)“, *J. of All. Comp.* **260** (1997) 35
- [46] N. P. Duong, K. H. J. Buschow, E. Brück, J. C. P. Klaasse, P. E. Brommer, L. T. Tai and T. D. Hien, “Magnetic Properties of GdT_2Ge_2 Compounds (T= 3d, 4d)“, *J. of Alloys and Comp.* **298** (2000) 18
- [47] N. P. Duong, E. Brück, P. E. Brommer, J. C. P. Klaasse, F. R. de Boer and K. H. J. Buschow, “Magnetic properties of GdFe_2Ge_2 “, *Journal of Magnetism and Magnetic Materials* **242** (2002) 813
- [48] E. Bauer, R. Lackner, G. Hilscher, H. Michor, M. Sieberer, A. Eichler, A. Griбанov, Y. Seropegin and P. Rogl, “ REPt_3Si (RE = La, Pr, Nd, Sm and Gd): isotopes of the heavy fermion superconductor CePt_3Si “, *J. Phys. Cond. Mat.* (2005) 1877
- [49] Z. Islam, C. Detlefs, C. Song, A. I. Goldman, V. Antropov, B. N. Harmon, S. L. Budko, T. Wiener, P. C. Canfield, D. Wermeille and K. D. Finkelstein, “Effects of Band Filling on Magnetic Structures: the Case of RNi_2Ge_2 “, *Phys. Rev. Lett.* **83** (1999) 2817
- [50] W. Good, J. Kim, A. I. Goldman, D. Wermeille, P. C. Canfield, C. Cunningham, Z. Islam, J. C. Lang, G. Srajer and I. R. Fisher, “Magnetic structure of GdCo_2Ge_2 “, *Phys. Rev.* **B 71** (2005) 224427
- [51] T. Chattopadhyay, P. J. Brown, A. A. Stepanov, P. Wyder, A. I. Zvyagin, S. N. Barilo and I. Zobkalo, “Magnetic Phase Transition in Gd_2CuO_4 “, *Phys. Rev.* **B 44** (1991) 9486
- [52] E. Talik and M. Neumann, *Physica B* **193** (1994) 207
- [53] E. Talik and A. Slebarski, *J. Alloys Comp.* **223** (1995) 87
- [54] N. Tristan, S. A. Nikitin, T. Palewski, K. Nenkov and K. Skokov, “Specific heat of the Gd_3Co and Gd_3Ni compounds“, *J. Magn. Magn. Mat.* **258-259** (2003) 583
- [55] N. V. Baranov, A. V. Andreev, A. I. Kozlov, G. M. Kvashnin, H. Nakotte, H. Aruga-Katori and T. Goto, “Magnetic phase transitions in Gd_3Co “, *Journal-of-Alloys-and-Compounds* **202** (1993) 215

- [56] L. Tung, M. Lees and G. Balakrishnan and D. Paul, “Field induced magnetic transitions in a GdSi single crystal“, *Phys. Rev. B* **71** (2005) 144410
- [57] S. Takayanagi, Y. Onuki, K. Ina, T. Komatsubara, N. Wada, T. Watanabe, T. Sakakirare and T. Goto, “Magnetic Properties of Antiferromagnetic GdCu₆“, *J. Phys. Soc. Jap.* **58** (1989) 1031
- [58] H. Rohrer, “Properties of GdAlO₃ near the Spin-Flop Bicritical Point“, *Phys. Rev. Lett.* **34** (1975) 1638
- [59] D. Mck. Paul, H. A. Mook, A. W. Hewat, B. C. Sales, L. A. Boatner, J. R. Thompson and M. Mostoller, “Magnetic ordering in the high-temperature superconductor GdBa₂Cu₃O₇“, *Phys. Rev.* **B 37** (1988) 2341
- [60] J. Ziegłowski, PhD thesis Universität zu Köln (1988)
- [61] R. Rawat and I. Das, “Magnetocaloric and magnetoresistance studies of GdPd₂Si“, *J. Phys. Cond. Mat.* **13** (2001) L57
- [62] M. Rotter, A. Schneidewind, M. Loewenhaupt, M. Doerr, A. Stunault, A. Hiess, A. Lindbaum, E. Gratz, G. Hilscher and H. Sassik, “Magnetic Scattering on GdCu₂“, *Physica B* **284-288** (2000) 1329
- [63] V. K. Pecharsky, A. P. Holm, K. A. Gschneidner and R. Rink, “Massive Magnetic-Field-Induced Structural Transformation in Gd₅Ge₄ and the Nature of the Giant Magnetocaloric Effect“, *Phys. Rev. Lett.* **91** (2003) 197204
- [64] L. Tan, A. Kreyssig, J. W. Kim, A. I. Goldman, R. J. McQueeney, D. Wermeille, B. Sieve, T. A. Lograsso, D. L. Schlagel, S. L. Budko, V. K. Pecharsky and K. A. Gschneidner, “Magnetic structure of Gd₅Ge₄“, *Phys. Rev.* **B 71** (2005) 214408
- [65] C. Magen, L. Morellon¹, P.A. Algarabel, C. Marquina and M. R. Ibarra, “Magnetoelastic behaviour of Gd₅Ge₄“, *J. Phys.:Cond. Mat.* **15** (2003) 2389
- [66] J. A. Blanco, J. C. Gómez Sal, J. Rodríguez Fernandez, D. Gignoux, D. Schmitt and J. Rodríguez-Carvajal, “Magnetic and electrical properties of GdNi_{1-x}Cu_x compounds“, *J. Phys.: Cond. Mat.* **4** (1992) 8233
- [67] S. Ebisu, Y. Iijima, T. Iwasa and S. Nagata, “Antiferromagnetic transition and electrical conductivity in α -Gd₂S₃“, *J. Phys. Chem. Sol.* **65** (2004) 1113
- [68] M. Matsuda, A. Kikkawa, K. Katsumata, S. Ebisu and S. Nagata, “Neutron diffraction Study of α -Gd₂S₃“, *J. Phys. Soc. Jap.* **74** (2005) 1412

- [69] R. Kmiec, Z. Swiatkowska, R. Kruk and K. Tomala, “Magnetic properties of GdNiSn studied by ^{155}Gd Mössbauer spectroscopy“, *J. Magn. Magn. Mat.* **271** (2005) 326
- [70] Y. Andoh, M. Kurisu, S. Kawano and I. Oguro, “Magnetic Properties and magnetic anisotropy of RNiSn (R=Gd, Ho and Er) single crystals“, *J. Magn. Magn. Mat.* **177-181** (1998) 1063
- [71] S. W. Lovesey, *Theory of Neutron Scattering from Condensed Matter*, Clarendon Press Oxford (1984)
- [72] Varley F. Sears, “Neutron scattering lengths and cross sections“, *Neutron News* **3** (1992) 26
- [73] J. Baruchel, J. Hodeau, M. Lehmann, J. Regnard and C. Schlenker, *Neutron and synchrotron radiation for condensed matter studies* Vol. 2, Springer Berlin Heidelberg New York (1994)
- [74] M. Blume, “Magnetic scattering of x rays (invited)“, *Journal of Applied Physics* **57** (1985) 3615
- [75] J. P. Hannon, G. T. Trammell, M. Blume and Doon Gibbs, “X-Ray Resonance Exchange Scattering“, *Phys. Rev. Lett.* **61** (1988) 1245
- [76] J. P. Hill and D. F. McMorrow, “X-ray resonant exchange scattering: Polarization dependence and correlation functions“, *Acta Crystallogr. A* **52** (1996) 236
- [77] A. Edelstein, “Advances in magnetometry“, *J. Phys. Cond. Mat.* **19** (2007) 165217
- [78] R. L. Fagaly, “Superconducting quantum interference device instruments and applications“, *Rev. Sci. Instrum.* **77** (2006) 101101
- [79] M. Doerr, M. Rotter and A. Lindbaum, “Magnetostriction in Rare Earth based Antiferromagnets“, *Adv. Phys.* **54** (2005) 1
- [80] A. Devishvili, M. Rotter, A. Lindbaum, A. Barcza, A. Hiess, W. Schmidt and J. Vejpravová, “Measuring magnetostriction with neutrons“, *J. Phys.: Condens. Matter* **20** (2008) 104218
- [81] M. Rotter, M. Loewenhaupt and M. Doerr, “A Miniature Capacitance Dilatometer for Thermal Expansion and Magnetostriction“, *Research Mat- ters (Oxford Instruments)* **12** (2000) 2

- [82] M. Rotter, H. Müller, E. Gratz, M. Doerr and M. Loewenhaupt, “A new miniature capacitance dilatometer for thermal expansion and magnetostriction“, *Rev. Sci. Instrum.* **69** (1998) 2742
- [83] M. Bouvier, P. Lethuillier and D. Schmitt, “Specific heat in some gadolinium compounds. I. Experimental“, *Phys. Rev.* **B 43** (1991) 13137
- [84] Paul Handler, D. E. Mapother and M. Rayl, “AC Measurement of the Heat Capacity of Nickel Near its Critical Point“, *Phys. Rev. Lett.* **19** (1967) 356
- [85] Paul F. Sullivan and G. Seidel, “Steady-State, ac-Temperature Calorimetry“, *Phys. Rev.* **173** (1968) 679
- [86] R. Bachmann, Jr. F. J. DiSalvo, T. H. Geballe, R. L. Greene, R. E. Howard, C. N. King, H. C. Kirsch, K. N. Lee, R. E. Schwall, H.-U. Thomas and R. B. Zubeck, “Heat Capacity Measurements on Small Samples at Low Temperatures“, *Review of Scientific Instruments* **43** (1972) 205
- [87] J. Hwang, K. Lin and C. Tien, “Measurement of heat capacity by fitting the whole temperature response of a heat-pulse calorimeter“, *Review of Scientific Instruments* **68** (1997) 94
- [88] C. Kennedy, M. Stancescu, R. Marriott and M. White, “Recommendations for accurate heat capacity measurements using a Quantum Design physical property measurement system“, *Cryogenics* **47** (2007) 107
- [89] C. Lashley, M. Hundley, A. Migliori, J. Sarrao, P. Pagliuso, T. Darling, M. Jaime, J. Cooley, W. Hulst, L. Morales, D. Thoma, J. Smith, J. Boerio-Goates, B. Woodfield, G. Stewart, R. Fisher and N. Phillips, “Critical examination of heat capacity measurements made on a Quantum Design physical property measurement system“, *Cryogenics* **43** (2003) 369
- [90] J. E. Lynn and P. A. Seeger, “Resonance effects in neutron scattering lengths of rare-earth nuclides“, *Atomic Data and Nuclear Tables* **44** (1990) 191
- [91] B. E. Warren, *X-ray diffraction*, Courier Dover Publications (1990)
- [92] “<http://www.ill.eu/>“
- [93] H. M. Rietveld, “Line profiles of neutron powder-diffraction peaks for structure refinement“, *Acta Crystallographica* **22** (1967) 151
- [94] M. Rotter, “Using McPhase to calculate Magnetic Phase Diagrams of Rare Earth Compounds“, *J. Magn. Mag. Mat.* **272-276** (2004) 481

- [95] A. Garnier, D. Gignoux, N. Iwata, D. Schmitt, T. Shigeoka and F. Zhang, “Anisotropic metamagnetism in GdRu_2Si_2 “, *J. Magn. Magn. Mat.* **140** (1995) 899
- [96] P. Morin and D. Schmitt, “Quadrupolar interaction and magnetoelastic effects in rare earth intermetallic compounds“, in: *Ferromagnetic Materials* Vol. 5, ed. K. H. J. Buschow and E. P. Wohlfarth, Elsevier Sci. Pub. Amsterdam, The Netherlands (1990) 1
- [97] M. Rotter, M. Doerr, M. Zschintzsch, A. Lindbaum, H. Sassik and G. Behr, “The Magnetoelastic Paradox in GdAg_2 and GdRu_2Si_2 “, *J. Magn. Magn. Mat.* **310** (2007) 1383
- [98] M. Rotter, A. Lindbaum, M. Doerr, M. Loewenhaupt, A. Barcza and M. el. Massalami, “Magnetoelastic paradox: Absence of symmetry-breaking distortions below T_N in antiferromagnetic systems without orbital moment“, *Europhys. Lett.* **75** (2006) 160
- [99] M. Rotter, M. Loewenhaupt, A. Lindbaum, K. Ziebeck and B. Beuneu, “Diffraction experiments on GdCu_2In using hot neutrons“, *Physica B* **350** (2004) E63
- [100] Jens Jensen and Martin Rotter, “Magnetic double-q ordering of tetragonal $\text{GdNi}_2\text{B}_2\text{C}$: A way to explain the magnetoelastic paradox“, *Phys. Rev. B (Cond. Mat. and Mat. Phys.)* **77** (2008) 134408
- [101] M. Rotter, A. Schneidewind, M. Doerr, M. Loewenhaupt, A. M. el Massalami and C. Detlefs, “Interpreting magnetic X-ray scattering of Gd-compounds using the McPhase simulation program“, *Physica B* **345** (2004) 231
- [102] U. Köbler, D. Hupfeld, W. Schnelle, K. Mattenberger and T. Brückel, “Fourth order exchange interactions in $\text{Gd}_x\text{Eu}_{1-x}\text{S}$ “, *J. Magn. Magn. Mat.* **205** (1999) 90
- [103] U. Köbler, R. M. Müller, P. J. Brown and K. Fischer, “Experimental identification of fourth-order exchange interactions in magnets with pure spin moments“, *J. Phys.: Cond. Mat.* **13** (2001) 6835
- [104] S. B. Roy, M. R. Lees, G. R. Stewart and B. R. Coles, “Thermodynamic and transport properties of $(\text{Ce}_x\text{Gd}_{1-x})\text{Cu}_6$ for $0 \leq x \leq 1$ “, *Phys. Rev. B* **43** (1991) 8264
- [105] S. Takayanagi, Y. Ōnuki, K. Ina, T. Komatsubara, N. Wada, T. Watanabe, T. Sakakibara and T. Goto, “Magnetic Properties of Antiferromagnetic GdCu_6 “, *Journal of the Physical Society of Japan* **58** (1989) 1031

- [106] M. Rotter, M. Loewenhaupt, M. Doerr, A. Lindbaum and H. Michor, “Non-collinear Amplitude Modulated Magnetic Order in Gd Compounds“, *Phys Rev.* **B 64** (2001) 014402
- [107] M. Rotter, A. Lindbaum, A. Barcza, M. El Massalami, M. Doerr, M. Loewenhaupt, H. Michor and B. Beuneu, *Europhys. Lett.* **75** (2006) 160
- [108] S. R. Saha, H. Sugawara, T. D. Matsuda, H. Sato, R. Mallik and E. V. Sampathkumaran, “Magnetic anisotropy, first-order-like metamagnetic transitions and large negative magnetoresistance in single-crystal Gd_2PdSi_3 “, *Phys. Rev.* **B 60** (1999) 12162
- [109] J. Roger, V. Babizhetskyy, K. Hiebl, J. F. Halet and R. Guerin, “Structural chemistry, magnetism and electrical properties of binary Gd silicides and Ho_3Si_4 “, *Journal of Alloys and Compounds* **407** (2006) 25
- [110] H Saito, S Suzuki, K Fukamichi, H Mitamura and T Goto, “Metamagnetic transition in GdSi “, **65** (1996) 1938
- [111] Y. Narumi, Y. Tanaka, N. Terada, M. Rotter, K. Katsumata, T. Fukui, M. Iwaki, K. Kindo, H. Toyokawa, A. Tanaka, T. Tsutaoka, T. Ishikawa and H. Kitamura, “Magnetization Process and the Associated Lattice Deformations in an Intermetallic Compound Gd_5Ge_3 “, *J. Phys. Soc. Jpn.* **77** (2008) 053711
- [112] Y. Narumi, *private communication* (2009)
- [113] N. Melnychenko-Koblyuk, A. Grytsiv, L. Fornasari, H. Kaldarar, H. Michor, F. Roehrbacher, M. Koza, E. Royanian, E. Bauer, P. Rogl, M. Rotter, H. Schmid, F. Marabelli, A. Devishvili, M. Doerr and G. Giester, “Ternary clathrates Ba-Zn-Ge: phase equilibria, crystal chemistry and physical properties“, *J. Phys. Cond. Mat.* **19** (2007)
- [114] M. Rotter, “High speed algorithm for the calculation of magnetic and orbital excitations in rare earth based systems“, *Computational Materials Science* **38** (2006) 400

Table 17: GdRu₂Si₂ neutron single crystal integrated intensity data at 2 K. Only selected reflections are presented here. The observed value I_{mes} with error $\sigma_{I_{mes}}$ is accompanied by a calculated value I_{cal} for a helical antiferromagnet with propagation vector (0.22 0 0) with moments in the (**bc**) plane. Structure, polarization, form-factor, Debye-Waller and Lorenz factors are taken into account.

h	k	l	I_{mes}	$\sigma_{I_{mes}}$	I_{cal}
0	0	2	235	15	40
0	1	1	152	12	77
1	1	0	53	7	54
1	1	2	839	29	1262
0	2	0	1221	35	1802
0	2	2	44	7	16
1	1	4	171	13	194
1	2	1	51	7	36
0.222	0	2	353	19	304
-0.778	0	1	128	11	493
-0.222	1	1	54	7	212
0.222	1	1	55	7	214
0.778	0	3	588	24	163
0.222	1	3	45	7	110
0.222	0	4	61	8	100
1.222	0	3	204	14	137
1.222	1	2	125	11	132
1.778	0	2	104	10	133
0.222	2	0	26	5	70
1.778	1	1	77	9	111
0.778	1	4	63	8	69
0.222	2	2	27	5	57
0.778	2	1	36	6	64
2.222	0	0	1123	34	109
0.778	0	5	144	12	57

Table 18: GdSi neutron single crystal integrated intensity data at 298 K. The observed value I_{mes} with error $\sigma_{I_{mes}}$ is accompanied by a calculated value I_{cal} for a nuclear structure described in Table 15. Structure, polarization, form-factor, Debye-Waller and Lorenz factors are taken into account.

h	k	l	I_{obs}	I_{cal}	diff/ σ	$\sin(\theta)/\lambda$
0	1	1	79.5000	120.0535	-4.0554	0.15597
1	1	1	250.0000	278.6664	-3.5833	0.16805
0	0	2	6.3380	11.2593	-0.4101	0.17383
2	1	0	724.0000	642.0514	6.8291	0.18010
1	0	2	547.4300	696.0040	-7.0750	0.18475
2	1	1	310.0000	300.6115	1.1736	0.19998
3	0	1	711.6350	613.3310	1.9841	0.20688
2	0	2	1.0000	4.7805	-1.2602	0.21420
1	1	2	379.0000	434.2012	-6.1335	0.22562
3	1	1	98.0000	83.5560	2.4073	0.24407
2	1	2	16.0000	6.6412	1.8718	0.25030
4	0	0	8.0000	0.0805	2.6398	0.25031
3	0	2	2.0000	0.0156	0.6615	0.25585
0	2	0	1515.0000	1306.7367	10.9612	0.25901
4	0	1	545.0000	512.4321	2.7140	0.26497
1	0	3	5.0000	0.1471	1.2132	0.26814
1	2	1	2.3240	3.3287	-0.1256	0.28028
4	1	0	352.0000	318.7707	3.3229	0.28183
3	1	2	295.0000	320.2689	-2.8077	0.28676
2	2	0	105.0000	62.1124	4.2888	0.28767
2	0	3	171.0000	189.2694	-2.6099	0.28922
0	1	3	194.1060	221.6434	-1.8358	0.29113
4	1	1	64.0000	57.5875	0.7125	0.29493
1	1	3	143.0000	134.7482	0.8252	0.29778
2	2	1	107.0000	105.5068	0.2489	0.30051
4	0	2	12.0000	0.5057	2.2989	0.30475
0	2	2	5.6100	10.4501	-0.5378	0.31193
2	1	3	307.0000	383.8611	-8.5401	0.31689
-1	2	-2	528.3550	649.8839	-3.4411	0.31815
3	0	3	332.0000	375.0985	-4.3099	0.32129
5	0	1	180.0000	164.8525	1.8934	0.32474
4	1	2	20.0000	10.5396	1.8921	0.33113
3	2	1	616.0000	576.8315	3.0130	0.33149
2	2	2	8.0000	4.4477	1.1841	0.33611

Table 19: GdSi neutron single crystal integrated intensity data at 298 K. Continuation of Table 18 . The observed value I_{mes} with error $\sigma_{I_{mes}}$ is accompanied by a calculated value I_{cal} for a nuclear structure described in Table 15. Structure, polarization, form-factor, Debye-Waller and Lorenz factors are taken into account.

h	k	l	I_{obs}	I_{cal}	diff/ σ	$\sin(\theta)/\lambda$
3	1	3	89.0000	61.7714	3.0254	0.34641
0	0	-4	967.7510	1189.8473	-6.7129	0.34765
1	0	4	14.0000	33.4065	-3.8813	0.35324
5	0	2	38.0000	41.7382	-0.6230	0.35794
4	2	0	9.0000	0.1879	2.9374	0.36020
4	0	3	642.0000	683.9946	-2.9996	0.36145
3	2	2	7.0000	0.0881	2.3040	0.36407
2	0	4	42.4920	48.2223	-0.5209	0.36950
4	2	1	508.0000	482.9103	2.0908	0.37054
1	2	3	4.5900	0.3114	0.3890	0.37281
6	0	0	701.0810	580.0974	3.9027	0.37547
1	1	4	9.0000	6.8984	0.7005	0.37623
5	1	2	584.0000	560.7131	1.7913	0.38064
4	1	3	60.0000	68.2779	-1.1826	0.38395
2	2	3	161.0000	173.5690	-1.5711	0.38825
2	1	4	459.0000	543.1529	-7.0127	0.39153
3	0	4	1.0000	2.4468	-0.4823	0.39510
6	1	0	518.0000	441.1022	5.9152	0.39718
0	3	1	4.7560	96.0625	-5.4868	0.39812
4	2	2	5.0000	0.4711	1.5096	0.39995
1	3	1	227.0000	237.8284	-1.2032	0.40301
5	0	3	71.0000	72.9134	-0.2392	0.40729
2	3	0	664.0000	565.6674	6.5555	0.40818
3	2	3	326.0000	353.9984	-2.7998	0.41269
6	0	2	11.0000	7.8437	0.7891	0.41376
5	2	1	163.0000	151.3577	1.4553	0.41538
3	1	4	35.0000	38.1426	-0.4489	0.41579
2	3	1	281.0000	270.4521	1.0548	0.41733
5	1	3	211.0000	217.2185	-0.6909	0.42739
4	0	4	8.0000	0.5057	1.8736	0.42839
1	3	2	371.0000	395.1067	-2.1915	0.43021
0	2	4	992.4970	1123.4800	-4.7375	0.43353
6	1	2	2.0000	1.8950	0.0350	0.43355
1	2	4	12.6000	31.0290	-2.0477	0.43802
1	0	5	14.0000	8.9241	1.0152	0.43905

Table 20: GdSi neutron single crystal integrated intensity data at 298 K. Continuation of Table 19 . The observed value I_{mes} with error $\sigma_{I_{mes}}$ is accompanied by a calculated value I_{cal} for a nuclear structure described in Table 15. Structure, polarization, form-factor, Debye-Waller and Lorenz factors are taken into account.

h	k	l	I_{obs}	I_{cal}	diff/ σ	$\sin(\theta)/\lambda$
3	3	1	93.0000	76.3157	1.8538	0.44016
5	2	2	66.0000	35.7394	3.3623	0.44182
2	3	2	9.0000	5.7258	0.8186	0.44365
4	2	3	629.0000	643.2085	-1.0149	0.44467
7	0	1	83.0000	0.0030	7.5452	0.44659
4	1	4	243.0000	241.8437	0.1285	0.44754
2	2	4	39.5230	41.6473	-0.1931	0.45124
2	0	5	6.0000	29.9850	-3.9975	0.45223
0	1	5	4.8000	17.6328	-1.8333	0.45345
6	2	0	665.0000	540.9292	8.2714	0.45614
6	0	3	14.0000	7.1025	1.7244	0.45713
1	1	5	314.0000	329.3760	-1.3978	0.45775
4	3	0	322.0000	261.1172	5.5348	0.46217
6	2	1	25.0000	0.4759	4.0874	0.46435
3	3	2	284.0000	263.2041	2.0796	0.46519
5	0	4	0.0010	14.4978	-4.8323	0.46772
0	3	3	171.5000	181.1851	-0.6053	0.46790
4	3	1	62.0000	52.8762	1.1405	0.47027
2	1	5	131.0000	169.1841	-5.4549	0.47041
7	0	2	1209.0000	1127.4490	4.0776	0.47128
1	3	3	122.0000	114.4198	0.7580	0.47207
3	2	4	2.0000	2.2796	-0.0466	0.47243
3	0	5	566.0000	680.4246	-8.1732	0.47338
6	1	3	318.0000	281.8802	3.2836	0.47512
5	2	3	52.0000	66.5391	-1.8174	0.48267
2	3	3	317.0000	343.4823	-2.4075	0.48435
5	1	4	1.0000	22.7618	-5.4405	0.48532
6	2	2	14.0000	7.2861	1.3428	0.48814
7	1	2	8.0000	2.1830	1.4543	0.48875
3	1	5	70.0000	87.4166	-1.9352	0.49078
4	3	2	2.0000	9.1132	-2.3711	0.49378
4	2	4	8.0000	0.7107	1.8223	0.50061

Table 21: GdSi neutron single crystal integrated intensity data at 298 K. Continuation of Table 20 . The observed value I_{mes} with error $\sigma_{I_{mes}}$ is accompanied by a calculated value I_{cal} for a nuclear structure described in Table 15. Structure, polarization, form-factor, Debye-Waller and Lorenz factors are taken into account.

h	k	l	I_{obs}	I_{cal}	diff/ σ	$\sin(\theta)/\lambda$
8	0	0	738.0000	615.7318	7.6418	0.50063
4	0	5	230.0000	258.0109	-3.1123	0.50150
3	3	3	44.0000	56.9496	-1.6187	0.50416
1	2	5	4.0000	7.2810	-0.3646	0.50976
7	0	3	5.0000	0.0114	1.2471	0.50978
6	0	4	447.0000	481.3252	-2.6404	0.51171
7	2	1	30.0000	0.0015	4.2855	0.51627
8	1	0	410.0000	343.3851	5.5512	0.51711
4	1	5	58.0000	38.3642	2.1818	0.51795
0	4	0	1303.5000	1099.0302	4.8683	0.51802
2	2	5	7.0000	26.9482	-4.9870	0.52115
0	0	6	77.2910	74.1082	0.3168	0.52148
8	1	1	185.0000	149.0666	3.9926	0.52436
1	3	4	1.0600	5.9245	-0.6081	0.52509
1	0	6	431.0000	482.6887	-4.3074	0.52522
6	2	3	0.0010	5.6839	-1.8943	0.52541
7	1	3	26.0000	41.8117	-2.2588	0.52597
6	1	4	351.0000	391.2205	-3.6564	0.52784
5	3	2	545.0000	492.9244	3.7197	0.52826
1	4	1	4.0000	1.2110	0.4648	0.52898
4	3	3	83.0000	62.3136	2.0686	0.53065
2	4	0	50.2570	40.5099	0.8123	0.53293
5	2	4	29.0000	13.4915	2.2155	0.53465
5	0	5	212.0000	199.1272	1.4303	0.53549
2	3	4	438.0000	479.2287	-3.1714	0.53616
2	0	6	2.0000	31.8133	-9.9378	0.53629
7	2	2	1151.0000	1064.7632	4.3118	0.53777
3	2	5	600.0000	639.2888	-2.6193	0.53961
2	4	1	85.0000	80.0775	0.3282	0.53997
6	3	0	449.0000	401.2714	3.6714	0.54030
1	1	6	296.0000	342.6645	-4.2422	0.54095
0	4	2	2.4400	8.3537	-0.8448	0.54641
6	3	1	195.0000	159.2054	0.1729	0.54725
1	4	2	482.0000	529.4896	-1.8265	0.54998

Table 22: Gd₅Ge₃ neutron single crystal integrated intensity data at 100 K. The observed value I_{mes} with error $\sigma_{I_{mes}}$ is accompanied by a calculated value I_{cal} for a nuclear structure described in Table 16. Structure, polarization, form-factor, Debye-Waller and Lorenz factors are taken into account.

h	k	l	I_{obs}	I_{cal}	diff/ σ	$\sin(\theta)/\lambda$
0	0	-2	167.7500	78.5717	22.2946	0.15564
-1	1	-2	44.0000	60.9400	-8.4700	0.16962
2	1	0	79.5000	96.9810	-3.8847	0.17840
-1	-1	-2	235.4590	319.1741	-3.0949	0.19459
2	1	1	153.4651	127.8115	1.7120	0.19463
0	3	0	259.7808	339.6303	-2.3208	0.20228
-2	0	-2	13.6892	38.2570	-2.0473	0.20594
1	3	0	19.5000	36.4531	-4.2383	0.24311
2	2	1	36.7500	37.5640	-0.3052	0.24620
-2	-2	-2	205.0000	241.3104	-4.8414	0.28068
-1	-2	-3	149.0699	124.6748	1.3992	0.29382
1	4	0	140.8400	180.1130	-4.3063	0.30899
0	0	-4	973.0000	899.3548	8.1828	0.31128
0	-4	-2	187.5000	182.6893	1.0022	0.31140
1	-2	-4	3.0000	13.8076	-10.8076	0.33247
-3	-2	-2	19.8000	48.2003	-9.4668	0.33258
-1	-3	-3	14.6000	23.1180	-2.6619	0.33706
5	0	0	124.1461	80.5842	5.5318	0.33714
0	-2	-4	9.6000	20.7703	-3.4907	0.33924
-4	-1	-2	26.0000	61.6300	-8.9075	0.34598
4	2	0	134.7500	153.7906	-2.5866	0.35679
2	-3	-4	83.1666	92.2792	-1.1718	0.35878
4	2	1	20.0000	20.7740	-0.1935	0.36518
3	0	4	248.9942	323.1641	-0.7457	0.37124
-5	0	-2	73.3194	378.2983	-2.1526	0.37133
2	-5	-3	66.7500	45.0113	5.4347	0.37535
5	1	0	50.0000	72.9997	-6.3888	0.37542
3	3	2	194.0000	213.2078	-2.1342	0.38338
-2	-2	-4	15.1000	33.2613	-5.0982	0.38917
4	-3	-4	21.6667	34.6858	-3.9454	0.39497
2	-1	-5	1.6670	0.3321	0.8899	0.40625
0	-4	-4	39.0769	7.9154	6.2323	0.41188
-3	-3	-3	171.6013	124.0279	2.8977	0.42102
5	2	0	62.0000	103.5677	-6.9279	0.42109

Table 23: Gd₅Ge₃ neutron single crystal integrated intensity data at 100 K. Continuation of Table 22. The observed value I_{mes} with error $\sigma_{I_{mes}}$ is accompanied by a calculated value I_{cal} for a nuclear structure described in Table 16. Structure, polarization, form-factor, Debye-Waller and Lorenz factors are taken into account.

h	k	l	I_{obs}	I_{cal}	diff/ σ	$\sin(\theta)/\lambda$
3	-2	-5	157.0061	118.6303	2.5360	0.42805
2	-5	-4	6.0000	13.2294	-5.4222	0.42811
-6	6	-2	162.8000	203.8000	-4.5680	0.43347
4	-5	-4	151.2244	171.3808	-2.0995	0.43860
5	1	-3	52.0000	40.8031	3.7323	0.44209
6	1	0	161.7500	184.9514	-2.9002	0.44215
5	2	2	82.0000	113.2052	-3.9007	0.44893
4	-2	-5	35.1818	34.8655	0.0589	0.45383
1	3	-5	24.3333	21.9972	0.7557	0.45881
0	5	-4	135.9000	76.6773	7.6516	0.45887
0	0	-6	156.3333	71.1377	10.5762	0.46693
4	4	0	265.0000	277.4960	-1.1901	0.46715
6	-3	-4	10.5000	39.9084	-7.3521	0.46867
0	1	-6	43.7273	55.1743	-2.5189	0.47177
4	-6	-4	132.1995	146.3344	-0.8329	0.47350
-1	-1	-6	293.9123	288.9757	0.1667	0.48131
5	2	-3	77.0000	52.4869	6.1283	0.48148
2	0	-6	18.0000	34.6374	-4.9060	0.48601
3	-5	-5	59.3750	42.8291	2.7679	0.48763
6	-5	-4	52.3335	69.4604	-2.2462	0.48769
1	-5	-5	5.6365	2.7314	0.6826	0.49687
7	0	2	61.0000	75.6529	-2.5858	0.49699
5	3	2	179.9427	196.9749	-2.1977	0.49699
3	-1	-6	0.3340	0.8707	-0.2236	0.49985
0	-3	-6	0.0778	9.2947	-5.5301	0.50886
7	1	0	103.5000	132.9408	-4.5294	0.50907
-3	-3	-5	178.5000	118.0147	10.0809	0.52360
-5	-2	-4	78.7500	98.5465	-2.1770	0.52365
8	0	0	197.7500	103.4547	10.1031	0.53942
-6	-1	-4	187.7500	175.9846	1.2606	0.54074

Table 24: Gd₅Ge₃ neutron single crystal integrated intensity data at 100 K. Continuation of Table 23. The observed value I_{mes} with error $\sigma_{I_{mes}}$ is accompanied by a calculated value I_{cal} for a nuclear structure described in Table 16. Structure, polarization, form-factor, Debye-Waller and Lorenz factors are taken into account.

h	k	l	I_{obs}	I_{cal}	diff/ σ	$\sin(\theta)/\lambda$
6	3	2	224.2938	234.9720	-0.7259	0.55736
-4	-4	-4	285.0000	264.0424	1.5524	0.56136
0	8	2	408.2500	407.1182	0.0849	0.56143
-5	0	-6	415.0000	342.5063	4.8329	0.57592
-3	-3	-6	204.0000	193.0353	0.9137	0.58376
5	5	0	253.0000	297.2680	-3.6890	0.58394
-4	-2	-6	11.5000	3.0644	1.5817	0.58764
0	-6	-6	186.5000	184.5178	0.1239	0.61781
8	2	0	93.0000	133.2244	-5.7463	0.61799
0	0	-8	906.0000	774.7859	8.2009	0.62257
-3	0	-8	267.5000	278.4030	-0.6057	0.65461
-5	-5	-4	236.0000	282.8557	-3.4708	0.66173
-5	-3	-6	168.0000	178.3385	-0.8615	0.66393
2	9	0	143.9668	134.5311	0.9131	0.68432
9	2	1	181.7500	125.0686	5.3139	0.68873
-8	-2	-4	65.0000	126.7653	-12.3531	0.69196
-8	0	-6	465.0000	368.5988	5.3556	0.71344
6	6	2	267.0000	287.2286	-1.3486	0.71781
9	2	3	172.8462	121.9991	4.3583	0.72305
10	1	2	207.2500	221.0650	-1.1512	0.72725
-6	-1	-8	168.0000	151.6091	1.8212	0.76360

Anton Devishvili

30 Grande Rue
38700 La Tronche France
Tel.: +33619185381
e-mail: devishvili@ill.fr

Personal Information:

Date of Birth: 01.07.1982
Place of Birth: Moscow, Russia
Father: Dr. Vaja M. Devishvili, psycho-physiologist, MSU, Faculty of Psychology
Mother: Dr. Marina Mdivani, psychologist, self-employed person.
Nationality: Russian
Marital Status: single
Languages: fluent in English and Russian, conversational French and German.

Education:

- 1988** Elementary School N°110 in Moscow, Russia.
1993 Gymnasium N°109 in Moscow, Russia.
1999 Physical studies at the Moscow State University (Physical Faculty, Division of Magnetism), Master thesis title: "Magnetic field distribution modelling", supervisor: Acc.Prof. Dr. N. Perov.
2005 started PhD studies at University of Vienna (Faculty of Physics), PhD thesis title: "Study of magnetic properties of high spin value systems of Rare Earth based compounds", supervisor: Dr. M. Rotter.

Work Experience:

- 04.2003–** Experimental work at Magnetic materials research laboratory,
01.2005 Moscow State University, Physical Faculty, Russia.
Vibrating Sample Magnetometry.
06.2004– Theoretical work at Neurosensor Laboratory, Engineering Faculty,
12.2004 National University of Singapore, Singapore.
Computational methods in Magnetism.
04.2005– Experimental work at Technical University of Vienna
09.2005 Technische Universität Wien, Austria.
Dilatometry in high magnetic fields.
10.2005– Experimental work at Institute of Solid State Physics
03.2006 Technische Universität Dresden, Germany.
X-Ray diffraction.

05.2006– Experimental work at Institute von Laue Langevin
12.2008 Grenoble, France.
Inelastic neutron scattering.

05.2009– Experimental work at Institute of Experimental/Solid State Physics
till now Ruhr Universität Bochum, Germany.
Polarised neutron reflectometry.

Other qualifications and skills:

Research interests: Solid state Magnetism, Rare-Earth magnetism, computational methods in Magnetism, scientific computing, experiment automation.

Computer Languages: C, C++, BASIC, VisualBasic, MS Visual Studio, Apple X-Code, Maple, HTML, LaTeX.

Software: MS Office (all products), Apple iWork, Adobe CS (Illustrator and Photoshop), 3D Studio.

Scientific Software: Origin, KaleidaGraph, FullProf, McPhase, ANSYS, GNUplot.

Instrument Control Software: MAD (DS/TAS), Nomad, pMAD, spec.

Publication List:

1. Master thesis "Magnetic field distribution modelling", MSU (2005).
2. Internship report "Magnetic Environment Detection", NUS (2004).
3. N. Melnichenko-Koblyuk, A. Grytsiv, A. Devishvili et. al, "Ternary clathrates Ba-ZnGe: phase equilibria, crystal chemistry and physical properties", J. Phys.: Cond. Matter 19 (2007) 216223.
4. A. Devishvili, M. Rotter, A. Hiess et. al, "Measuring Magnetostriction with Neutrons", J. Phys.: Cond. Matter 20 (2008) 104218.
5. M. Doerr, M. Rotter, A. Devishvili et.al. "Magnetostructural irreversibilities in R_5Ge_3 (R=Gd,Nd) intermetallics", J. Phys.: Conf. Ser. 150 (2008) 042025.
6. A. Devishvili, M. Rotter, M. Doerr et. al. "Magnetic Structure of $GdCu_6$ ", J. Phys.: Cond. Mat. 21 (2008) 126002.
7. A. Devishvili, M. Rotter, A. Kryessig, M. Doerr et. al, "Magnetic Structure of $GdRu_2Si_2$ ", submitted to Phys. Rev. B. (2010).

Conference contributions:

1. A. Devishvili, M. Doerr, M. Rotter, B. Beuneu, A. Lindbaum, „Neutron Diffraction Experiments on Gd Compounds“, Jahrestagung der ÖPG (27 – 30.09.2005)
2. A. Devishvili, M. Doerr, M. Rotter, B. Beuneu, A. Lindbaum, G. Behr, „Neutron Diffraction Experiments on Gd Compounds“, Jahrestagung der ÖPG (28 – 30.09.2006)
3. A. Devishvili, M. Rotter, A. Hiess, A. Lindbaum, H. Muller, A. Barcza, J. Vejpravova, W. Schmidt. „Measuring magnetostriction with neutrons“, European Conference on Neutron Scattering, Lund, Sweden (24–29. 06.2007).

4. A. Devishvili, M. Rotter, M. Doerr, A. Kreyssig, J. Vejpravova, J. Prokleshka, „Using McPhase to calculate magnetoelastic and magnetocaloric properties of GdRu_2Si_2 “, Workshop on Magnetostrictive Materials and Magnetic Refrigeration 2007, Baden bei Wien, Austria (13–15.08.2007).
5. A. Devishvili, M. Rotter, A. Hiess, A. Lindbaum, H. Muller, A. Barcza, J. Vejpravova, W. Schmidt. „Measuring magnetostriction with neutrons“, GÖCH Symposim 2007 „Physikalische Chemie in Österreich“ (19–20. 10.2007).
6. A. Devishvili, M. Rotter, M. Doerr, B. Beuneau, G. Behr. „Magnetic Structure of GdCu_6 “, Deutsche Neutronennstreutagung 2008, Garching, Germany (15–17.10.2008).

Invited seminar talks:

1. MSU, Faculty of Physics, Moscow, Russia November 2005, “Magnetoelastic paradox“.
2. TUD, Institute of Solid State Physics, Dresden, Germany, December 2005, “Magnetic structure of GdCu_6 , GdRu_2Si_2 , GdRu_2Ge_2 ”.
3. MSU, Faculty of Physics, March 2006, Moscow, Russia, “Magnetic structure determination methods from elastic neutron scattering data”.
4. ESRF, Grenoble, France, February 2009. “Magnetic structure of Gd^{3+} based intermetallic compounds”

Experimental reports:

1. M. Rotter, M. Fröhlich, A. Devishvili, R. Schedler, M. Doerr, A. Kreyssig, M. Loewenhaupt, A. Schneidewind, J. Vejpravova, P. Svoboda, Orbital Excitations in PrCu_2 , ILL Experimental Report CRG-1029 (2005).
2. M. Rotter, A. Devishvili, J. Vejpravova, P. Svoboda, „Orbital Excitations on PrCu_2 “, ILL Experimental Report TEST-1104 (2005).
3. M. Rotter, A. Lindbaum, A. Devishvili, M. Doerr, M. Loewenhaupt, A. Hiess, R. Kremer, “Increasing the transmission of Gadolinium”, ILL Experiment Report 3-07-192 (2005).
4. A. Devishvili, M. Rotter, P. Rogl, N. Melnychenko, “Lattice dynamics in clathrate (I) type $\text{Ba}_8\text{Zn}_8\text{Ge}_{38}$ ”, ILL Experiment Report 4-01-624 (2006).
5. A. Devishvili, M. Rotter, E. Bauer, A. Grytsiv P. Rogl, N. Melnychenko, “Inelastic Response of Nd-based skutterudite $\text{NdFe}_4\text{Sb}_{12}$ ” ILL Experiment Report 4-03-1549 (2006).
6. D. Adroja, H. Michor, M. Rotter, A. Devishvili, “Quantum fluctuations in the novel non-Fermi-Liquid system CeNi_9Ge_4 ”, ILL Experiment Report 4-05-610 (2006).
7. P. Rogl, A. Devishvili, M. Rotter, A. Grytsiv, N. Melnychenko, “Lattice dynamics of $\text{Ba}_8\text{Zn}_8\text{Ge}_{38}$ type (I) clathrate”, ILL Experiment Report 5-23-573 (2006).
8. A. Devishvili, M. Rotter, H. Michor, M. Frontzek, “Magnetic structure of GdPt_3Si , Gd_2PdSi_3 and GdCuSn ” ILL Experiment Report 5-31-1629 (2006).

9. A. Devishvili, "Magnetostriction and thermal expansion of PrCu₂", ILL Experiment Report TEST-1233 (2007).
10. M. Rotter, A. Devishvili, P. Rogl, W. Kockelmann, J. Taylor, "Magnetic Response of ZrMn₂", ILL Experiment Report 5-53-131 (2007).
11. A. Devishvili, Y. Xinlin, M. Rotter, T. Le, J. Prokleska, J. Vejpravova, A. Kreyszig, "Magnetic Structure of GdSi and GdRu₂Si₂", ILL Experiment Report 5-41-416 (2007).
12. A. Devishvili, M. Rotter, A. Machado, "Defect structure in a new superconductor phase of Nb₅Ge₃C_x composition", ILL Experiment Report 5-23-576 (2007).
13. M. Rotter, M. Doerr, A. Devishvili, T. Tsutaoka, Y. Narumi, "Magnetocrystalline irreversibility in Gd₅Ge₃", ILL Experiment Report 5-41-453 (2008).
14. M. Koza, A. Devishvili, P. Rogl, M. Rotter, A. Grytsiv, N. Melnychenko, "Lattice dynamics in type (I) Ba₈Zn_xGe_{46-x} clathrates" ILL Experiment Report 7-01-231 (2008).